Optical projection tomography for whole organ imaging

Thèse N° 9094

Présentée le 1er mars 2019

à la Faculté des sciences et techniques de l'ingénieur
Laboratoire d'optique biomédicale
Programme doctoral en biotechnologie et génie biologique

pour l'obtention du grade de Docteur ès Sciences

par

David NGUYEN

Acceptée sur proposition du jury

Prof. A. Radenovic, présidente du jury
Prof. T. Lasser, Prof. D. Van De Ville, directeurs de thèse
Prof. D. Holmberg, rapporteur
Prof. M. Rudin, rapporteur
Dr T. Scharf, rapporteur

2019

ÉCOLE POLYTECHNIQUE
FÉDÉRALE DE LAUSANNE

> *Tout homme est tiraillé entre deux besoins, le besoin de la pirogue,*
> *c'est-à-dire du voyage, de l'arrachement à soi-même, et le besoin de l'arbre,*
> *c'est-à-dire de l'enracinement, de l'identité, et les hommes errent constamment*
> *entre ces deux besoins en cédant tantôt à l'un, tantôt à l'autre; jusqu'au jour*
> *où ils comprennent que c'est avec l'arbre qu'on fabrique la pirogue.*
> — Mythe mélanésien de l'île de Vanuatu

À tout mes bienveillants. . .

Acknowledgements

The work presented in this thesis is the result of four years of research and a life full of adventures, which I shared with the many companions I was fortunate to meet during my journey. I am grateful to all of them.

My first thanks go to my supervisor, Professor Theo Lasser, who gave me the opportunity to pursue my doctoral studies in the Laboratoire d'Optique Biomédicale (LOB). Ever since I started working in the field of optics, Theo consistently pushed me to reach my potential and inspired me to become the scientist I am today. During these four years of Ph.D., I have also been supervised by Professor Dimitri Van De Ville, who was always available for discussions. Dimitri's help has been invaluable after Theo's retirement at the end of 2017. Thank you, Dimitri, for being such a benevolent and caring person.

I am thankful to my thesis jury members, Professor Dan Holmberg, Professor Markus Rudin, Doctor Toralf Scharf, and Professor Aleksandra Radenovic, for their precious time and the validation of my work through their vast experience in their respective domains of research. A special thank goes to Aleksandra, who hosted me in her lab after Theo's retirement. She has always been supportive of my work, and she made sure I had all the resources needed to finish my thesis.

Next, I want to thank our collaborators from Lund University under the supervision of Professor Holmberg, Doctor Anja Schmidt-Christensen, and Julia Nilsson, for our discussions and their guidance on the development of the optical projection tomography instrument. I also want to thank our collaborator at EPFL, Mélanie Hannebelle, who shared her vision of open hardware imaging instruments and her enthusiasm. Together, we did not put a camera in liquid nitrogen to observe a change in thermal noise. I am also grateful to the facilities at EPFL and their staff. In particular, I received invaluable support from the Center of Phenogenomics (CPG) team, Doctor Eleonora Simeoni, Doctor Isabelle Desbaillets, the veterinarians Gisèle Ferrand, and Arthur Humbert, Doctor Alexis Kousteff, Doctor Emilie Gesina, Doctor Raphaël Doenlen, Arnaud Legay, Valérie Zbinden, who helped in setting up and managing our mice colonies. I am also indebted to the Histology Core Facility (HCF) team and Doctor Jessica Sordet-Dessimoz. Thank you for your expertise and your patience. A big thank you to the Bioengineering doctoral school in the person of Professor Matteo Dal Peraro, and Sonja Bodmer.

Then, my gratitude goes to the members of the LOB team, Fabienne Ubezio, Noelia Simone, Doctor Azat Sharipov, Doctor Tomas Lukes, Doctor Corinne Berclaz, Doctor Séverine Coquoz, Doctor Amir Nahas, Doctor Jérome Extermann, Doctor Daniel Szlag, Doctor Marcin Sylwestrzak, Doctor Kristin Grüssmayer, Doctor Joechem Deen, Adrien Descloux, Antonio

Lopez, Ronald Gianotti. Thank you for your welcoming attitude toward me and for making the lab a beautiful place to work in. Special thanks to Doctor Miguel Sison, Doctor Paul Marchand, and Arielle Planchette, who, in addition to being the craziest people I have ever met, are also great friends. Together, they helped me go through the Ph.D. thesis and were always there when I needed a laugh. A great thank to my hard-working students, Silas Schlatter, Amélie Ducrey, and Octave Martin. Another great thank to the members of the LBEN team, which I didn't have much time to meet. They were all welcoming, and I directly felt integrated into their group.

I will proceed with my mentors, who I am grateful to for teaching me their knowledge with a strong sense of work ethics: Professor Philippe Renaud, Professor Hans-Peter Herzig, Doctor Myun-Sik Kim, Doctor Nicolas Sommet. I also want to give a special attention to Professor Hans-Jörg Ruppen, and Doctor Myriame Favre, who both had a pivotal role in my academic career. They were present at the darkest moments of my life, and they saw the light in me that I could not even see. Thank you, Professor Ruppen, thank you, Doctor Favre, you planted the very roots of the person I am today.

My next thanks are to my friends. Just thinking about you I feel a strong sense of gratitude. I want to start with my childhood friends, Andy Singele, Loïc Duran, Sylvain Bovet, and *mon frérot* Cédric Haldimann. I have so many memories of our decadent parties, and I couldn't wish for more caring and loving friends. Although our path went apart, we will always share this connection. Then I want to thank my many friends at EPFL, and in particular, Ha-Phong Nguyen, Martin Jobin, and Hammam Elaian. You made my studies at EPFL an incredible journey, and you kept me motivated to work harder.

During my thesis, I was fortunate to have extracurricular activities. I am thankful to the Centre d'acceuil MalleyPrairie in Lausanne and its staff who hired me as a volunteer school tutor. It was a fantastic experience to share these moments with less fortunate kids. I also started to climb, and it rapidly became a passion. I am grateful to have met other mountain lovers who share my ideals and even helped me go through my academic journey. I am so thankful for the active climbing community here in Lausanne. A special thank to Simon De Coulon with whom I shared amazing bouldering trips. Thank you to Carmen Lonfat and Kent Barbey, the next generation of *academic* climbers. Tea always was heart-warming in your flat share. I wish you to live your craziest dreams. A peaceful thank you to the yogi master Alexandra Hugon and her van Jimmy, who made me grow spiritually (both of them). Thank you also to Vincent Amstutz, Vincent Santi, and Erin A. Converse (and not Erine), whose outstanding life ethics is a source of inspiration. A grateful thank you to Eveline and her therapeutic massages. You helped me keep a healthy mind in a healthy body.

Then, there is Stefano Ginella. I can't remember exactly when we met, but ever since, we developed a strong friendship based on the two French words *Force* & *Honneur*. Stefano, it feels as if I have known you forever. You taught me how to become a better climber and a better person. Together we have climbed, run, ski, always seeking for the best of ourselves. Thank you, Stefano. Thank you for our discussions, thank you for always supporting me.

Earlier this year, I was lucky to meet the one I call my soul mate. Her name is Doctor Virginie Uhlmann. Although it's been only a couple of months, we already went through so many

adventures. Virginie, thank you for what you shared with me, thank you for being with me through these difficult times at the end of my thesis, thank you for the review of my writings, and thank you for allowing me to be myself. I am looking forward to our next adventures. Piep. Finally, I want to thank my family. Léonard, Anthony, and their mother Marie-Claire, Don Larenzo and Myshima. My brothers Romain, and Vincent. Thank you for your unconditional love through all these years together. There's not much else to say, and I am sure that we will remain a strong family together, even without blood-links. Last but not least, I want to thank my father Van Son, who lived through the boat people for me to be able to present this thesis.

Lausanne, 27 Décembre 2018 D. N.

Abstract

In the past twenty years, far-reaching studies of molecular and cellular processes have reached a milestone in their maturation, and the knowledge from these studies was ready to apply at higher organizational levels. At that time, rodent models were long established. However, methods were inappropriate to image a whole rodent organ, such as the mouse brain, which drove the emergence of a new range of imaging techniques, later gathered under the name mesoscopy. Mesoscopic techniques filled a gap between classical microscopy and medical imaging techniques, such as magnetic resonance imaging, and X-ray computed tomography. They allow the acquisition of centimeter-sized samples. In this thesis, we focus on one of these mesoscopic imaging techniques called optical projection tomography, or OPT, and its potential application to Alzheimer's disease (AD) research. We review the fundamentals of OPT and describe the filtered back-projection algorithm, which is the primary tomographic reconstruction method of this technique. We also go through the implementation of OPT for whole mouse brain imaging, including sample preparation. We show that OPT is suitable to image the whole brain anatomy based on endogenous fluorescence, and the whole neural vasculature as well as amyloid plaques (a hallmark of AD) with adequate fluorescent markers. Then, we dwell on the characterization of OPT instruments. We give some insights on the instrument point spread function and discuss the influence of the number of projections on the quality of the reconstructed image. Afterward, we illustrate the application of OPT to study amyloidosis progression in a preliminary cross-sectional study, where we have used supervised learning to quantify the amyloid plaque load. In this study, we show that OPT can be used to quantify amyloidosis in whole mouse brains and that comparison between individuals of different age can be performed. Imaging of a whole mouse brain is unquestionably necessary. At this scale though, it has some constraints. We present the limitations of OPT, and we share how we think they can be circumvented by combining this modality with another microscopy technique, namely structured illumination microscopy. We see that this other microscopy technique has the potential to produce high-resolution zooms in selected regions of interest based on a prior OPT acquisition. The results presented in this work have led to the duplication of our OPT instrument in Lund University, and we hope they will help to foster advances in OPT and broaden its range of application. We also hope that this work will contribute to making OPT more accessible and user-friendly.

Key words: optical projection tomography (OPT); Alzheimer's disease (AD); whole mouse brain imaging; 3D fluorescence mesoscopy

Résumé

Au cours des vingts dernières années, des études de grande portée sur les processus moléculaires et cellulaires arrivées à maturité et la connaissance de ces études était prête à être appliquée à des niveaux organisationnels plus élevés. À cette époque, les modèles de rongeurs étaient établis depuis longtemps. Cependant, les méthodes existantes étaient inappropriées pour imager des organes de rongeurs entiers, tel que le cerveau de souris. Cela conduisit à l'émergence d'une nouvelle gamme de techniques d'imagerie, plus tard rassemblées sous le nom de mesoscopie. Ces techniques mesoscopiques comblèrent le vide entre la microscopie classique et les techniques d'imagerie médicales, telles que l'imagerie par résonance magnétique et la tomodensitométrie aux rayons X, en permettant l'acquisition d'échantillons de taille centimétrique. Dans cette thèse, nous nous intéressons à une techniques d'imagerie mesoscopique appelée tomographie par projection optique, ou TPO, et à son application à la recherche sur la maladie d'Alzheimer. Nous revisitons les fondamentaux de la TPO et nous décrivons l'algorithme de rétro-projection filtrée, qui est le moyen de reconstruction tomographique au cœur de cette technique. Nous allons passons également en revue une implémentation de la TPO pour l'imagerie de cerveaux de souris entiers incluant la préparation des échantillons. Nous montrons que la TPO est adéquate pour l'imagerie de l'anatomie des cerveaux entiers basée sur la fluorescence endogène et la vascularisation cérébrale, ainsi que les plaques d'amyloïde (une signature caractéristique de la maladie d'Alzheimer) avec des marqueurs fluorescents adéquats. Nous nous penchons ensuite sur la caractérisation des instruments de TPO. Nous donnons un aperçu de la fonction d'étalement du point de l'instrument et nous discutons l'influence du nombre de projections dans la qualité de l'image obtenue après reconstruction. Après quoi, nous illustrons l'application de la TPO à l'étude de la progression de l'amyloïdose dans une étude transversale préliminaire où nous avons utilisé l'apprentissage supervisé pour identifier et quantifier la charge de plaque d'amyloïde. Dans cette étude, nous montrons que la TPO peut être utilisée pour quantifier l'amyloïdose dans les cerveaux de souris entiers et qu'une comparaison entre individus d'âges différents peut être réalisée. L'imagerie de cerveaux de souris entiers est sans conteste nécessaire. À cette échelle cependant, elle impose certaines contraintes. Nous présentons les limitations de la TPO et nous partageons comment nous pensons qu'elles peuvent êtres dépassées en combinant cette modalité avec une autre technique de microscopie, la microscopie à illumination structurée. Nous verrons que la microscopie à illumination structurée a le potentiel de produire des zooms à haute résolution dans des régions d'intérêts basée sur une acquisition TPO antérieure. Les résultats présentés dans cette thèse ont conduit à la duplication de notre instrument de

TPO à l'univérsité de Lund et nous espérons qu'ils pourront aider à favoriser les avancées en TPO et élargir son champ d'applications. Nous espérons aussi que ce travail contribuera à rendre la TPO plus accessible et facile à utiliser.

Mots-clés : tomographie par projection optique (TPO) ; maladie d'Alzheimer ; imagerie du cerveau de souris entier ; mesoscopie de fluorescence en 3D

Contents

List of Figures

List of Tables

1 Introduction

3D imaging is an essential field of biomedical research [1] with numerous applications in medicine and life sciences. From drug evaluation studies [2] to cellular and molecular diagnostics [3], tridimensional imaging of biomedical specimen is performed at different scales, as summarized in Figure 1.1. Until twenty years ago, the techniques were mainly divided into two categories.

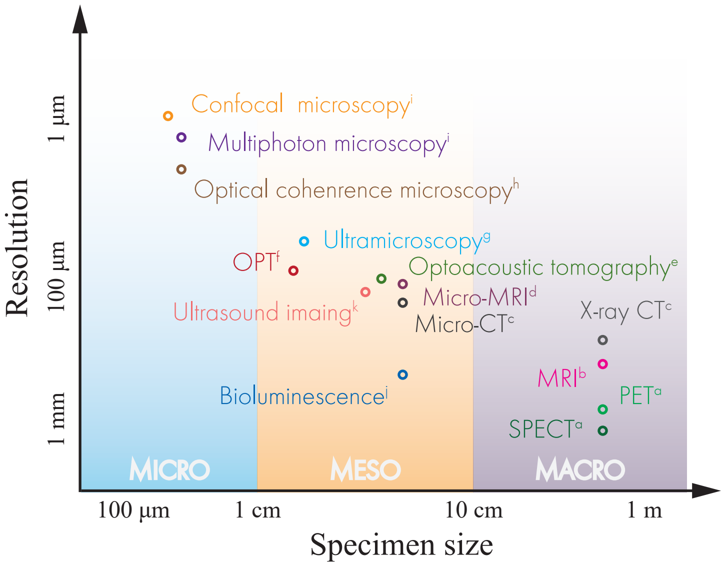

Figure 1.1 – Representation of the trade-off between resolution and specimen size in common 3D biomedical imaging techniques. Until twenty years ago, there was a gap between microscopic and macroscopic imaging techniques. Mesoscopic imaging techniques have started to fill it since then due to a growing interest in small animal imaging. [a]Khalil *et al.* [4], [b]Stucht *et al.* [5], [c]du Plessis *et al.* [6], [d]Baltes *et al.* [7], [e]Ntziachristos *et al.* [8], [f]Sharpe *et al.* [9], [g]Pende *et al.* [10], [h]Fercher *et al.* [11], [i]Ntziachristos [12], [j]Rehemtulla *et al.* [13], [k]Deffieux *et al.* [14].

On one hand, *macroscopic* imaging techniques, such as X-ray computed tomography (CT) [15, 16], positron emission tomography (PET) [17], single-photon emission computed tomography

(SPECT) [4] and magnetic resonance imaging (MRI) [18], are used to diagnose human patients. They can produce 3D images of the whole human body with different levels of specificity and a resolution from 0.2 to 8 mm.

On the other hand, optical *microscopic* imaging techniques, such as confocal microscopy [19], multiphoton microscopy [20], and optical coherence microscopy [11], are used for cell and tissue imaging [21]. In optical microscopy, the specimen size generally falls between 100 µm and 1 mm with a resolution from 5 µm, down to a few hundreds of nanometers [22] (for super-resolution microscopy).

Over the past decades, a growing interest for small animal imaging [23] has fostered the emergence of 3D imaging techniques operating at an intermediate regime called *mesoscopy* [12]. In this regime, the specimen size range from few millimeters to several centimeters with a resolution of 200 µm to 3 µm, filling the gap between microscopy and the macroscopic imaging techniques.

Mesoscopy

A variety of imaging techniques are today available in the mesoscopic imaging range. A subset of these techniques is adapted from their macroscopic counterpart. Micro-CT [24], for example, is the equivalent of CT for small animal imaging. Driven by recent technological progress, micro-CT is widely used in small animal cancer research [25]. It offers a resolution of approximately 50 µm in whole rodents and a sensitivity to tumors *in vivo*. Micro-MRI [26] is the equivalent of MRI for small animal imaging. The resolution increase is obtained by different means, such as increasing the magnetic field strength [27] and using cryogenic detection devices [7]. Micro-MRI has been used for *in vivo* visualization of amyloid plaques [28] (a hallmark of Alzheimer's disease, see below), it has a resolution of 30 to 80 µm and excellent sensitivity to soft tissues. Micro-CT and MRI have both similar resolutions, they mainly differ in their contrast mechanism which leads to differences in specificity, and can be performed *in vivo*. However, they require expensive instruments that have a high maintenance cost, restricting their availability. Fortunately, these two imaging techniques are only a small sample of the available mesoscopic technologies.

Functional ultrasound imaging (fUS) [14] measures echoes from sound waves transmitted through the organ to retrieve 3D images *in vivo*. It is sensitive to blood flow, allowing to perform functional imaging of the brain at a high temporal resolution and with a spatial resolution down to 100 µm.

Optoacoustic tomography (OA) [29, 30] detects ultrasounds upon absorption of an excitation light beam, increasing the detected signal resolution in deep tissues. In the mesoscopic regime, OA has a resolution of approximately 100 µm [8] and has been used to image the vasculature in whole mouse brains *in vivo* [31]. This technique requires direct contact with the specimen to guarantee a good transmission of the sound waves.

Bioluminescence imaging (BLI) [32] is an optical imaging technique based on the detection of chemically-induced fluorescence. BLI has been used in small animal cancer research [13] and can be used *in vivo*. Bioluminescence imaging in mammals requires the introduction of a transgene leading to the expression of enzymes such as Firefly or Renilla luciferase, which upon interaction with their substrates generate light. The method is characterized by a high sensitivity as the intrinsic bioluminescence background signal is absent in mammalian cells. Due to a pronounced scattering of the emitted photons in biological tissues, the spatial resolution of BLI is approximately 1 mm.

Ultramicroscopy [33] and light-sheet microscopy [34] are probably the most commonly used among the mesoscopic fluorescence imaging techniques. Both techniques use a sheet of light to illuminate a single section of the sample selectively. The subtle difference between these two is that, in state-of-the-art light sheet microscopy, the trend is in increasing the resolution and going towards super-resolution microscopy [35], while in ultramicroscopy, the aim is to enhance the light-sheet performance at the mesoscopic-scale and to provide small animal imaging capacity [36, 37, 38, 39]. Ultramicroscopy has been used in developmental studies of whole zebra fish *in vivo* [40], and fruit flies [41, 10]. Ultramicroscopy also found applications in imaging of the whole mouse brain neuroanatomy [42] and amyloidosis in an Alzheimer's disease model [43]. This technique can achieve a resolution down to the cellular level in whole model organisms using engineered sheets of light [10].

Finally, optical projection tomography (OPT) [9] finds a sweet spot among this range of mesoscopic imaging techniques.

Optical projection tomography

OPT is sometimes described as an optical equivalent of CT [44]. It can have a resolution down to 5 µm in centimeter-sized samples [45], and it can use fluorescent and colored dyes [9]. OPT has been applied to the zebra fish vasculature *in vivo* [46], whole mouse pancreas in the study of diabetes [47, 48, 49], and whole mouse brain neuroanatomy [50]. Additionally, helical scanning enables imaging of elongated samples, such as the mouse spinal cord [51]. Another interesting feature is that open hardware allows transforming any microscope into an OPT instrument [52] or building one from the ground up [45]. Moreover, improved reconstruction methods can provide an increase in the resolution [53, 54].

In this thesis, we developed a custom OPT instrument for whole mouse organ imaging [55]. We characterized the instrument using fluorescent microparticles, and we investigated the influence of the number of projections on the final image. Finally, we evaluated the use of OPT in Alzheimer's disease (AD) research in a preliminary cross-sectional study with mice.

Alzheimer's disease

AD is a neurodegenerative disorder and the most prevalent cause of dementia [56]. Dementia is a syndrome altering functional, cognitive, and behavioral ability, hampering independent living capacity, and ultimately leading to death [57]. In 2001, a panel of 12 experts estimated 24.3 million people with dementia worldwide and projected 4.6 million new cases each year [58]. The same experts also predicted that the increase in new cases will double every 20 year and that by 2040 dementia will affect 81.1 million people. Another study reported a projection of 106.2 million people with AD in 2050, confirming the alarming numbers [59] and making AD a public health priority [60].

In 2011, a review of the diagnostic guidelines for AD, established in 1984 [61], suggested that the clinical diagnosis of AD, based on multiple information such as medical history, cognitive and personality tests, etc., had a sensitivity of 81 % and a specificity of 70 % based on 27 years of experience [62]. Additionally, there can be a long period between the earliest pathogenic events in the brain of an AD patient and the first evidence of cognitive decline; this is referred to as the *preclinical states* of AD [63]. The preclinical states of AD are asymptomatic and, in some cases, will remain so until the patient's death. In this case, only a diagnosis *post mortem* can unveil the characteristic brain lesions.

Two hallmark proteins have been identified in the brain of AD patients: the amyloid-β and tau protein [64]. In this thesis, we focus on the amyloid-β and the amyloid cascade hypothesis [65, 66]. Amyloid-β is the principal component of amyloid plaques, which deposit in the extracellular space in the form of small aggregates from 10 to 100 µm in size. In the amyloid cascade hypothesis, it is believed that amyloid plaques are the crucial event of AD pathology. In this regard, the visualization of amyloid plaques plays a pivotal role in AD research, as illustrated in Figure 1.2.

The recent development of the Pittsburgh Compound-B (PIB) in 2004 [67] revolutionized *in vivo* imaging of amyloid pathology in humans with PET (Figure 1.2(a)). There have been efforts to incorporate PET of amyloid-β in the clinical diagnosis of AD, and its importance regarding asymptomatic preclinical states has been highlighted [69] as previous guidelines failed to establish a diagnostic before the patient's death. The binding of PIB to amyloid-β assemblies is well characterized [70], and the tracer design gives the specific spatial representation of the amyloid burden in PET images. However, the resolution of PET is insufficient to study individual amyloid plaques, which is rather performed on transgenic mouse models [71].

In histopathology, the brain is mechanically sliced and marked with probes of amyloid plaques [72]. The tissue sections are then imaged with a widefield microscope (Figure 1.2(b) and (c)). The resolution of modern microscopes allows visualizing individual amyloid plaques, but histopathology is rarely applied in 3D and suffers from cutting artefacts due to mechanical slicing. Additionally, histopathology is performed *ex vivo*.

Ultramicroscopy can provide whole 3D images of *ex vivo* AD mouse brains using an amyloid-

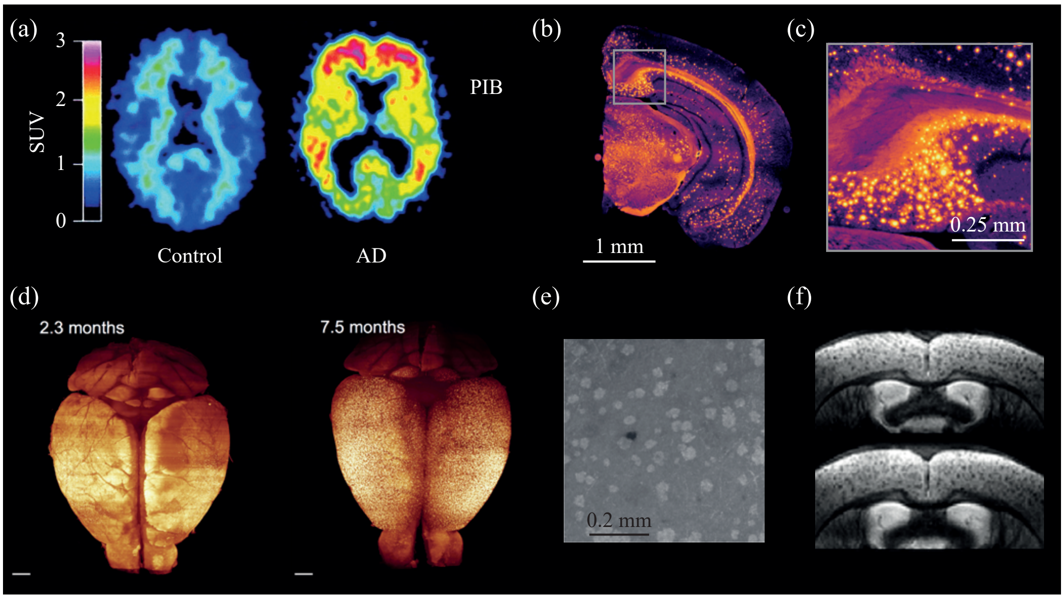

Figure 1.2 – Amyloid plaque imaging. (a) *in vivo* PET images of human subjects with Pittsburgh Compound-B (edited from Figure 4 in the work of Klunk *et al.* [67]). Left: 67-year-old healthy control subject; right: 79-year-old AD patient. (b) Histological section from a mouse brain of an AD model marked for amyloid plaques. (c) Corresponding zoom in the histological section. (d) Ultramicroscopy images of AD mouse brains at different age and marked for amyloid plaques (edited from Figure 3 in the work of Jährling *et al.* [43]). Scale bar: 1 mm. (e) OCM image of amyloid plaques in an AD mouse brain with intrinsic contrast (edited from Figure 3 in the work of Bolmont *et al.* [68]). (f) Micro-MRI images of plaques with intrinsic contrast in AD mouse brains (edited from Figure 3 in the work of Jack *et al.* [28]).

probe (Figure 1.2(d)) with cellular resolution [43]. OCM can perform 3D intrinsic imaging of the plaques in regions of interest of an AD mouse brain *in vivo* [68] (Figure 1.2(e)) but is hardly applicable to a whole mouse brain. Micro-MRI also shows an *in vivo* intrinsic contrast of the amyloid plaques in whole AD mouse brains [28] in 3D. However, to the best of our knowledge, there has not been an attempt to image amyloid plaques in the whole brain of an AD mouse with OPT.

Main contributions

The main scientific contributions of this thesis consist of three first author papers, each composing a chapter (Chapter 3-5).

In the first research article by D. Nguyen, P. J. Marchand, A. L. Planchette, J. Nilsson, M. Sison, J. Extermann, A. Lopez, *et al.* called “Optical projection tomography for rapid whole mouse brain imaging” published in Biomedical Optics Express [55], a custom OPT instrument designed for whole mouse organ imaging is described. The OPT instrument can image samples as large as 8 cm^3 with a resolution of approximately 30 µm in a matter of minutes. Additionally, sample preparation is described and includes an optimized clearing protocol, the duration of which is reduced to a couple of days instead of weeks. Finally, images of the mouse brain neuroanatomy, vasculature, and amyloid plaque demonstrate the instrument performance.

In the second research article by D. Nguyen, O. Martin, A. C. Descloux, D. Van De Ville, T. Lasser, and A. Radenovic called “Practical aspects of optical projection tomography imaging exemplified with whole mouse organs” submitted to Optics Express (December 2018), several practical considerations related to the use of OPT are investigated. A new agarose embedding protocol, which standardizes sample preparation and reduces the risk of image artefacts, is detailed. Images of fluorescent microparticles are shown in view of understanding the instrument specifications, and the effect of the number of projections on the reconstructed image quality is studied.

In the last research article by D. Nguyen, V. Uhlmann, A. L. Planchette, P. J. Marchand, D. Van De Ville, T. Lasser, and A. Radenovic called “Supervised learning to quantify amyloidosis in whole brains of an Alzheimer’s disease mouse model acquired with optical projection tomography” submitted to Biomedical Optics Express (December 2018), OPT images of amyloid plaques in whole mouse brain are quantified relying on a supervised learning algorithm to evaluate the disease progression in a preliminary cross-sectional study.

Thesis organization

In Chapter 2, the general theory of tomographic reconstruction is introduced, and the filtered back-projection algorithm is derived. Then, the use of optical projections in tomographic reconstruction and underlying artefacts that might arise are discussed. In Chapter 3, the implementation of a custom OPT instrument designed for whole mouse organ imaging is described in the form of a first research article. This work also showcases whole mouse brain imaging of the neuroanatomy, vasculature, and amyloid plaques, together with the corresponding sample preparation protocols. Practical aspects of OPT acquisition are examined in Chapter 4. This second research article includes a new agarose embedding protocol, images of fluorescent microparticles, and an evaluation of the influence of the number of projections on the reconstructed image quality. In Chapter 5, OPT is combined with supervised learning to quantify the progression of amyloidosis in mouse brains of an Alzheimer’s disease model in a third research article. Preliminary results to bridge imaging scales by merging OPT with structured illumination microscopy are presented in Chapter 6. The remaining challenges are discussed with a focus on optical aberrations arising in whole mouse organ imaging, and the thesis concludes with a personal paragraph summarizing my work at the Laboratoire d’Optique Biomédicale. Finally, a collection of unpublished images are showcased in a portfolio gallery in Appendix A.

2 OPT theory, algorithm, and practical aspects

Fully grasping the 3D representation of an object is an ambitious exercise. Instead, we prefer to understand the spatial nature of things by looking at their cross-sections. Think of the floor plan of a building or a technical drawing in a user manual. We call “tomography” the range of techniques that can produce 3D images of objects in cross-sections. From that definition, it follows that optical projection tomography (OPT) is the reconstruction of 3D images in cross-sections based on optical projections of a sample. A projection is the flattened representation of an object via a physical phenomenon. For example, the shadow we cast on the floor is a projection resulting from sunlight absorption and reflection by our body. Projections differ from cross-sections in the sense that they are not a strict representation of the object in a plane of observation. Instead, they describe the response to a physical phenomenon from a certain point of view. In the shadow example, it is deformed by the sun’s position and changes throughout the day. For optical projections, the physical phenomena are essentially light absorption and fluorescence emission.

In this Chapter, I introduce a general scheme for tomographic reconstruction (Section 2.1) adapted from the book of Kak and Slaney [73]. This scheme has notably been applied to X-ray computed tomography (CT), and I will discuss it first in that context. I will start with a mathematical definition of the projection process, also known as the Radon transform (Section 2.1.1). I will pursue with the central slice theorem (Section 2.1.2), another essential result to understand tomographic reconstructions. Then, I will present the classical tomographic reconstruction scheme (Section 2.1.3), called filtered back-projection (FBP). I will also discuss the peculiarities of optical projections, how to implement tomographic reconstruction in OPT (Section 2.2), and the possible image artefacts that might arise (Section 2.2.1). Finally, I will give some details about the practical aspects of OPT and in particular the optional optical clearing necessary for opaque samples (Section 2.3). These aspects will be further discussed in a dedicated chapter (Chapter 4).

2.1 Tomographic reconstruction

Our journey to understanding tomographic reconstruction begins with the concept of radiographs. A radiograph is a photographic film that was exposed to X-rays passing through a specimen. Being initially transparent, the film darkens upon an increasing X-rays exposure. Hard tissues, such as bones, absorb a substantial amount of radiation, leaving transparent zones on the film. Soft tissues such as organs, in contrast, have lower radiation absorption, resulting in translucent shades on the film. Radiographers then place the exposed film over a homogenous light-emitting surface to appreciate the different contrasts in view of a patient's diagnosis. A radiograph is, therefore, a projection based on X-ray absorption in a specimen. This physical phenomenon is described by the Beer-Lambert law [74] as

$$A = \log_{10} \frac{I_0}{I} = \mu l, \tag{2.1}$$

where A is the absorbance, I_0 is the initial radiation intensity, I is the radiation intensity after a distance l traveled inside the specimen, and μ is a specimen-and-radiation-dependant absorption coefficient. In Section 2.1.1, we derive a mathematical formulation for the generation of projections which captures the problem of radiography.

2.1.1 Radon transform

The Radon transform, defined as

$$P_\theta(t) = \iint_{-\infty}^{\infty} f(x, y)\delta(x\cos\theta + y\sin\theta - t)\mathrm{d}x\mathrm{d}y, \tag{2.2}$$

with δ the Dirac impulse, transforms a 2D function f, with spatial coordinates (x, y), into a line integral P_θ, with remaining spatial coordinate t, along a straight direction given by arbitrary angle θ. This transform was first introduced by the Austrian mathematician J. Radon in 1917 [75] and sets a formalism for the generation of projections. An illustration of the Radon transform applied to a mouse brain section is shown in Figure 2.1. In this example, parallel X-rays, represented by gray arrows, traverse the sample $f(x, y)$ at an arbitrary angle θ. Each ray accumulates the values of f in its direction of propagation and determines the value $P_\theta(t)$ of the line integral at the corresponding position t. This line integral is a 1D radiograph of the mouse brain section, and P_θ describes the absorbance of X-rays under an angle θ. In 3D, the radiograph of a specimen is a 2D image composed of the 1D radiographs of each of its sections.

Figure 2.1 also depicts the fundamental limitation of radiographs, which is that the projection

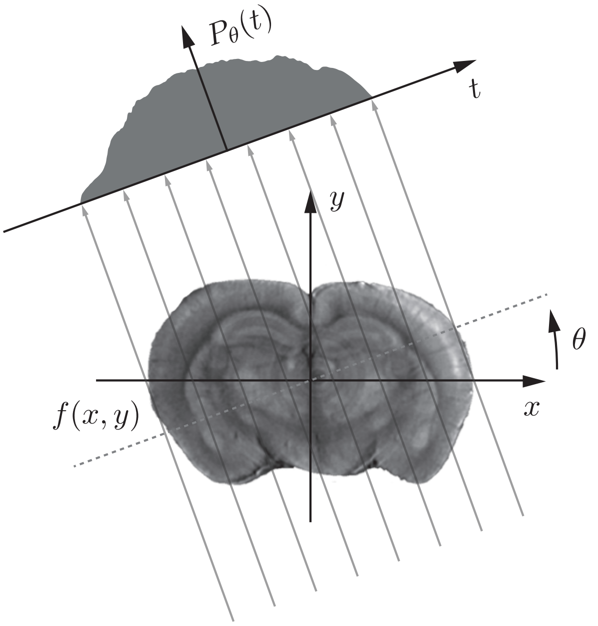

Figure 2.1 – Illustration of the Radon transform. A 2D section of a mouse brain f is projected to a line integral P_θ at arbitrary angle θ.

is made at the expense of a reduction in data dimensionality materialized by a loss of depth information. In other words, it is impossible to know which depth of the brain section contributed most to a given value $P_\theta(t)$ in the line integral. Similarly, it is unrealistic to deduce the morphology of a person based solely on the shadow cast on the floor at one point in time. The inclusion of a time notion was intentional here because if that person starts to move and turns herself or himself around, we can get a better feeling for morphology by looking at the shadow over time. This is the underlying concept of CT.

In CT, a collection of projections are acquired at different angles over 180° to recover the otherwise lost depth information. The intuition that the 3D nature of an object can be retrieved based on projections at different angles is formalized by the direct inversion of the Radon transform, *i.e.*,

$$f_{bp}(x,y) = \int_0^\pi P_\theta(x\cos\theta + y\sin\theta)\mathrm{d}\theta, \tag{2.3}$$

where f_{bp} is the reconstructed specimen section, also called the “back-projection”. By applying this inversion to each section, a 3D image of the specimen can be reconstructed. The back-projection of a single specimen section is illustrated in Figure 2.2. The acquisition of three mouse brain projections is shown by the line integrals $P_{\frac{1}{9}\pi}$, $P_{\frac{4}{9}\pi}$, and $P_{\frac{7}{9}\pi}$ in Figure 2.2(a). These projections are then back-projected in the reconstruction space in Figure 2.2(b). In this process, each projection is replicated throughout the reconstruction space in its direction of acquisition. This is carried out because the depth information has been lost and it is impossible to determine from which depth each contribution to the line integral originated from. Finally, in Figure 2.2(c), a back-projection from 600 projections separated by 0.3° is shown. The result is a blurred reconstruction of the original specimen section. While the overall morphology can be deduced, from that image, fine details disappear. The principal method to circumvent this issue is to incorporate an additional filtering step in the back-projection operation. Before diving into the details of the filtered back-projection, another essential mathematical result is needed. This result is known as the central slice theorem (Section 2.1.2), also sometimes called the projection slice theorem or the Fourier slice theorem.

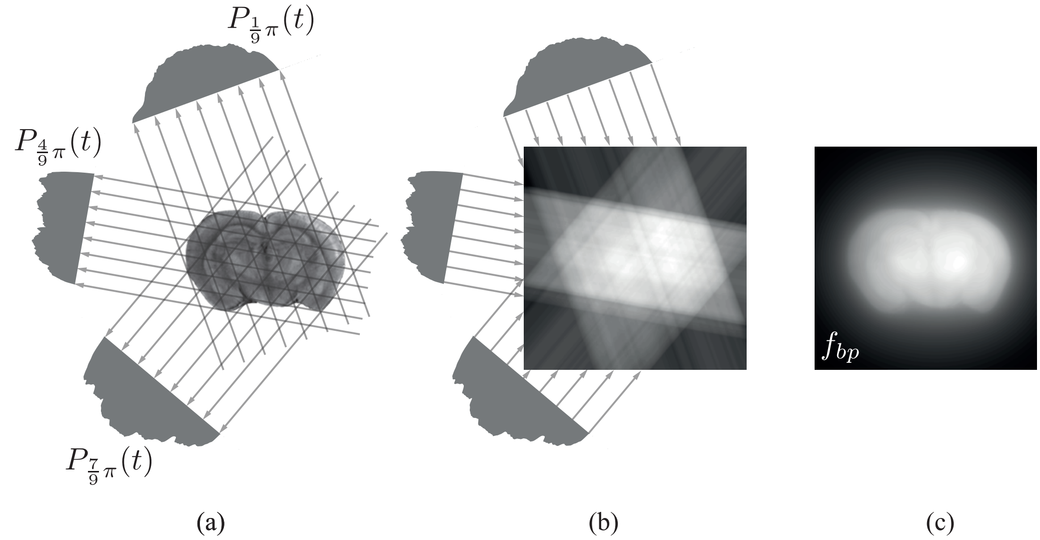

(a) (b) (c)

Figure 2.2 – (a) Acquisition of three mouse brain projections, represented by the line integrals $P_{\frac{1}{9}\pi}$, $P_{\frac{4}{9}\pi}$, and $P_{\frac{7}{9}\pi}$, at corresponding angles $\frac{1}{9}\pi$, $\frac{4}{9}\pi$, and $\frac{7}{9}\pi$ in radians. (b) Direct inversion of the Radon transform from the three projections. Each projection is copied along the direction of acquisition throughout the whole depth of the reconstruction space. This process is referred to as back-projection. (c) Back-projection of the mouse brain section based on 600 projections separated by 0.3°, the result is a blurred image of the mouse brain section.

2.1.2 Central slice theorem

The central slice theorem relates the Fourier transform to the Radon transform, and is stated as

$$\hat{f}_{\mathrm{pol}}(\omega,\theta) = \hat{P}_{\theta}(\omega), \tag{2.4}$$

where $\hat{f}_{\text{pol}}$ is the 2D Fourier transform of a section in polar coordinates (ω,θ), and $\hat{P}_\theta$ is the 1D Fourier transform of the line integral from the Radon transform at corresponding angle θ. The proof of this theorem is given here for $\theta = 0$.

Proof. The definition of the 2D Fourier transform in polar coordinates is expressed as

$$\hat{f}_{\text{pol}}(\omega,\theta) = \iint_{-\infty}^{\infty} f(x,y)\mathrm{e}^{-\mathrm{j}\omega(x\cos\theta + y\sin\theta)}\mathrm{d}x\mathrm{d}y. \tag{2.5}$$

When $\theta = 0$, (2.5) becomes

$$\hat{f}_{\text{pol}}(\omega,0) = \iint_{-\infty}^{\infty} f(x,y)\mathrm{e}^{-\mathrm{j}\omega x}\mathrm{d}x\mathrm{d}y. \tag{2.6}$$

Since there is only an x-dependency in the exponential factor, the integration order in (2.6) can be rearranged as

$$\hat{f}_{\text{pol}}(\omega,0) = \int_{-\infty}^{\infty} \left(\int_{-\infty}^{\infty} f(x,y)\mathrm{d}y\right)\mathrm{e}^{-\mathrm{j}\omega x}\mathrm{d}x, \tag{2.7}$$

where the parentheses denote the line integral of f at $\theta = 0$. Therefore, (2.7) becomes

$$\hat{f}_{\text{pol}}(\omega,0) = \int_{-\infty}^{\infty} P_0(x)\mathrm{e}^{-\mathrm{j}\omega x}\mathrm{d}x, \tag{2.8}$$

where the x- and $t-$coordinates of the Radon transform (2.2) are confounded. Finally, what remains on the right-hand side of (2.8) is the definition of the 1D Fourier transform of the line integral that is

$$\hat{f}_{\text{pol}}(\omega,0) = \hat{P}_0(\omega). \tag{2.9}$$

□

This proof holds without loss of generality to other values of θ thanks to the rotation properties of the Fourier transform.

The central slice theorem tells us that an infinite number of Fourier-transformed line integrals are equivalent to the 2D Fourier transform of an object section f. Since the inversion of the Fourier transform is a well-known result of mathematics, the central slice theorem gives us a different way of reconstructing the object section. Indeed, we can acquire line integrals from an object, apply a Fourier transform to each of them, compose a 2D spectrum, and then use an inverse Fourier transform in 2D. This algorithm is also referred to as direct Fourier reconstruction. In practice, the number of line integrals we can acquire is finite, and the Fourier space is interpolated, which is a delicate operation prone to artefacts during the reconstruction [76]. However, the central slice theorem provides a framework to filter line integrals in the Fourier domain, which leads us to the filtered back-projection algorithm.

2.1.3 Filtered back-projection

The filtered back-projection algorithm is the most used approach for tomographic reconstruction. It can be derived from the definition of the 2D inverse Fourier transform

$$f(x,y) = \frac{1}{(2\pi)^2} \iint_{-\infty}^{\infty} \hat{f}(\omega_x,\omega_y) \mathrm{e}^{\mathrm{j}(\omega_x x+\omega_y y)} \mathrm{d}\omega_x \mathrm{d}\omega_y, \tag{2.10}$$

where $\hat{f}$ is the 2D Fourier transform of f in Cartesian spatial frequencies (ω_x,ω_y). This 2D Fourier transform can be rewritten in polar coordinates in (2.10), which leads to

$$f(x,y) = \frac{1}{(2\pi)^2} \int_0^{2\pi} \int_0^{\infty} \omega \hat{f}_{\mathrm{pol}}(\omega,\theta) \mathrm{e}^{\mathrm{j}\omega(x\cos\theta+y\sin\theta)} \mathrm{d}\omega \mathrm{d}\theta, \tag{2.11}$$

where $\omega = \sqrt{\omega_x^2+\omega_y^2}$, $\theta = \arctan\frac{\omega_y}{\omega_x}$, and $\omega \mathrm{d}\omega \mathrm{d}\theta = \mathrm{d}\omega_x \mathrm{d}\omega_y$. Using the central slice theorem (2.4), (2.11) becomes

$$f(x,y) = \frac{1}{(2\pi)^2} \int_0^{2\pi} \int_0^{\infty} \omega \hat{P}_\theta(\omega) \mathrm{e}^{\mathrm{j}\omega(x\cos\theta+y\sin\theta)} \mathrm{d}\omega \mathrm{d}\theta. \tag{2.12}$$

The next step in the derivation of the FBP algorithm is to split the integration over θ in (2.12) in order to get an integration span from 0 to π. Assuming $f(x,y) = i_1 + i_2$, we can write

$$i_1(x,y) = \frac{1}{(2\pi)^2} \int_0^{\pi} \int_0^{\infty} \omega \hat{P}_\theta(\omega) \mathrm{e}^{\mathrm{j}\omega(x\cos\theta+y\sin\theta)} \mathrm{d}\omega \mathrm{d}\theta, \tag{2.13}$$

and

$$i_2(x,y) = \frac{1}{(2\pi)^2}\int_{\pi}^{2\pi}\int_0^{\infty}\omega\hat{P}_\theta(\omega)\mathrm{e}^{\mathrm{j}\omega(x\cos\theta+y\sin\theta)}\mathrm{d}\omega\mathrm{d}\theta. \tag{2.14}$$

A change of variables in (2.14) allows us to integrate θ over the interval $[0,\pi[$ as

$$i_2(x,y) = \frac{1}{(2\pi)^2}\int_0^{\pi}\int_0^{\infty}\omega\hat{P}_{\theta-\pi}(\omega)\mathrm{e}^{\mathrm{j}\omega\left(x\cos(\theta-\pi)+y\sin(\theta-\pi)\right)}\mathrm{d}\omega\mathrm{d}\theta. \tag{2.15}$$

We can then rewrite (2.15) as

$$i_2(x,y) = \frac{1}{(2\pi)^2}\int_0^{\pi}\int_0^{\infty}\omega\hat{P}_{\theta-\pi}(\omega)\mathrm{e}^{-\mathrm{j}\omega(x\cos\theta+y\sin\theta)}\mathrm{d}\omega\mathrm{d}\theta. \tag{2.16}$$

Besides, it can be shown that

$$\hat{P}_{\theta-\pi}(\omega) = \hat{P}_\theta(-\omega). \tag{2.17}$$

Proof. Using (2.4) we can rewrite the left-hand side of (2.17) as

$$\hat{P}_{\theta-\pi}(\omega) = \hat{f}_{\mathrm{pol}}(\omega,\theta-\pi). \tag{2.18}$$

From the definition in (2.5), the right-hand side of (2.18) becomes

$$\begin{aligned}\hat{f}_{\mathrm{pol}}(\omega,\theta-\pi) &= \iint_{-\infty}^{\infty} f(x,y)\mathrm{e}^{-\mathrm{j}\omega\left(x\cos(\theta-\pi)+y\sin(\theta-\pi)\right)}\mathrm{d}x\mathrm{d}y\\ &= \iint_{-\infty}^{\infty} f(x,y)\mathrm{e}^{\mathrm{j}\omega(x\cos\theta+y\sin\theta)}\mathrm{d}x\mathrm{d}y\\ &= \hat{f}_{\mathrm{pol}}(-\omega,\theta).\end{aligned} \tag{2.19}$$

Using again (2.4), we can rewrite the right-hand side of (2.19) as

$$\hat{f}_{\mathrm{pol}}(-\omega,\theta) = \hat{P}_\theta(-\omega). \tag{2.20}$$

Therefore, by combining (2.18), (2.19), and (2.20) we get

$$\hat{P}_{\theta-\pi}(\omega) = \hat{P}_\theta(-\omega). \tag{2.21}$$

$\square$

So that (2.16) becomes

$$i_2(x,y) = \frac{1}{(2\pi)^2}\int_0^\pi \int_0^\infty \omega \hat{P}_\theta(-\omega)\mathrm{e}^{-\mathrm{j}\omega(x\cos\theta + y\sin\theta)}\mathrm{d}\omega\mathrm{d}\theta. \tag{2.22}$$

Then, a last change of variable allows us to integrate ω from $-\infty$ to 0 as

$$i_2(x,y) = \frac{1}{(2\pi)^2}\int_0^\pi \int_{-\infty}^0 (-\omega)\hat{P}_\theta(\omega)\mathrm{e}^{\mathrm{j}\omega(x\cos\theta + y\sin\theta)}\mathrm{d}\omega\mathrm{d}\theta. \tag{2.23}$$

We can now rewrite (2.12) as the sum of (2.13) and (2.23) as

$$f(x,y) = \frac{1}{(2\pi)^2}\int_0^\pi \int_{-\infty}^\infty |\omega|\hat{P}_\theta(\omega)\mathrm{e}^{\mathrm{j}\omega(x\cos\theta + y\sin\theta)}\mathrm{d}\omega\mathrm{d}\theta, \tag{2.24}$$

which is the FBP. It is equivalent to a back-projection (2.3), where each line integral is Fourier-transformed, multiplied by a term $|\omega|$, and transformed back to the spatial domain, exactly as in a filtering operation. The filter transfer function H, defined as

$$H(\omega) = |\omega|, \tag{2.25}$$

describes a ramp emphasizing high spatial frequencies in the line integrals and compensating for the blurring occurring in the back-projection process. This filter is also known as the

Ram-Lak filter (see Figure 2.3).

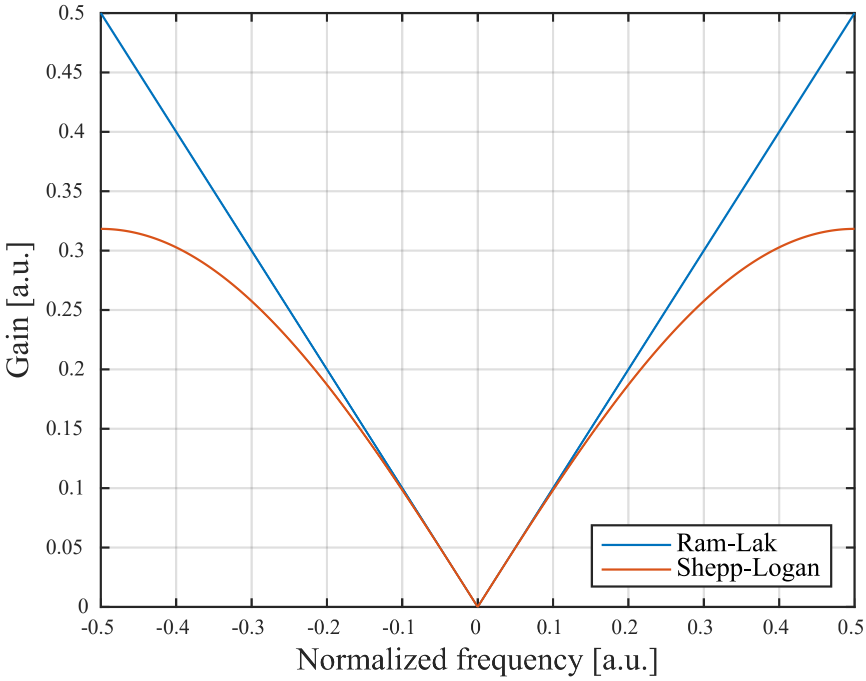

Figure 2.3 – Plot of the FBP filters transfer function. The Ram-Lak filter is used to reconstruct an image from noiseless projections. It linearly emphasizes the high spatial frequencies in the line integrals to retrieve a sharp reconstruction after back-projection. In practice, projections are usually corrupted by high-spatial-frequency noise, which would be amplified by the Ram-Lak filter. To mitigate this effect, the Shepp-Logan filter can be used. It is the Ram-Lak filter windowed by a cardinal sine function, which attenuates the gain in the very high spatial frequencies.

The FBP algorithm is illustrated in Figure 2.4. A specimen section, such as a mouse brain (Figure 2.4(a)) is Radon-transformed at multiple angles over 180°. The resulting line integrals form the columns of a matrix called a sinogram (Figure 2.4(b)). A ramp filters the sinogram in the Fourier domain (Figure 2.4(c)), and is then back-projected to retrieve a sharp reconstruction of the specimen section (Figure 2.4(d)). Practically, the FBP algorithm is implemented with a finite number of line integrals, and spatial-domain-interpolation is required to fill the reconstruction space consistently. Throughout this work, we use linear interpolation for this purpose. Moreover, the Ram-Lak filter is an ideal filter, which does not account for noise in the projections. Indeed, the high-frequency-noise recorded during the acquisition of projections is intensified by the ramp $|\omega|$. Therefore, FBP filters are usually combined with a window function that attenuates the gain in the highest spatial frequencies. In the remainder of this work, we use the Shepp-Logan filter (see Figure 2.3), which is a combination of the ramp with a cardinal sine function. The Shepp-Logan filter transfer function H_{SL} is defined as

$$H_{SL}(\omega) = |\omega|\text{sinc}(\omega). \tag{2.26}$$

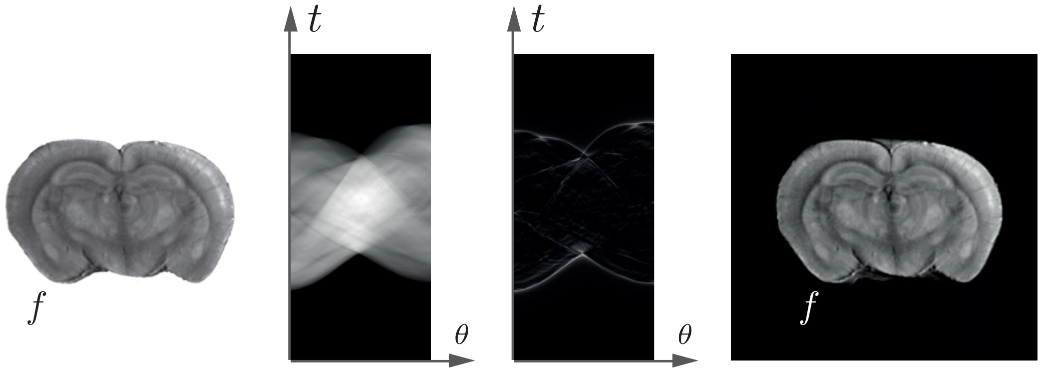

(a) (b) (c) (d)

Figure 2.4 – Main steps of the filtered back-projection algorithm. (a) Multiple line integrals from a specimen section are acquired. (b) Each line integral is placed in the columns of a matrix called a sinogram. (c) The sinogram is filtered column by column in the Fourier domain with a ramp. (d) The back-projection of the filtered sinogram results in a sharp reconstruction of the specimen section.

The given description of the FBP algorithm holds for X-ray CT with parallel beams. In Section 2.2, I explain how OPT differs from CT. Then, I discuss how the optical projections are realized and what consequences they have on the sample preparation. Finally, I introduce the requirements that allow us to use the FBP algorithm with optical projections.

2.2 Optical projections

The essential difference between X-ray CT and OPT is the source radiation spectrum. In OPT, it is the visible light spectrum (400-700 nm). Working with visible light is usually safer than X-rays, and it is less cumbersome to manipulate. On the other hand, it has a shallower penetration depth in tissues, around 10-20 µm [12]. To enhance the penetration depth in opaque and semi-transparent samples, such as rodent organs, optical clearing methods are needed [77]. There are two fundamental ways of generating optical projections with visible light.

First, white light can be shined through the sample and detected on a camera with appropriate imaging optics. This is known as the absorption mode of OPT (Figure 2.5(a)). In this mode, light is absorbed in a different amount by the tissues it has to traverse following a Beer-Lambert law. Depending on the tissue thickness and density, various shades of gray will appear on the detector with a white background where no absorption occurs. Similarly to X-ray CT, the absorption mode of OPT is intrinsically unspecific. There exist some ways of staining the samples which can give additional contrast in the projections [9], but these are not commonly used.

This lack of specificity brings us to the fluorescence mode of OPT (Figure 2.5(b)). In this mode, an excitation beam is shined orthogonally to the detection optics to trigger the fluorescence of a marker or the endogenous tissue fluorescence. The fluorescence signal is then recorded on the detector. The resulting projection is mostly dark with bright regions where the fluorophores are. The fluorescence mode of OPT can be combined with the multitude of fluorescent markers that exist among the life science community. In the remainder of this work, I will concentrate on the fluorescence mode due to its high specificity.

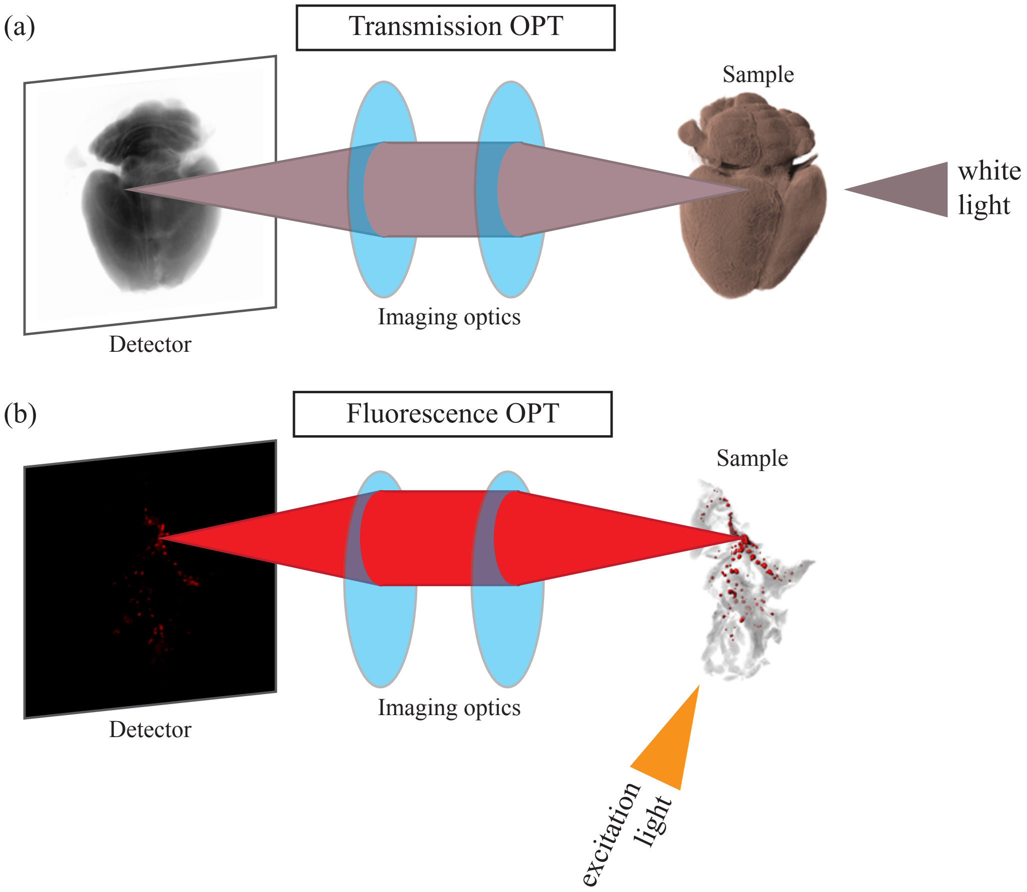

Figure 2.5 – The different operating modes of OPT. (a) In transmission OPT, white light is shined through the sample. Dense tissue regions absorb a significant amount of light and result in lower intensity values on the detector. (b) In fluorescence OPT, excitation light is generally shined on the side of the sample to generate a fluorescent signal from tissues (autofluorescence) or specific markers. The higher the fluorescence signal, the higher the intensity values on the detector.

Then, I want to give a few words on the imaging optics and what is needed to be able to use the FBP algorithm in OPT. First, the depth of field (DOF) need to be equivalent to the maximum sample thickness. In Inoué and Spring [78], the DOF is defined as

$$\mathrm{DOF} = n\left(\frac{\lambda}{\mathrm{NA}^2} + \frac{e}{M \cdot \mathrm{NA}}\right), \tag{2.27}$$

where n is the surrounding medium refractive index, λ the emission wavelength, e the pixel size in the detector plane, M the system magnification, and NA the numerical aperture of the system. In this definition, we observe that the DOF inversely depends on NA. However, we also know that the resolution of an optical system, which can be defined by the Airy radius r, depends on NA as

$$r = \frac{\lambda}{2 \cdot \mathrm{NA}}. \tag{2.28}$$

Therefore, to reach a certain DOF, the resolution has to be reduced (the value of r increases). In practice, the loss of resolution is mitigated by keeping only the front part of the specimen in focus while rotating over 360° instead of 180°.

Second, we need to conserve the system magnification throughout the detection axis. This property of optical systems is known as telecentricity. It guarantees that two objects of the same size will appear with the same size on the detector independent of their position along the detection axis. Our eyes, for example, are not telecentric. If we see two people at a different distance from us, the person farther will appear smaller. This is not desirable in OPT as we want to have a strict representation of our sample with constant magnification. Telecentricity is achieved by having the image of the system aperture located at infinity. However, even with perfect telecentricity and sufficient DOF, artefacts might still arise in OPT images.

2.2.1 Image artefacts

We will now discuss some of the relevant image artefacts that might arise in fluorescence OPT images based on the work of Walls *et al.* [79].

First, the stability of the light source is a considerable cause of image artefacts in OPT (see Figure 2 in the work of Walls *et al.* [79]). While a majority of fluorescence OPT system use mercury arc gas discharge lamps, some designs take advantage of light emitting diodes (LEDs) [80]. LEDs generally have better stability, and fluctuations are avoided by using quality power supplies [81].

Second, photobleaching can cause a signal decay over the acquisition of multiple projections

(Figure 3 in the work of Walls *et al.* [79]). This decay can be corrected by multiplying each projection by a correction factor corresponding to the exponential decay. However, this also causes an increase in the noise level.

Third, individual pixel variations in photon response can cause ring artefacts (Figure 2.6(a)). In the worst case, "bad" pixels will always take the maximum or minimum value of the detector dynamic range causing white and black rings to appear in the reconstructed image. Ring artefacts can be reduced by applying a median filter to each projection, also decreasing the resulting imaging resolution (Figure 2.6(b)).

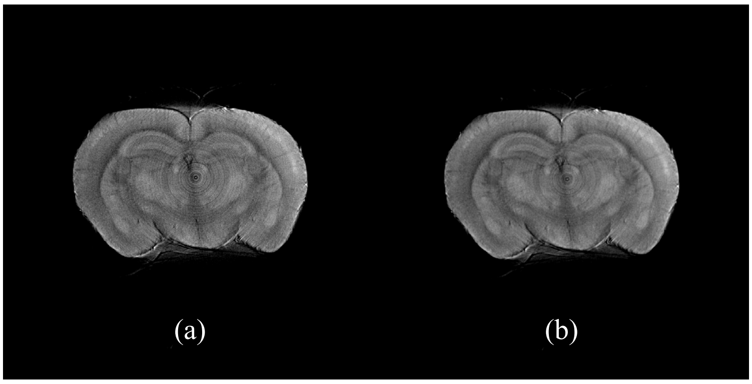

Figure 2.6 – Illustration of ring artefacts caused by pixel-to-pixel variations in photon response. (a) Original OPT reconstruction of a mouse brain highlighting the characteristic circles emanating from the center of the image. (b) Result of the apodization of the ring artefacts by applying a median filter to each projection.

Lastly, precise knowledge of the position of the center of rotation is essential to perform accurate reconstructions of the specimen. This can be done by iteratively applying the FBP with different centers of rotation and each time trying to maximize the reconstructed image variance [82]. This procedure has a sub-pixel accuracy and guarantees a good reconstruction quality. However, multiple reconstructions of the same image have to be performed which is time-consuming and requires sufficient computer power.

2.3 Practical aspects

OPT imaging of whole mouse organs is often performed *ex vivo* [47, 50]. To extract the organs, the mouse is deeply anesthetized, and an operation called "transcardiac perfusion" is performed [83]. To put it briefly, after verification of the depth of anesthesia using the toe pinch-response method, precise incisions in the abdominal wall give direct access to the heart. The needle of a perfusion apparatus (usually syringes and valves) is inserted in the left ventricle, and another incision is made in the right atrium. Several milliliters of a buffer solution is perfused through the heart to wash away the blood, significantly reducing the tissue autofluorescence during imaging later. Then, a few more milliliters of a fixation solution is perfused to fix the whole mouse in a life-like state. Finally, the organs can be harvested following a protocol such as the one by Antal *et al.* [84]. In this work, we mainly harvested the mouse brain, kidney, and lung but most organs can be acquired with an OPT instrument if the magnification is adapted.

In medical CT scanners, the patient is placed on a table. Then, the source and detector are rotated around the patient to acquire the projections. In OPT, it is simpler to have the source and detector fixed while the specimen is turned, because of its size (few centimeters). The sample is firmly attached to a motorized rotation stage with glue [85, 86]. However, direct contact with glue would damage the sample. Therefore, mouse organs are mounted in an agarose gel. The gel is poured in a large petri dish with the organ, and after it cooled down, a small block containing the specimen is trimmed away.

Light penetration in mouse organs is limited to few tens of micrometers [12]. Therefore, an additional clearing step is necessary to make tissues semi-transparent in view of OPT acquisition. There exists a variety of clearing techniques [77], but one of them stands out by its simplicity and reliability in whole mouse brain preparation. This technique consists in the dehydration of the sample in ethanol for 7 days and rehydration in a 1:2 solution of benzyl alcohol and benzyl benzoate (BABB) for 2 days [33].

Finally, the last step before OPT acquisition and FBP reconstruction is to choose a number of projections which also determines the angular increment of the motor. Originally, 400 projections were used [9], and more recently, 1200 projections were tried in the mouse brain [50].

In Chapter 3, we discuss how to implement an OPT instrument with a specific resolution and DOF for large specimen (in the order of a few centimeters), while guaranteeing telecentricity. Additionally, we introduce a means of retrieving the center of rotation based on convolution between mirrored projections (separated by 180°), and an optimized clearing protocol for whole mouse brains that last approximately 3 days. We also showcase whole mouse brain images of the neuroanatomy, vasculature and amyloid plaques in a model of AD. Moreover, in Chapter 4, we present a series of improvements of the practical aspects of OPT.

3 OPT instrument design

The design of custom optical projection tomography instruments (OPT) [45, 51] allows the exploration of new biomedical imaging applications. In neuroscience, custom OPT instruments are used for neuroanatomical phenotyping of the mouse brain [50], based on tissue autofluorescence. A next step to explore in this domain is the potential application of OPT to the study of neurodegenerative diseases. In this work, a custom OPT instrument was designed for 3D whole-mouse brain imaging with fluorescent markers of vasculature and amyloidosis, the latter being a hallmark of Alzheimer's disease. It features a 17 cm^3 imaging volume with 50 µm resolution and epi-fluorescence illumination using light emitting diodes (LEDs).

Moreover, this OPT instrument has been duplicated at Lund University and is applied to the study of autoimmunity in the research group of Professor Dan Holmberg (also available to other users in the university through the OPT imaging platform web page [87]). The instrument design and underlying sample preparation protocols are the topics of a research article published in Biomedical Optics Express in 2017 [55] (doi: 10.1364/BOE.8.005637). The rest of this section is composed of the postprint version of the article, followed by a detailed list of author contributions.

3.1 OPT for rapid whole mouse brain imaging

David Nguyen[1*], Paul J. Marchand[1], Arielle L. Planchette[1], Julia Nilsson[2], Miguel Sison[1], Jérôme Extermann[1], Antonio Lopez[1], Marcin Sylwestrzak[1], Jessica Sordet-Dessimoz[1], Anja Schmidt-Christensen[2], Dan Holmberg[2], Dimitri Van De Ville[3], and Theo Lasser[1]

[1] *Laboratoire d'Optique Biomédicale, School of Engineering, École Polytechnique Fédérale de Lausanne, CH-*1015 *Lausanne, Switzerland*
[2] *Autoimmunity, Department of Experimental Medical Sciences, Lund University Diabetes Centre,* 20502 *Malmö, Sweden*
[3] *Medical Image Processing Lab, School of Engineering, École Polytechnique Fédérale de Lausanne, CH-*1202 *Genève, Switzerland*
[*] *david.nguyen@epfl.ch*

Abstract

In recent years, three-dimensional mesoscopic imaging has gained significant importance in life sciences for fundamental studies at the whole-organ level. In this manuscript, we present an optical projection tomography (OPT) method designed for imaging of the intact mouse brain. The system features an isotropic resolution of ~50 µm and an acquisition time of four to eight minutes, using a 3-day optimized clearing protocol. Imaging of the brain autofluorescence in 3D reveals details of the neuroanatomy, while the use of fluorescent labels displays the vascular network and amyloid deposition in 5xFAD mice, an important model of Alzheimer's disease (AD). Finally, the OPT images are compared with histological slices.

Introduction

Since its invention in the 19th century, histopathology has been and continues to be a widely used method for tissue-based medical diagnosis. While it excels at producing two-dimensional images of tissue sections, extracting information from whole three-dimensional tissues remains challenging. As a complement to histopathology, a new imaging regime, termed mesoscopy [12] emerged at the beginning of the century for 3D visualization of samples spanning a scale from a few millimeters to several centimeters. Over time, various techniques have been developed within this regime.

Micro-optical sectioning tomography (MOST) [88] is a block-face imaging method where the process of histology is automatized via simultaneous imaging and sectioning of the tissue. This technique has been successfully applied to image a whole mouse brain with a submicrometric resolution [89]. However, the acquisition time of approximately two weeks represents an experimental limitation for studies involving numerous animals.

Light-sheet microscopy [90] is probably the most prolific example of these mesoscopic techniques. Light-sheet microscopy performs three-dimensional imaging by scanning an engineered sheet of light orthogonal to the optical axis. This illumination mechanism achieves optical sectioning without slicing the tissue along with minimal photobleaching. The penetration depth of light-sheet microscopy is enhanced in naturally-transparent or cleared samples due to the reduction in light scattering. Recent research on light-sheet microscopy has mainly been focused on *in vivo* imaging. Improved illumination strategies (for example with optical lattices [35]), and solutions for specimen mounting in a physiological environment [40] have been developed. Additionally, the combination of light-sheet microscopy with structured illumination microscopy has increased the visibility through opaque samples [41], thus avoiding optical clearing (a process often done *ex vivo* due to its toxicity). Efforts have also been directed towards imaging larger samples, such as entire neural [33] and vascular networks [91, 92], or Alzheimer's disease (AD) hallmark amyloid deposition [43] in whole mouse brains. These particular results have helped to establish light-sheet microscopy as a tool for mouse phenotyping and investigations of disease models. Light-sheet microscopy produces outstanding 3D image quality with subcellular resolution over large volumes, which typically translates into big data sets. These require excessively long image processing time and terabytes of data handling [93]. Moreover, the optical design and image processing pipeline of such systems can be complex for inexperienced users. For these reasons, we propose optical projection tomography (OPT) as an alternative.

OPT is a three-dimensional imaging technique developed by James Sharpe in 2002 [9] for 3D microscopy and gene expression studies. Considered as an optical analogue of X-ray computed tomography (CT) [73], OPT allows sample reconstruction from projections acquired at different angles. These projections are images taken over 360°, by rotating the sample, with a depth of field (DOF) covering half the specimen. Depending on the illumination, the projections either provide information on the light absorption or the integration of a fluorescence signal through the sample [44]. In both cases, the reconstruction of inner structures strongly depends upon the sample's transparency. For enhanced penetration depths, OPT requires naturally-transparent or cleared samples. Recently, custom OPT systems have been developed [45], including helical OPT [51], where a vertical translation is introduced during the acquisition process to enable imaging of elongated samples, such as rodent spinal cords and large intestines. Along with these hardware improvements, OPT benefited from several artifact-correction [79] and resolution improvement [94] algorithms. For example, to automatically recover the center of rotation (COR) in the projections [82] or to account for fluorescence absorption in tissues with a normalized Born approach [95]. Additionally, accelerated reconstruction procedures have been achieved by taking advantage of either iterative algorithms [96], or parallel processing on the graphics processing unit (GPU) [97]. Various applications highlight the performance of OPT. These include *in vivo* imaging of the zebrafish vasculature [46], fruit fly pupae head eversion process [98], morphogenesis of salivary glands and wing imaginal discs [99], as well as fluorescence lifetime in living zebrafish embryos [100], and visualization of plant development [101, 102]. Furthermore, OPT has been used for whole organ imaging in mice to study the pancreas and beta-cell tissue in the development of diabetes [48, 49], the spinal cord and optic nerve in the development of experimental autoimmune encephalomyelitis (EAE) [103], and to perform neuroanatomical phenotyping [50, 104]. So far, OPT is limited in resolution by the depth of field required for imaging. However, its rapidity and simplicity in image acquisition and processing make OPT convenient for various routine applications.

In this paper, we present a novel OPT methodology for whole mouse brain imaging. It includes an OPT design which uses the principle of epifluorescence, a feature known to maximize the rejection of stray light and homogenize the illumination in the sample plane. In addition to the setup design, we provide an outline of the software processing and demonstrate 3D imaging of the brain with an optimized solvent-based clearing protocol. A dehydration step of a single day in 100 % methanol with one refresh in the clearing protocol is shown to be sufficient to reveal details of the mouse neuroanatomy (while several days and increasing concentration of solvent solution were previously required [33, 43, 50]). Furthermore, our sample preparation has been successfully combined with different standard labeling protocols from fluorescence imaging technology to image the vasculature of wild-type mouse brains as well as the distribution of amyloid plaques in the brain of transgenic mice that coexpress five familial AD mutations (5xFAD mice) [105], an important model of the disease. Finally, we show a comparison of the OPT images with histological slices from the same mouse brain.

Materials and methods

Optical Projection Tomography

Our mesoscopic OPT setup (Figure 3.1) is designed for 3D imaging of whole intact mouse brains. As shown in blue in Figure 3.1(A) and 3.1(B), the detection arm consists of a 4f system with an objective lens L_o (f = 300 mm, AC508-300-A-ML, Thorlabs) and a tube lens L_t (f = 150 mm, AC508-150-A-ML, Thorlabs), both achromatic. This configuration results in a 0.5X magnification on the detector (ORCA-Flash 4.0 V2, Hamamatsu), providing a field of view (FOV) of 26.6 × 26.6 mm^2 over 1024 × 1024 px^2 in a 2 × 2 binning mode (initially 2048 × 2048 px^2). A DOF of approximately 15 mm (according to the definition of Inoué and Spring [106], equation 2.18) is obtained by placing a 4 mm diameter diaphragm in the rear focal plane of the objective lens, which also makes the system telecentric. The resulting numerical aperture (NA) of 0.01 provides a diffraction-limited lateral resolution of 28 µm (according to the definition of Inoué and Spring [106], equation 2.7). However, this diffraction-limited lateral resolution is currently hindered by the pixel-limited resolution of 52 µm (twice the binned pixel size). The projections are captured at angular steps of 0.3° (or 0.9° in Figure 3.6(E)) by rotating the sample over 360° *i.e.*, 1200 projections (or 400 projections in Figure 3.6(E)), in a step-and-shoot mode. The reconstruction of samples as thick as 26 mm (limited by the FOV) is typically achieved within minutes (see Table 3.1 for details on exposure and acquisition time). As illustrated in green in Figure 3.1(A), the sample is illuminated by switchable LEDs. In this manuscript, we use a 420 nm LED (M420D2, Thorlabs) and a 470 nm LED (M470D2, Thorlabs), also described in Table 3.1. These LEDs are collimated by an aspheric lens L_c (f = 16 mm, ACL25416U, Thorlabs). The resulting illumination beam is magnified by another 4f system composed of an achromatic relay lens L_r (f = 150 mm, AC254-150-A-ML, Thorlabs) and the objective lens, providing a uniform full-field illumination of the sample plane while maximizing the rejection of stray light. A kinematic fluorescence filter cube (DFM1/M, Thorlabs) is used to introduce and filter the illumination beam in the detection path (epifluorescence), and a modular LED switching mechanism (Figure 3.1(C)) allows the user to choose between different fluorescence configurations (described in Table 3.1).

Table 3.1 – OPT configuration to visualize different features of interest. Stated are LEDs, filters, exposure time, and total acquisition time. Filters references are from Chroma: EX, excitation filter; DC, dichroic mirror; EM, emission filter.

Feature *(marker)*	**Figure**	**LED**	**Filters**	**Exposure time** [s]	**Acquisition time** [min]
neuroanatomy *(autofluorescence)*	3.3	420 nm	EX, AT420/40x DC, AT455dc EM, AT465lp	0.2	4
vascular network *(FITC-albumin hydrogel)*	3.4, 3.6(B)-(C)	470 nm	EX, AT480/30x DC, AT505dc EM, AT535/40m	0.2-0.4	4-8
amyloid plaques *(Methoxy-X04)*	3.5, 3.6(E)	420 nm	EX, AT420/40x DC, AT455dc EM, AT465lp	0.15-0.3	3-6

Before imaging, the sample embedded in agarose is glued (Loctite 454, Loctite) on a holder and attached to a motorized rotation stage (8MR190-2, Standa) using a magnet, as depicted in Figure 3.1(D). The OPT imaging takes place across a cuvette (704-001-30-10, Hellma Analytics) filled with a 1:2 mixture of benzyl alcohol and benzyl benzoate (BABB) for index matching. Three motorized linear stages (8MT167-100, Standa) provide additional degrees of freedom for aligning and focusing the sample. We use the translation along the y-axis to align the rotation axis on the center of the detector, and the magnet to align the sample gravity center on the rotation axis. These alignment procedures are necessary to keep the sample within the FOV of the setup but can be carried out approximately since the COR is numerically retrieved in the reconstruction algorithm. The tilt of the rotation axis has been minimized by precisely manufacturing the custom components and does not significantly affect the reconstruction process. More control on this parameter can be achieved by adding a tip-tilt mount on the rotation stage and using the alignment protocol described by Wong *et al.* [45].

Image Processing

As illustrated in Figure 3.2, image acquisition with the OPT system produces a stack of 1200 or 400 projections, separated by the same angular distance and depicting the sample over 360°. These projections are pre-processed with Fiji [107] depending on the sample preparation. Brain autofluorescence reconstructions sometimes present ring artifacts [79], presumably due

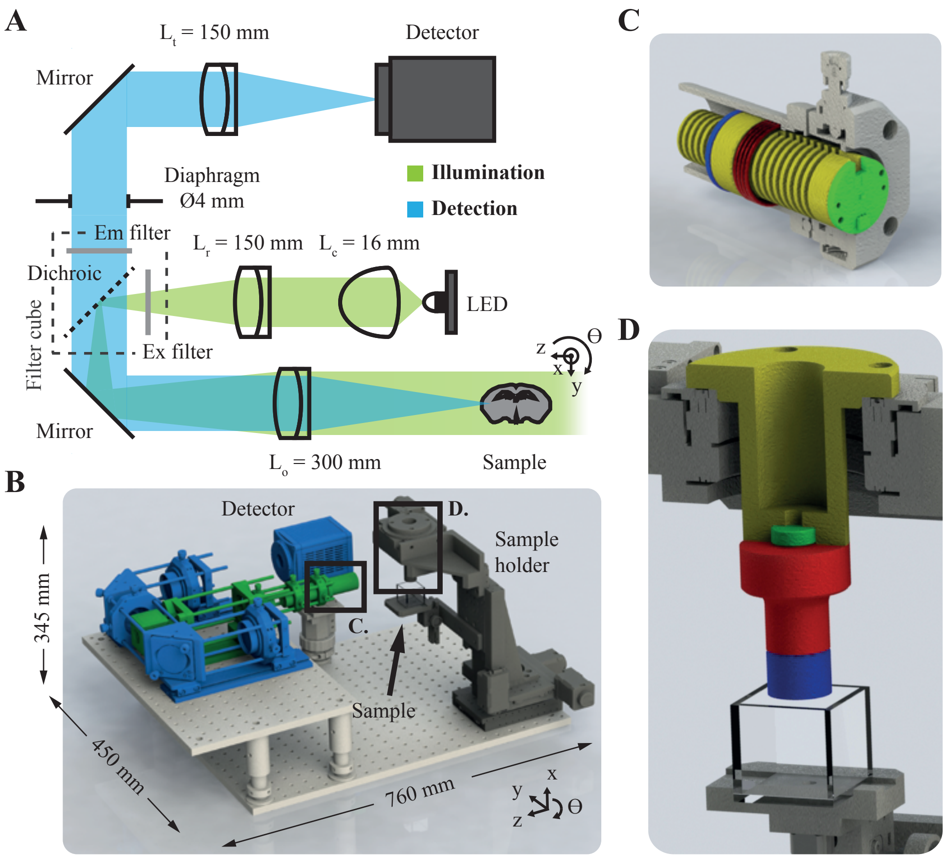

Figure 3.1 – OPT design. The optical layout (A) and the corresponding CAD rendering (B) illustrate the detection (blue) and illumination (green) arms. A detailed view of the LEDs mount (C) demonstrates the system for alignment and switching. It is composed of a custom heat sink (yellow), a spring (red, C.254.250.0250.A, Vanel), and a ring (blue, SM1RR, Thorlabs) stacked inside a 1-inch tube (SM1L20, Thorlabs) and screwed to a quick-release translation mount (CXY1Q, Thorlabs). The custom sample holding mechanism (D) consists of a base tube (yellow) glued to a magnet (green) to hold the magnetic stainless steel cylinder (red). The sample is glued to the blue cylinder which can be screwed to the whole mechanism.

to a variation in the pixels response of the camera. A median filter (3 × 3, radius 0.5 px) is applied to the projections to mitigate this effect. Vasculature-labeled brain reconstructions display an increased contrast by applying a mean filter of the same size to the projections. No pre-processing step is applied to amyloid-labeled brain projections. A line is fit on the maximum values of the convolution of the first projection I_{0° with the opposite projection I_{180° along the vertical direction. This line forms a vector containing the CORs (shown with a green dotted line in Figure 3.2), for each vertical position in the projection stack. These COR values are crucial to avoid artifacts in the reconstruction. The projection stack is transformed into a sinograms stack, by permuting the dimensions of the stack, and each sinogram is high-pass filtered with a Shepp-Logan filter. A 3D image of the sample is obtained by back-projecting each sinogram around the corresponding COR value with a linear interpolation. The sinograms' filtering and back-projection compose the conventional filtered back-projection (FBP) algorithm [73] and are implemented in CUDA (Nvidia) to take advantage of massive parallelization on the GPU. A desktop computer operated with Windows 7 Enterprise SP1 64-bit (Microsoft) and equipped with two Xeon CPU E5-2650 v2 (Intel), 64 GB DDR3 RAM, a GeForce GTX TITAN Black embedding 2880 CUDA cores, and 6 GB GDDR5 memory allows processing the samples in approximately 2 minutes for a resulting 8-bits stack of 1024 × 1024 × 1024 px^3 (around 0.5 GB in size). Finally, three-dimensional image rendering is performed with the Imaris (Bitplane) software.

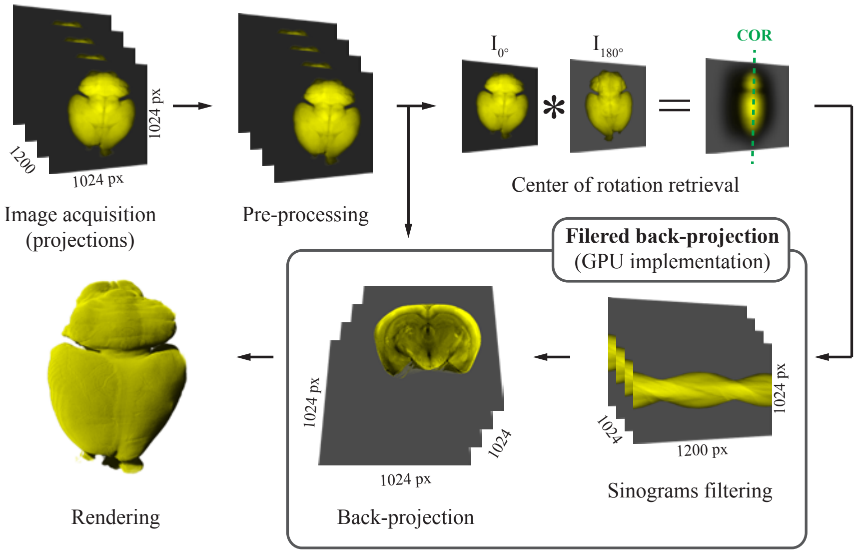

Figure 3.2 – Image processing pipeline illustrating the filtered back-projection (FBP) as well as the automatic retrieval of the COR algorithms. After a pre-processing step (described in text), the sinograms are filtered and the corresponding COR is retrieved. Following these operations, the sinograms are back-projected to form the virtual tissue sections, and 3D rendering is applied.

Mouse Model

5xFAD genetically-modified mice [105] were purchased from The Jackson Laboratory on a congenic C57BL/6J background (34848-JAX, MMRRC). They were bred and maintained in-house with SJL/J mice (000686, The Jackson Laboratory) to generate the experimental animals on a hybrid B6SJL F1 background, which demonstrates a more robust amyloid phenotype. This model of AD is extensively used in research and displays many of the phenotypes associated with the disease [105]. In particular, the mice are known to develop an early and severe amyloid deposition starting from 1.5 months of age [105].

Sample Preparation

All animal procedures were carried out according to Swiss regulations under the approval of the veterinary authority of the canton of Vaud.

Amyloid plaques labeling. Similar to the protocol reported by Jährling *et al.* [43], 5xFAD mice and their littermate controls, on a B6SJL F1 background, received two consecutive intraperitoneal (IP) injections of 30 mg/kg Methoxy-X04 (Tocris) in DMSO (10 mg/ml) with a 24-h interval. During the second injection, 100 µl (30 µg/ml) buprenorphine in 0.9 % NaCl was also administered subcutaneously (SC) for analgesia. Two hours later, the animals were deeply anesthetized IP with sodium pentobarbital (150 mg/kg) in aqueous solution (150 mg/ml). Once the depth of anesthesia was sufficient (assessed with toe pinch reflex), the animals were transcardially perfused with 2 ml of heparinized (5 I.U./ml) 1X PBS (pH 7.4), followed by 15 ml of 10 % formalin solution (HT501128, Sigma), at 4° C and 1.5 ml/min, for tissue fixation. After the perfusion, the brains were extracted and postfixed in 40 ml of formalin at 4° C overnight.

Vasculature labeling. B6SJL F1 mice were anesthetized as described above (including the injection of buprenorphine). Subsequently, an identical transcardial perfusion was performed with the additional 10 ml of hydrogel [92] at 40° C and 1.5 ml/min. The hydrogel is a mixture of 2 % (w/v) gelatin (G1890, Sigma) in 1X PBS (prepared at 60° C) and 0.1 % (w/v) FITC-conjugated albumin (A9771, Sigma) done at 40° C (0.22 µm-filtered). Before organ harvesting and fixation (as described above), the mouse head was incubated in ice-cold water for 10 minutes to solidify the hydrogel.

Organ clearing. After fixation, the organs were mounted in 1.5 % (w/v) agarose (16500500, Invitrogen) at 45° C with Milli-Q water (0.22 µm-filtered and degassed) and dehydrated in 40 ml of 100 % methanol (ME03161000, Scharlau) on a rotator (10 RPM) for 24 h with a renewal of the methanol after 15 h. Similar results (not shown here) were obtained by dehydration in ethanol. Then, the organs were transferred to a 40 ml solution of BABB (148390010 and 105860010, ACROS Organics) for optical clearing. This process can last for several days, but after approximately 48 h, the brain transparency is sufficient for imaging.

Histology. After fixation, the brains were split into hemispheres. One hemisphere was cleared and imaged with OPT. The other hemisphere was transferred to a 40 ml solution (0.22 µm-filtered) of 30 % (w/v) sucrose in 1X PBS (pH 7.4) at 4° C for approximately 48 h, or until the sample sunk at the bottom of the tube. Then the sample was partially dried on a tissue, placed in an embedding mold (such as 27112, Ted Pella Inc), and immersed in Cryomatrix (6769006, Thermo Scientific). Following the immersion in Cryomatrix, the mold was dipped in a bath of isopentane (avoid contact between Cryomatrix and isopentane) and dry ice until the Cryomatrix became completely opaque. Afterwards, the samples were stored at -80° C before slicing, with a sliding microtome, and mounting. The hemisphere sections were imaged on an Apotome (Zeiss) with a 5X, 0.15 NA air-objective, as well as a DAPI and wtGFP filter sets (for plaques and vasculature respectively). The Fiji plugin MosaicJ [108] was used to stitch the Apotome images together and create an image of the whole section.

Results and discussion

Neuroanatomy

To demonstrate the performance of our novel OPT approach, we started by clearing 2- to 8-month-old B6SJL F1 mouse brains (n>5). Figure 3.3(A) shows a representative image of a cleared brain at the age of 8 months. The transparency is sufficient to *see through* the organ and is adequate for OPT imaging (see Figure 3.3(B) and 3.3(C)). Standard BABB clearing techniques require tissue immersion in increasing series of methanol concentration for dehydration to prevent cellular distortions and excessive shrinkage of the tissue. However, we found that it is not needed for OPT as the agarose embedding acts as a protective coating. The samples are directly dehydrated in 100 % methanol, and this simplifies the clearing protocol. Although not shown in Figure 3.3, we observed shrinkage of the organs, a known side-effect of BABB clearing [109].

Images of the same 8-month-old brain were further acquired using the OPT system with the 420-nm excitation illumination, and a 3D rendering is shown in Figure 3.3(B). With its 0.5X magnification and 15-mm DOF, the setup successfully captures the whole three-dimensional nature of the organ. Individual coronal sections (Figure 3.3(C)) reveal details of the neuroanatomy down to the deepest structures. For example, the lateral (vl) and third (v3) ventricles are cavities in the brain, which get filled with BABB and therefore appear as dark regions in the sections. The caudoputamen (cp), identified through its sponge-like structure, and the thalamus (th), appear brighter. More brain regions can be identified via the different autofluorescence contrasts, such as the cortex (ctx), culmen (cul), and medial mammillary nucleus (mm), which present a higher contrast, the optic chiasms (och), which appear as a bright tube with a dark, presumably hollow, core, but also the corpus callosum (cc), the hippocampal region (hip), the inferior colliculus (ic), and the central lobule (cent). The identification of these different brain regions using the autofluorescence contrast confirms the ability of our OPT system to perform neuroanatomical phenotyping as described previously [50].

Vascular network

Vascular abnormalities play an important role in cognitive decline and inflammation in some AD patients. To demonstrate the compatibility of our clearing protocol with a fluorescence labeling of the vasculature, we perfused the animals with an FITC-albumin hydrogel. This labeling method was performed on 4-month-old B6SJL F1 mouse brains (n=2) and the resulting images, acquired using the OPT system with the 470-nm excitation illumination, are shown in Figure 3.4. In this configuration, we can identify a variety of vascular compartments, including the superior sagittal sinus (SSS) and the sigmoid sinus (SS), which are venous sinuses found within the dura mater, the outermost layer surrounding the central nervous system, and located on top of the brain (Figure 3.4(A)). The caudal rhinal vein (CRV), running on the side of the brain in a sagittal manner (Figure 3.4(B)), the anterior cerebral artery (ACA), which partly forms the circle of Willis, ring-shaped system of arteries, situated at the base of the

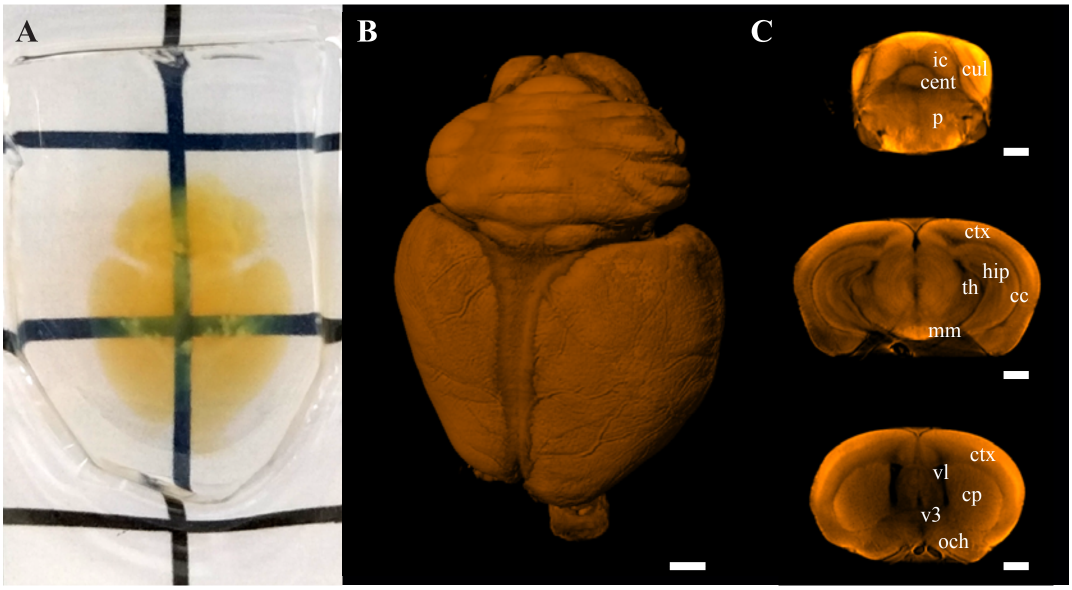

Figure 3.3 – Photograph of a mounted and cleared 8-month-old B6SJL F1 mouse brain (A). 3D rendering of the OPT image obtained from tissue autofluorescence (B, Visualization 1 [available online]). Single coronal sections of the OPT image (C) showing the inner morphology of the intact organ: cc, corpus callosum; cent, central lobule; cp, caudoputamen; ctx, cerebral cortex; cul, culmen; hip, hippocampal region; ic, inferior colliculus; mm, medial mammillary nucleus; och, optic chiasm; p, pons; th, thalamus; v3, third ventricle; vl, lateral ventricle. Grid spacing (in A): 1 cm. Scale bars: 1 mm.

brain (Figure 3.4(C)), and the middle cerebral artery (MCA) traveling from the circle of Willis to the top of the brain. To better appreciate the 3D nature of the blood vessels, we created maximum intensity projections from 20 consecutive OPT sections at different positions of the brain (Figure 3.4(D)). These artificial sections represent half a millimeter of the whole brain sliced coronally and highlight penetrating vessels several millimeters in depth. However, smaller vessels, such as capillaries, have a diameter of typically less than 10 µm and fall beyond our resolution limit. The innermost vessels of the brains are seemingly undetected. This could be due to the depletion of the fluorescence signal propagating through the sample as well as the shadowing from the surface vasculature. Ultimately, the identification of large brain vessels with the hydrogel perfusion extends the phenotyping capacity of OPT and has potential application in the study of aneurysms, strokes, and vascular development [110].

Amyloid deposition

New amyloid imaging agents, based on the chemical structure of histologic dyes, are now making it possible to track amyloid pathology along with disease progression. To show the compatibility of our clearing protocol with fluorescence labeling of amyloid deposits, we injected the animals IP with an amyloid-binding dye called Methoxy-X04. This labeling method was performed on 8-month-old 5xFAD mouse brains (n=3) and the resulting images,

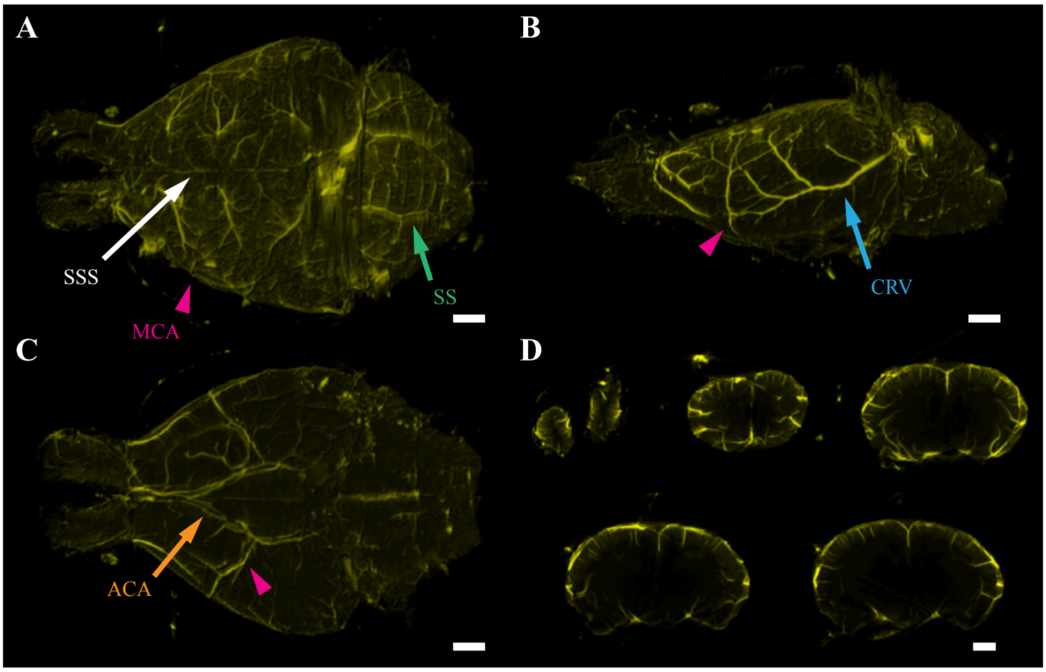

Figure 3.4 – Visualization of the brain vasculature in a 4-month-old B6SJL F1 mouse. The brain was perfused with an FITC-albumin hydrogel and imaged with OPT. 3D rendering from the top (A), side (B), and bottom (C) view (see Visualization 2 [available online]). Maximum intensity projections of 20 coronal sections through the whole brain (D) showing the penetrating venules/arterioles. ACA, anterior cerebral artery; CRV, caudal rhinal vein; MCA, middle cerebral artery; SS, sigmoid sinus; SSS, superior sagittal sinus. Scale bars: 1 mm.

acquired using the OPT system with the 420-nm excitation illumination, are shown in Figure 3.5. Individual sections of the three-dimensional OPT image (Figure 3.5(A)) reveal a mixed contrast between the brain anatomy and amyloid plaques, seen as bright dot agglomerates (denser zones pointed out by the arrows), caused by the overlap of the autofluorescence and the Methoxy-X04 emission spectra. The 3D rendering of the whole brain, presented in Figure 3.5(B), reveals the amyloid distribution in the organ and highlight an important aggregation in the subiculum (Figure 3.5(B) and 3.5(C)). This result adds to the findings of Oakley *et al.* [105], who used histology to localize amyloid deposition, providing deeper insights into the 3D distribution of the amyloid plaques. Interestingly, the pathological phenotype observed in the 5xFAD mice shows differences in the 3D distribution compared to the APPPS1 model used in the work of Jährling *et al.* [43] at a comparable age. This observation further demonstrates the high potential of OPT for fast phenotyping. Small plaques (below 50 μm) are blurred out due to the system's resolution.

Histology comparison

The proposed framework for rapid mouse brain imaging with OPT extends the current 3D capability of traditional histology. For this reason, we performed a qualitative comparison of

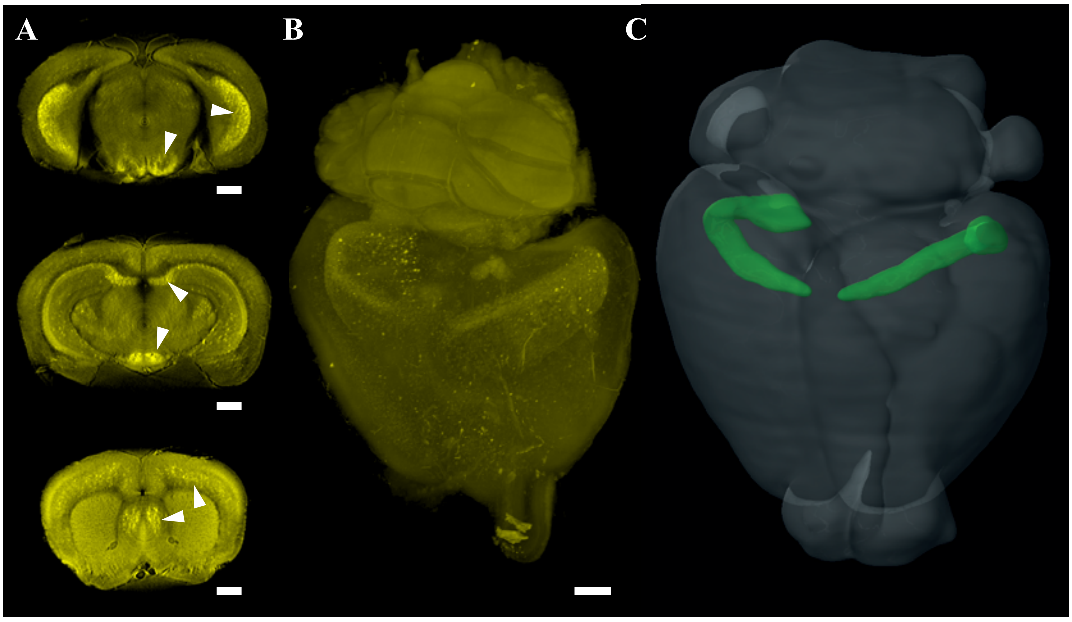

Figure 3.5 – 3D imaging of amyloid deposition in an 8-month-old 5xFAD mouse. Single coronal sections (A) with the arrows pointing to regions with high deposition and three-dimensional rendering of the OPT image (B, Visualization 3 [available online]). A 3D image of the subiculum (green) is shown within a whole mouse brain (C) to compare with the location of amyloid deposition. Image (C) was obtained from the Allen mouse brain atlas [111]. Scale bars: 1 mm.

both techniques by splitting labeled mouse brains into hemispheres. The hemispheres were then processed separately: one was prepared for histology (Figure 3.6(A) and 3.6(D)), and the other one for OPT (Figure 3.6(B)-(C) and 3.6(E)).

First, the result of this comparison for the vasculature in a 9-month-old B6SJL F1 mouse brain is shown in Figure 3.6(A)-(C). The histological slice (Figure 3.6(A), Visualization 4 [available online]) displays details of the microvasculature as well as larger vessels, pointed by pink arrows. However, the acquisition and stitching of the images took almost an hour for a single section. Additionally, stitching artifacts, such as the one pointed by the blue arrow, remain visible in the figure. On the other hand, some of the large vessels (pink arrows) can be identified in the OPT section (Figure 3.6(B)), but the microvasculature is not resolved. Additionally, we used the 3D capability of OPT to produce a maximum intensity projection (Figure 3.6(C)) from 20 consecutive sections (approx. 0.5 mm in thickness), which reveals a range of penetrating vessels otherwise difficult to obtain in histology.

Second, the result of the comparison for the amyloid plaques in a 3-month-old 5xFAD mouse brain is shown in Figure 3.6(D)-(E). The histological slice (Figure 3.6(D), Visualization 5 [available online]) present a high-resolution mixed contrast between tissue autofluorescence and amyloid plaques (regions of accumulation pointed by green arrows). However, the acquisition and stitching took approximately an hour, and the resulting section suffers from microtome artifacts (blue arrows). On the other hand, the regions of plaques accumulation (green arrows) could be retrieved in the OPT section (Figure 3.6(E)) with a lower resolution. Additionally, we observed an opposed contrast in some regions of the brain, such as the corpus callosum (cc), which is bright in the histological section but appears dark in OPT. This might be caused by the chemical clearing.

These results highlight the complementarity of traditional histology and OPT. Mechanical slicing associated with wide-field fluorescence microscopy produces high-resolution images of the features of interest in 2D. However, this method can be cumbersome (particularly the cutting and stitching parts) and is hardly suitable for 3D imaging. On the other hand, OPT produces low-resolution 3D images of the whole organ in about 5 minutes with a user-friendly sample preparation.

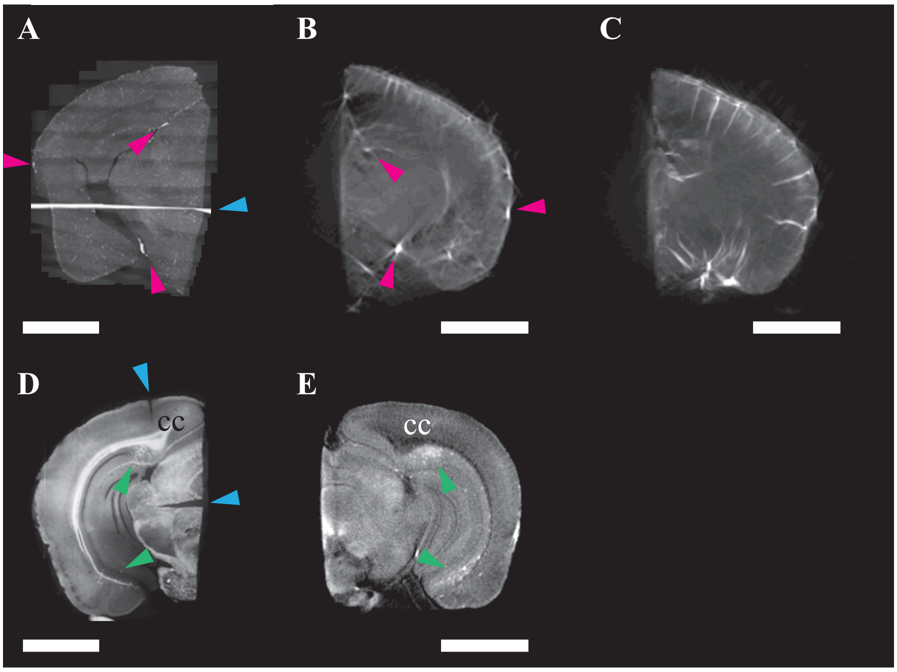

Figure 3.6 – Comparison of histological and OPT slices. 40 µm-coronal section of a 9-month-old B6SJL F1 mouse brain hemisphere labeled for vasculature (A, Visualization 4 [available online]) and corresponding single OPT section (B). A maximum intensity projection (C) taken over 20 consecutive OPT sections, which represents approximately 0.5 mm in thickness, gives a better representation of the penetrating vessels and highlights the 3D advantage of this technique. 40 µm-coronal section of a 3-month-old 5xFAD mouse brain hemisphere labeled for plaques (D, Visualization 5 [available online]) and corresponding single OPT section (E), some regions such as the corpus callosum (cc) show an inverted contrast. Scale bars: 2 mm.

Conclusion

In this manuscript, we present a novel OPT method for whole mouse brain imaging. This method is based on a custom OPT system, designed for mouse brain imaging, and an optimized sample preparation. The OPT system provides an FOV of $26.6 \times 26.6\ \mathrm{mm}^2$ and can image samples as thick as 26 mm typically within less than 5 minutes. It incorporates an epifluorescence arm, which provides a uniform full-field illumination and is easily configurable by switching the excitation LEDs and filters. The sample preparation consists of a simple and rapid solvent-based clearing of the organ (3 changes of clearing solution in 3 days). This can be complemented with fluorescence labeling of the vasculature, through perfusion of a fluorescent hydrogel, or labeling of amyloid deposition in a mouse model of AD, via 2 consecutive injections of an amyloid-binding dye. Based on this method, we imaged B6SJL F1 mouse brains without markers. The results demonstrate the quality of the clearing and reveal details of the organ structure, an essential requirement of neuroanatomical phenotyping [50]. Additionally, by imaging the vasculature of B6SJL F1 mouse brains, we identify major vessels, as well as penetrating arterioles/venules in 3D down to several millimeters in depth. We also imaged 5xFAD mouse brains with labeled amyloid deposition. Individual sections of the OPT image revealed regions of accumulated amyloid plaques. Through 3D rendering, we could identify the subiculum as the region with the densest accumulation, in concordance with the literature [105]. Finally, we performed a qualitative comparison of histological and OPT slices in the different hemispheres of the same brain to illustrate the complementarity of these two techniques.

The rapid acquisition of whole mouse brains with our OPT system is achieved through a long DOF and a low magnification, which currently limit the resolution to ~50 µm. Additionally, the low NA of the system restricts the light collection efficiency. This would be a plausible explanation for why finer structures such as capillaries and small amyloid plaques (<50 µm) were undetectable. Furthermore, the method requires embedding of the sample in agarose for mounting purposes. While the surrounding agarose simplifies the clearing protocol, by creating an interface with the solvents and avoiding the use of increasing concentration solutions, it has not been tested yet with other clearing methods such as CLARITY [112], SeeDB [109], Sca*l*e [113], or 3DISCO [114].

In the future, other clearing methods optimized for OPT might improve the current results obtained with BABB; new amyloid imaging agents with a distinct excitation/emission spectrum will help to discriminate between the tissue autofluorescence and the amyloid plaques. Additionally, our imaging method shows high potential for the use in neuropathology and the study of disease progression, similarly to the work and research in diabetes [48, 49], by imaging the mouse pancreas at different ages. Ultimately, our OPT setup with its large FOV is well suited for the imaging of other organs, such as the liver, lung, and kidney.

Supporting information

The 3D reconstructed OPT datasets used to generate Fig. 3.3-3.5 can be downloaded from our website at https://lob.epfl.ch/files/content/sites/lob/files/shared/downloads/brainOPT.zip/.

Funding

The authors greatly acknowledge the funding from: EU Framework Programme for Research and Innovation (602812, 686271); Commission for Technology and Innovation (CTI) (13964.1, 17537.2); Lundbergs Foundation (2014/2073); Novo Nordisk Foundation (NNF150C0016146); Royal Physiographic Society.

Acknowledgments

The authors would like to thank Amélie C. M.-O. Ducrey and Silas Schlatter for their helpful contributions during their semester projects.

The authors would also like to show their gratitude to the Histology Core Facility (HCF) of EPFL for the slicing and mounting of the brain hemispheres with the microtome.

Disclosures

The authors declare that there are no conflicts of interest related to this article.

3.2 Author contributions

Author contributions are written based on the CRediT taxonomy [115].

David Nguyen proposed the design (**Conceptualization**), built and aligned the instrument (**Methodology**), including control software (**Software**). He participated in brain extractions and performed the rest of the sample preparation (**Methodology**). He also acquired (**Investigation**), processed (**Software**), and rendered (**Visualization**) the OPT images. David wrote the original draft (**Writing – Original Draft Preparation**) and was involved in the **Project Administration**. Finally, he was responsible for **Data Curation**.

Paul James Marchand supervisied the project (**Project Administration** and **Supervision**), participated in the instrument design (**Conceptualization**), helped with the instrument alignment (**Methodolody**), performed part of the brain extractions (**Methodolody**), gave insights to results interpretation (**Investigation**) and reviewed the manuscript (**Writing – review & editing**).

Arielle Louise Planchette performed the rest of the brain extractions (**Methodology**) and reviewed the manuscript (**Writing – review & editing**).

Julia Nilsson helped with the sample preparation (**Methodology**) and reviewed the manuscript (**Writing – review & editing**).

Miguel Sison helped with the instrument alignment (**Methodology**), discussed the instrument design (**Conceptualization**), and reviewed the manuscript (**Writing – review & editing**).

Jérôme Extermann participated in the project planning (**Project Administration** and **Supervision**), and reviewed the manuscript (**Writing – review & editing**).

Antonio Lopez verified the mechanical design, and proofread the blueprints (**Verification**).

Marcin Sylwestrzak programmed the GPU implementation of the filtered back-projection algorithm (**Software**).

Jessica Sordet-Dessimoz proposed a histology protocol for the brain samples (**Methodology**).

Anja Schmidt-Christensen discussed the sample preparation (**Methodology**), and reviewed the manuscript (**Writing – review & editing**).

Dan Holmberg proposed the idea to build an OPT instrument (**Conceptualization**), provided his expertise in the field (**Validation** and **Supervision**), and reviewed the manuscript (**Writing – review & editing**).

Dimitri Van De Ville discussed the design (**Conceptualization**), provided **Supervision**, was involved in **Funding acquisition**, and reviewed the manuscript (**Writing – review & editing**).

Theo Lasser supervised the project (**Supervision**), discussed the design (**Conceptualization**), provided the project planning (**Project administration**) as well as funding (**Funding acquisition**), and reviewed the manuscript (**Writing – review & editing**).

4 OPT optical and tomographic instrument characterization

In the previous chapter (Chapter 3), the implementation of a custom OPT instrument for mouse organ imaging was described. In parallel to the development of this instrument, we contributed to the characterization of OPT instruments in various areas. First, we aimed to standardize the mounting procedure to decrease sample preparation variability, which we achieved by molding agarose in conical tubes. The new mounting procedure facilitates sample preparation and is less prone to image artefacts, due to the agarose block shape in the original procedure. Second, we performed microparticle imaging to understand the instrument's transfer function through its point spread function. This approach to characterize the instrument has rarely been applied in standard OPT, and our results suggest that it is relevant to perform it on every instrument at least once because it can reveal imperfections in the motorized rotation stage. Finally, ever since the introduction of OPT in 2002, the choice of a number of projections for OPT acquisitions has never been discussed. It was originally suggested to use 400 projections (separated by 0.9°) [9]. Later, researchers worked with empirical numbers such as 360 projections (separated by 1°) [97] and 1200 projections (separated by 0.3°) [50], but without any justification on their choice. Although these number of projections lead to good quality OPT images, we decided to challenge their empirical values. The results suggest that the number of projections to be acquired depends on the type of sample to be imaged and its spatial frequency content. Moreover, when evaluated in mouse organs, the number of projections required to compute accurate reconstructions was always higher than the original 400. These contributions are detailed in a research article submitted to the Journal of Biomedical Optics in December 2018. This section is composed of the preprint version of the article, followed by a detailed list of author contributions.

4.1 Practical aspects of optical projection tomography imaging exemplified with whole mouse organs

David Nguyen[1,2,3*], Octave Martin[1], Adrien C. Descloux[1,3], Dimitri Van De Ville[2], Theo Lasser[3], Aleksandra Radenovic[1]

[1] *Laboratory of Nanoscale Biology, School of Engineering, École Polytechnique Fédérale de Lausanne, CH-*1015 *Lausanne, Switzerland*
[2] *Medical Image Processing Lab, School of Engineering, École Polytechnique Fédérale de Lausanne, CH-*1202 *Genève, Switzerland*
[3] *Laboratoire d'Optique Biomédicale, School of Engineering, École Polytechnique Fédérale de Lausanne, CH-*1015 *Lausanne, Switzerland*
[*] *david.nguyen@epfl.ch*

Abstract

Optical projection tomography (OPT) is a mesoscopic imaging tool holding invaluable potential for life sciences, as the understanding of biological processes goes through 3D visualization at the centimeter scale. We address key technical aspects of OPT to improve reconstructions quality. An agarose embedding procedure based on molding in conical tubes is presented, and images of fluorescent microparticles are shown. We also introduce a method to investigate the effects of the number of projections on the reconstruction's quality. All of this showcased in different mouse organs endogenously and with a vasculature staining. We hope that these insights will make OPT more accessible and that they will open the door to new applications of mesoscopic 3D imaging.

Introduction

Mesoscopic imaging is a branch of optical microscopy focusing on large samples, typically with a size ranging from a few millimeters to several centimeters in at least one direction [12]. The principal modalities of mesoscopic imaging include light sheet fluorescence microscopy (LSFM), opto-acoustic (OA) microscopy, and optical projection tomography (OPT) [116]. These methods have critical applications in life sciences and hold an invaluable potential to extend the molecular and cellular knowledge to a higher level of structural organization. LSFM [90] uses a planar illumination shined orthogonally to the detection axis to produce fluorescent optical sections of a specimen and reconstruct 3D volumes. This method has been applied to the visualization of neural [33], and vascular [91, 92] networks in whole mouse brains, as well as the recording of neuronal activity in whole zebrafish brains [38] and the imaging of the fruit fly nervous system [10]. OA microscopy [117] records optical absorption in tissues by measuring pressure changes upon excitation with a light pulse. This method has been applied for the visualization of the whole mouse [29] and zebrafish [118] anatomy. Lastly, OPT [9] takes a series of in-focus images at different angles, called projections, over a complete turn to compute a 3D reconstruction of the specimen with a filtered back-projection algorithm (FBP) [73]. OPT has been used since 2002 for 3D fluorescence imaging of biological specimen. It was originally described as a tool for gene expression studies in mouse embryos [44], but its field of application proliferated.

For instance, whole mouse pancreas imaging with OPT plays a key role in diabetes research [47, 48, 49], providing scientists with a quantitative overview of the disease progression in the entire organ. Similarly, whole mouse brain imaging is performed with OPT for the study of Alzheimer's disease [55]. *In vivo* OPT imaging of zebrafish embryos [119, 100] can also be applied to study the cardiovascular system [46]. Technological advances have closely followed the application growth in OPT. Helical scanning [51] allows acquisition of elongated samples, such as the mouse spine, without compromising the field of view. Normalized born approach [95] has been proposed in fluorescence OPT to account for tissue absorption properties. A point-spread-function based method to reconstruct OPT images increases signal-to-background ratio and resolution [53, 54]. However, these features aim to improve OPT resolution, and few papers have been dedicated to the fundamental aspects of OPT imaging. These include investigations of the importance of correct determination of the center of rotation [82], and correction of image artefacts in OPT [79], although the latter is mostly restricted to simulation cases.

This work aims to consider other fundamental and recurring aspects of OPT acquisition and to present preliminary studies highlighting interesting avenues for the future development of OPT technology.

While standard OPT sample preparation protocols exist [85, 86], they rely on the critical trimming of the sample-enclosing agarose block. As a means to uniformize sample shape and reduce the risk of sample damage and imaging artefacts, we introduce a nearly cut-free specimen embedding procedure in agarose via molding in conical tubes. Then, we rely on imaging microparticles to qualitatively characterize the point spread function (PSF) of our OPT instrument, to better understand imaging and reconstruction artefacts. Images of fluorescent microparticles also illustrate the space-varying nature of the PSF in OPT. The last aspect we study concerns an essential parameter of OPT acquisition, which is the number of projections. It is well known in X-ray computed tomography that the number of projections plays a crucial role in reconstruction accuracy [120], and that reconstruction from an insufficient number of projections leads to heavy image artefacts. We investigate the influence of increasing the number of acquired projections on the resulting reconstruction quality in various samples, namely the mouse brain, lungs, kidney, and fluorescent microparticles. The comparison between specimen reconstructions from a different number of projections is based on correlations. To the best of our knowledge, it is the first time that the effect of the number of projections is investigated in OPT.

In Section 4.1, we review the OPT sample preparation and present our different specimen embedding procedure. We describe the OPT instrument PSF qualitatively through the use of fluorescent microparticles in Section 4.1. Finally, in Section 4.1, we present the results of modulating the number of projections on image reconstruction quality in OPT, followed by concluding remarks in Section 4.1.

Animal ethics statement

Animal procedures were carried out according to Swiss regulations (animal protection ordinance 455.1) under the approval of the veterinary authority of the canton of Vaud (license: VD3058) and all efforts were made to minimize suffering, following the principle of the 3Rs [121].

Sample preparation with a different embedding procedure

Standard protocols for OPT imaging are usually composed of three parts: organ extraction, specimen embedding, and optical clearing [85, 86]. Each of these is briefly reviewed in the following paragraphs, and a different specimen embedding procedure is presented in Subsection 4.1.

Organ extraction

Organ extraction methods differ depending on the experiment's design but can include deep anesthesia and perfusion of the animal to be sacrificed, as well as organ harvesting. Staining is an optional step that can be performed at different points of organ extraction. For example, amyloid plaques in a mouse brain with Alzheimer's disease are stained before sacrifice [55], whereas antibody staining is performed after the organ has been harvested [104]. In this work, we used 4 B6SJL F1 mice, one of 8, two of 23, and the last of 51 weeks of age, which were primarily sacrificed for other experiments but were re-used in our experiments. The mice were deeply anesthetized with pentobarbital and perfused with 2 ml of heparinized PBS, and 10 ml of 10 % formalin (HT501128, Sigma). In the 51-week-old mouse, the vasculature was stained by perfusing the animal with 10 ml of a hydrogel containing FITC-conjugated albumin [92]. After perfusion, we harvested the brain from the 8-, and 23-week-old mice (3 mouse brains). We also harvested the lungs and a kidney from the 51-week-old mouse (2 mouse organs). All organs were postfixed in 40 ml of formalin overnight.

Specimen embedding

OPT imaging often requires the sample to be glued on a motorized rotation stage [85]. Direct contact of the sample with glue impairs imaging and is avoided by embedding the specimen in agarose gel. Embedding starts by filling a container, such as a Petri dish, with warm 1.5 % (wt/v) agarose gel. Then, the specimen is transferred to the container's center and is maintained in this position until the gel solidifies. Finally and critically, a block containing the sample is carved from the gel according to the following principles. Firstly, the amount of agarose around the sample is minimized to reduce its effect on light penetration. Secondly, the block is "shaved" to remove acute angles, which could cause light scattering. Lastly, approximately 1 cm of agarose is left on the side of the sample which will be glued to the rotation stage. Trimming an agarose block can be a problematic operation as it is brittle. The block's translucence results in refraction effects that make it difficult to precisely cut around the sample. Moreover, edge quality depends on several factors, including block temperature, and blade quality and handling. Ultimately, trimming is a contributor to variability in the resulting images.

We propose an embedding protocol that significantly reduces related artefacts and associated variability. Conical-tube-based molds are used to produce agarose cylinders, virtually free from light-scattering edges (see Figure 4.1). The required materials include: microtome blades, a pair of inoculation loops, ice in a container and a 15 ml conical tube (Figure 4.1a). The conical tube is cut with a saw along the 10 ml graduation line, and the conical tip is discarded. Deburring and rinsing the mold with acetone helps to prevent bubbles when pouring the agarose inside. The mold is placed on ice and filled with approximately 4 ml of warm 1.5 % (wt/v) agarose in Milli-Q water (0.22 μm-filtered). The specimen can then be sunk in the agarose gel and maintained at the mold's center with inoculation loops (Figure 4.1b). When the agarose begins to solidify, the inoculation loops are removed. Since only 5-10 ml of agarose gel are used, the solidification occurs within minutes and is faster than in a whole Petri. The mold is allowed to cool until complete gel solidification at 4° C (Figure 4.1c), and is subsequently immersed into hot water (approximately 90° C) for 10-30 seconds (Figure 4.1d) to facilitate unmolding (Figure 4.1e). Finally, the cylinder can be trimmed at its extremities, while remembering to keep at least 1 cm of agarose on one side of the sample. The critical step of this protocol is to maintain the sample at the center of the mold before agarose gel solidification. Different mold sizes can be obtained with other conical tube volumes, but 15 ml tubes were found to be the most suitable for mouse brains, kidneys, and lungs.

OPT images acquired with the custom embedding protocol (Figure 4.2a) are comparable to the ones from standard embedding protocols (Figure 4.2b and c). In Figure 4.2c, the agarose block interface is emphasized in the image (red arrowheads) due to poor cut quality performed by an inexperienced user. However, even if trimming is performed cautiously by an experienced user, it does not prevent the occurrence of cutting artefacts (red arrowheads in Figure 4.2b). These images also reveal the presence of a cavity (blue arrowheads) in the agarose block, which corresponds to the original specimen morphology. After optical clearing with BABB (described below), specimens were found to have shrunk, as already documented previously [109]. The custom embedding protocol preserves image quality while the risk of damaging the sample and introducing cutting artefacts is reduced.

Optical clearing

Optical clearing is an essential part of OPT sample preparation for opaque specimens, such as mouse organs. Its purpose is to enhance light penetration by making these specimen

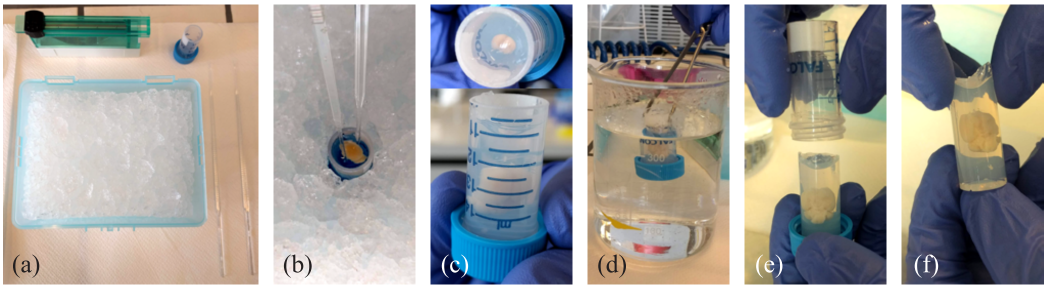

Figure 4.1 – Agarose mounting in custom molds made from 15 ml conical tubes. (a) Start with ice in a container, a sharp blade, two inoculation loops, and the part with the cap of a 15 ml conical tube which was cut along the 10 ml graduation line. (b) Pour warm 1.5 % agarose solution in the mold on the ice, add the specimen, and, with the inoculation loops, maintain it at the center of the mold until it starts solidifying. (c) Once the specimen stops moving, remove the loops quickly and wait for complete solidification. (d) Sink the mold into hot water for 10-30 seconds. (e) Unmold by gently opening the cap. (f) If necessary, trim the uneven circular surfaces of the cylinder, while always keeping at least 1 cm of agarose on the end of the cylinder to be mounted on the instrument.

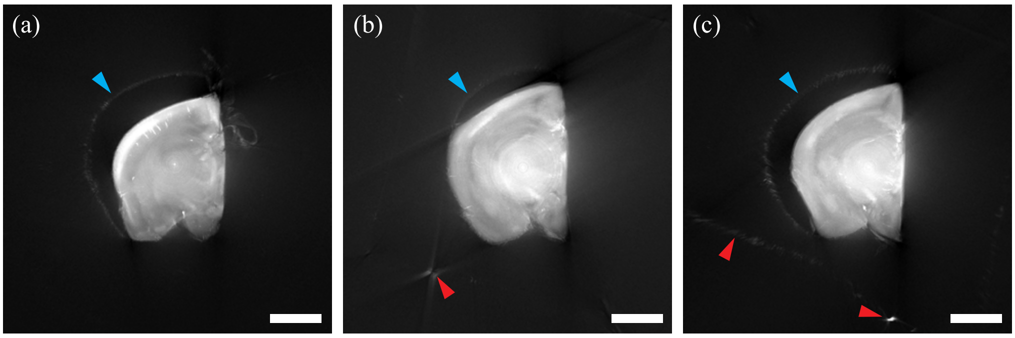

Figure 4.2 – Comparison between the different embedding protocols on OPT images of mouse brain hemispheres. Each image is a maximum intensity projection through 100 slices, which corresponds to 1.3 mm of tissue thickness. (a) Trimming-free procedure with agarose molding in conical tubes. (b) Standard trimming procedure performed by an experienced user. (c) Standard trimming procedure performed by an inexperienced user. The images are saturated to better visualize mounting artefacts. Blue arrowheads: agarose cavity due to specimen shrinkage after optical clearing. Red arrowheads: artefacts from agarose trimming. Scale bar: 2 mm.

transparent. In this work, we use the clearing protocol from our previous work [55]. Briefly, samples are dehydrated in methanol for a day and incubated for two days in a 1:2 solution of benzyl alcohol and benzyl benzoate (BABB) before imaging.

Microparticles imaging for OPT characterization

The characterization of an imaging instrument is important to understanding its inherent limitations and minimizing their effects through methods adaptation. Among the properties of an imaging system, the point spread function (PSF) is probably the most relevant [122]. The PSF describes the response of the instrument to an ideal point source. In practice, ideal point sources are taken as known objects which are much smaller than the actual PSF of the system. For fluorescence microscopy, including OPT, fluorescent microparticles are the tool of choice [123]. The size of the particles can be determined by estimating the resolution of the system, which is a measure of the PSF size. We carried out this approach using a custom OPT instrument [55] built for large-scale specimen imaging. The field of view is 26.6 × 26.6 mm^2 with a diffraction-limited resolution of approximately 28 µm. The resolution was improved by using a camera chip without binning (2048 × 2048 px^2), at the expense of image processing time and storage expenditure. The other instrument's features are a numerical aperture of 0.01, a magnification of 0.5X, and a working distance of 300 mm. For this characterization, we opted for 5 µm fluorescent FITC-labeled microparticles (75908-5ML-F, Sigma). These particles are more than five times smaller than the system's resolution, which satisfies the sampling theorem [124], and are sufficiently bright to be imaged by the OPT instrument. The preparation of the microparticles for OPT imaging uses the molding procedure described in Section 4.1, where the beads are the specimen. Approximately 0.01 µl of particles are mixed to 10 ml of agarose solution before molding. The acquisition is performed without clearing steps, which would otherwise bleach the fluorescent signal from these microparticles. The difference in refractive index between BABB and water in the agarose gel causes light scattering and aberrations (although negligible with a numerical aperture of 0.01) at the interface of the agarose cylinder. In this particular case, image acquisition and reconstruction can still be performed normally. Additionally, BABB and water do not mix. Over time, this makes the agarose block opaque. Consequently, the microparticle samples are used once and discarded after imaging.

The results of imaging samples with fluorescent microparticles using our OPT instrument are presented in Figure 4.3. A total of 99 slices are reconstructed, and a depth color-coded maximum intensity projection image is generated (Figure 4.3a-c). The instrument shows a space-varying PSF with a circular shape close to the center of rotation, symbolized with a red cross (Figure 4.3b). When moving away from the center of rotation, the PSF takes the shape of an arrowhead pointing toward the exterior of the sample. Furthermore, the size of the PSF increases with the distance to the center of rotation. Due to the translucent nature of the agarose gel without clearing, each microparticle is only visible on approximately half of the projections. This phenomenon is illustrated in the sinogram (0.9 mm in depth) of Figure 4.3d, where some microparticle traces (blue arrowheads) do not span the 360°.

In summary, the PSF size of our OPT instrument increases with the distance from the center of rotation and transforms from a circular to a growing-arrowhead shape pointing towards the agarose cylinder surface. The varying shape of the PSF currently hinders the computation

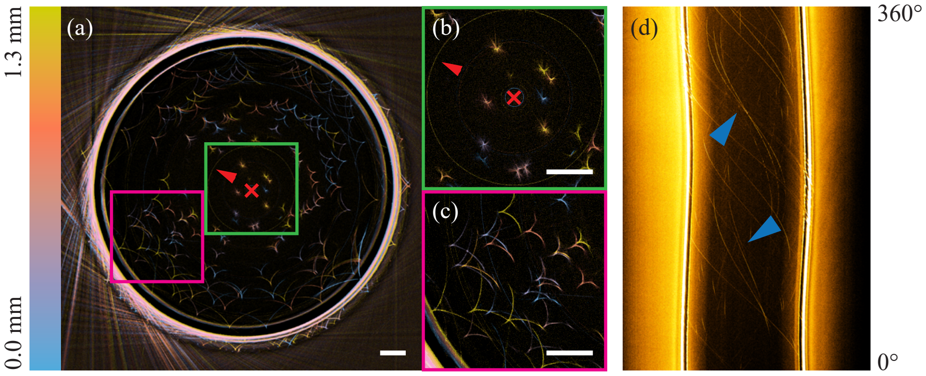

Figure 4.3 – Fluorescent microparticles imaging with the OPT instrument. (a) Depth color-coded maximum intensity projection of a section from the agarose cylinder mixed with microparticles. Red arrowheads indicate ring artefacts, which can be used to identify the center of rotation (red crosses). Color-coded tiles correspond to zoom-in views in (b) and (c). (d) Sinogram of the microparticle sample at 0.9 mm depth. Blue arrowheads points to incomplete single particle traces. Scale bar: 1 mm.

of the system's resolution and depth of field. Additionally, this PSF differs from what was observed by Van Der Horst *et al.* [125] and Trull *et al.* [53, 54]. Both reported a radius-dependent tangential blurring of their PSF from the center of rotation, although with a different instrument. However, the nature of the changes in the PSF shape of our system has led us to think that these artefacts are related to something else than optics. Indeed, the large increase in the PSF size cannot be explained with regards to the large depth of field of the instrument (15.4 mm). Rather, we believe it is caused by the mechanical rotation of the motorized stage. There could be an eccentricity in the rotation, and there might also be an inaccuracy to generate constant angular increments. In the future, we want to characterize the rotation stage motion, measure its positioning precision, and eventually try to correct for systematic errors we find to improve reconstruction accuracy. However, in the following organ images acquired with the OPT instrument, the effect of the PSF degradation is difficult to judge and the image quality is already sufficient to see details of the vascular network.

Assessment of image quality with projection number

OPT imaging requires projections acquired at different angles, over a complete turn, and with a depth of field covering at least half of the sample thickness to be used by the filtered back-projection (FBP) algorithm [73] and compute a 3D reconstruction of the sample. In practice, the number of acquired projections is a parameter chosen by the experimentalist, bearing in mind that it is directly related to the image reconstruction quality. Indeed, decades of research in X-ray computed tomography, where FBP was initially applied, have shown that reconstructions using an insufficient number of projections contain image artefacts [120]. Although a greater number of projections imply a higher reconstruction fidelity, several factors limit the number of angles that can be considered in OPT. More projections imply a prolonged exposure to the excitation light, which eventually leads to photobleaching of the fluorescence signal. It also means greater computational memory consumption and longer image processing times, which is a growing issue for experiments involving numerous specimens. Additionally, the precision of the motorized rotation stage imposes a minimal angular displacement, although new motors have a resolution far below 0.1° thus enabling acquisitions with more than 3600 projections. Currently, most OPT acquisition protocols rely on 400 projections that are processed by the reconstruction algorithm, as was suggested in the original OPT paper [9]. We believe that the appropriateness of this number depends on the sample type to be imaged and should be evaluated on a case-by-case basis, as discussed hereafter.

We propose a correlation-based approach to assess how image quality improves with the number of projection and suggest a method for estimating the appropriate trade-off. Our method requires a specific acquisition protocol, described as follows. Firstly, a large number of projections is acquired for the sample of interest, and the resulting high-quality reconstruction is defined as ground truth. In the present case, 3000 projections were used. Secondly, a series of reconstructions with a different total of projections (ranging from 100 to 3000 by steps of 100 projections in this case) is computed. The smaller stacks of projections are obtained by linear interpolation of the ground truth stack. Thirdly, each reconstruction is correlated with the ground truth and the Pearson correlation coefficient $\rho_{X,Y}$ (PCC), defined as

$$\rho_{X,Y} = \frac{\mathrm{cov(X,Y)}}{\sigma_X \sigma_Y}, \tag{4.1}$$

where X is the reconstruction from fewer projections, Y is the ground truth, cov is the covariance, and σ_X and σ_Y are the corresponding variances, is computed. Finally, a plot of the PCC against the number of projections can be generated. This acquisition protocol was tested on three samples: a mouse brain, lung, and kidney. The subsequent 3D reconstructions of these samples are shown in Figure 4.4. Additionally, the protocol was also tested on the microparticles sample presented in Section 4.1. To reduce the processing time, only a selected subvolume of the sample underwent the correlation procedure. For mouse organs, 49 slices were processed, and for microparticles, 99 slices were processed. Ground truth acquisition times were approximately 9, 12.5, 7.5, and 25 minutes for the brain, lung, kidney, and microparticles, respectively. During all acquisitions, signal decay due to photobleaching did not exceed 10 %.

The PCC curves of each sample (mouse brain, lung, kidney, and microparticles) are shown in Figure 4.5. All curves present a similar behavior. They are almost monotonically increasing and asymptotically approach 1. However, their growth pattern is specific to the sample utilized. For example, the mouse brain curve systemically has higher values than the other curves for a given number of projections. Before we can hypothesize on the reasons behind this behavior,

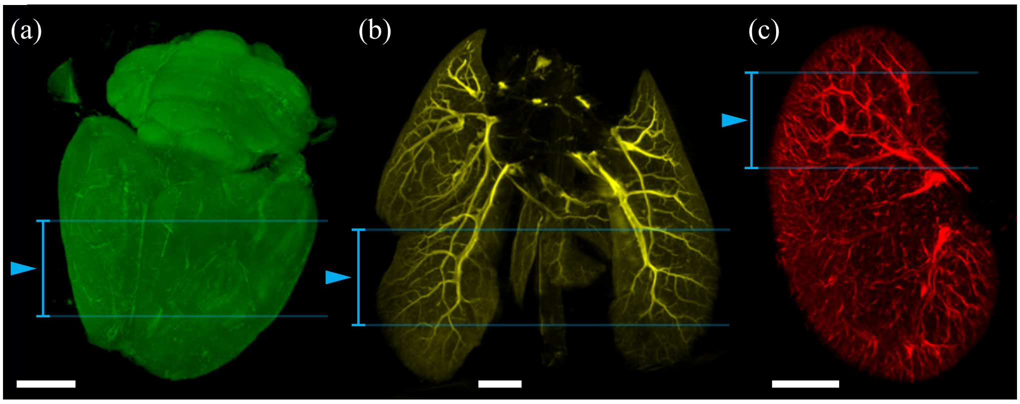

Figure 4.4 – Maximum intensity projections through ground truth reconstruction (from 3000 projections) acquired with the OPT instrument. The specimens are: (a) a 8-week-old mouse brain morphology, and the vasculature from (b) a 51-week-old mouse lung and (c) a 51-week-old mouse kidney. Blue arrows indicate the subvolumes used for correlations. Scale bar: 2 mm.

we should notice that all nervous tissues have similar levels of autofluorescence and they create a rather homogeneous distribution of intensities across the organ (see Figure 4.6). The resulting image is therefore mainly composed of low spatial frequencies, which are better captured than high spatial frequencies with fewer projections. The vasculature curves (lungs and kidney samples) confirm this hypothesis. The vascular network is made of intricate blood vessels, which result in high spatial frequency image features in the 3D reconstruction (see Figure 4.6). Therefore, the lungs and kidney require more projections to reach a PCC value that compares to that of the brain for a given number of projections. Consequently, the small differences (at least below 1500 projections, as discussed below) observed between the kidney and lungs curves could indicate a difference in the tissue-specific type of vascularization.

Additionally, the microparticles curve requires an even higher number of projections to reach a given PCC value (at least below 1500 projections), which is also in favor of the hypothesis that the curve growth depends on the spatial frequency content of the image. Microparticles indeed reflect the PSF of the OPT instrument, which is by definition the highest detectable spatial frequency. Finally, around 1500 projections, the PCC curves of the kidney vasculature, lungs vasculature, and microparticles intersect. Correlation values above this number of projections do not have a particular trend. We think this can be attributed to noise in the *close to ground truth* reconstruction regime. Therefore it is probably not useful to acquire more than 1500 projections with the current instrument for these types of samples. The autocorrelation of the ground truth (PCC=1) has been omitted on the plot of Figure 4.5 because it introduced a jump in the PCC curves at 3000 projections. This jump is another indication that with more than 1500 projections, differences in the reconstruction are mostly attributed to noise and the correlation level saturates before reaching 1.

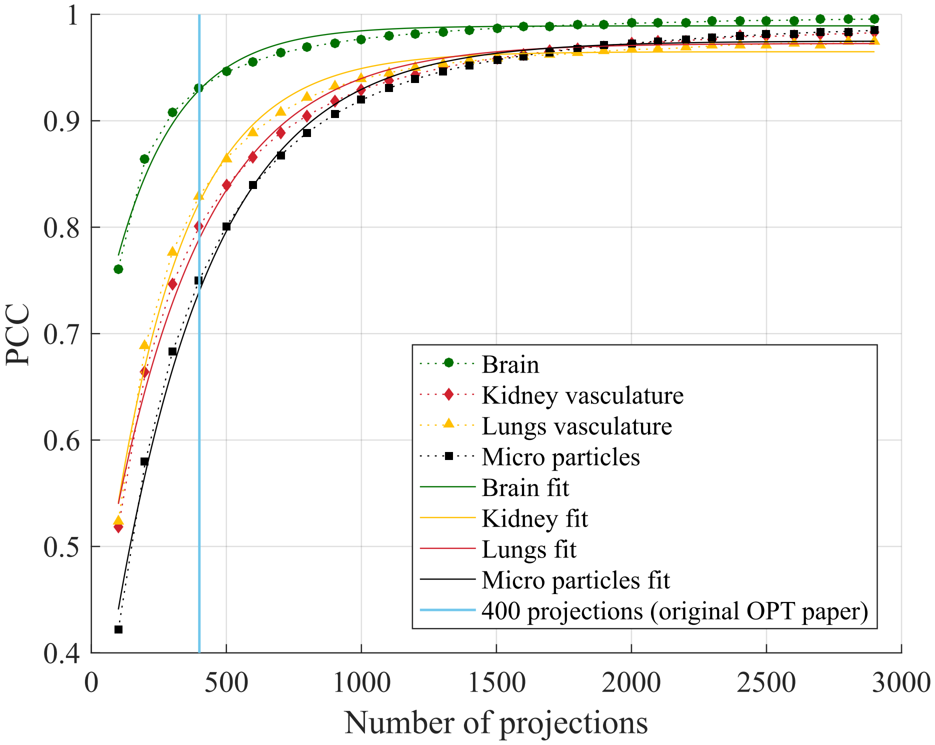

Figure 4.5 – Plot of the PCC and corresponding fit against the number of projections for different samples studied in this work. The curves are monotonically increasing and approach 1 in an asymptotic manner. The amount of projections required to reach a given PCC value depends on the sample type. Samples with higher spatial frequency content require more projections, up to a saturation level of approximately 1500 projections. The blue line indicates 400 projections, as suggested in the original OPT paper.

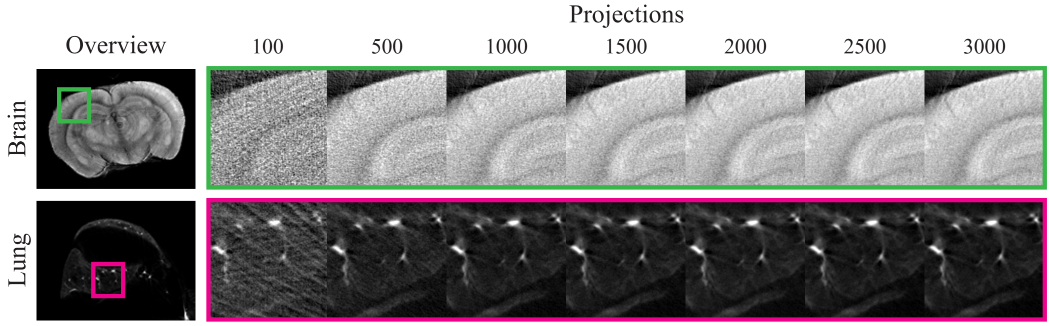

Figure 4.6 – Selected slices from the 3D reconstructions of the mouse brain and right part of the lungs vasculature. Color-coded tiles indicate zoom-in view reconstructed with an increasing number of projections (from 100 to 3000).

As hypothesized, PCC curves could be an indication of the spatial frequency content in an image. They can assist in deciding the appropriate number of projections to acquire for OPT imaging of a particular sample. It is worthwhile also looking at reconstructions with a different number of projections in a single slice of each sample. Such an analysis is shown in Figure 4.6 for the mouse brain and part of the vasculature of the mouse lung. From these images, it is clear that reconstructions based on 100 projections are inaccurate and heavily corrupted by reconstruction artefacts. At 500 projections, streak artefacts remain present in the lung image, and the brain image has a granular texture. At 1000 projections both images have considerably fewer artefacts. From 1500 projections onward, image improvements become marginal, which agrees with our hypothesis that, after 1500 projections, PCC values reflect more noise fluctuations than improvements on reconstruction quality. Since little signal decay (<10 %) was observed during the acquisition of ground truth images, we do not expect this to be a problem at 1500 projections. Additionally, signal decay in that order of magnitude can be corrected [79]. Regarding acquisition time, the 1500 projections of mouse specimens presented in this work took 5 minutes, and the memory expenditure for that amount of projections is approximately 12 Gbytes (2048 × 2048 × 1500 px^3 in 16 bits). The approach described in this section aims at helping OPT users choosing the number of projections considering their samples and instrument. In our case, we found that mouse brain anatomy, as well as lungs and kidney vasculature, are accurately reconstructed with 1500 projections without prohibitively compromising the acquisition duration or memory consumption. Moreover, the computation of a PCC curve from microparticle images can provide information on the number of projections at the limit of the instrument resolution, which can serve as an upper bound to the number of projections. Since microparticle images are likely to be acquired infrequently in OPT instruments, we suggest to select a large number of projections for their reconstructions as the improvement in image quality is not fully understood yet. In our case, we would still acquire 3000 projections for our microparticles samples.

Finally, we fitted the PCC curves with an exponential function

$$\rho_{X,Y}(n) = a - b\exp^{-cn}, \tag{4.2}$$

where n is the number of projections and a, b, and c are the fit coefficients. These fits are plotted in Figure 4.5 and the coefficients are summarized in Table 4.1 with the resulting R-square value. They can be used to infer on the PCC value for any given number of projections.

Conclusion

In this paper, we discussed several aspects of OPT imaging: sample preparation, with a focus on specimen embedding, instrument characterization with fluorescent microparticles and

Table 4.1 – Fit coefficient and R-square value for the four different PCC curves in Figure 4.5.

Sample	a	b	c	R-square
Brain	0.9892	0.3303	0.004256	0.9823
Lungs	0.9649	0.6108	0.003656	0.9918
Kidney	0.9727	0.576	0.00286	0.9922
Micro particles	0.975	0.7023	0.002736	0.9958

the influence of the number of projections on the subsequent reconstruction with the FBP algorithm. Each aspect provides a starting point to be further investigated. Microparticle imaging can serve to understand the instrument behavior and specifications, such as the point spread function and resolution. A better knowledge of these features can help in designing deconvolution methods for OPT as suggested by Van Der Horst *et al.* [125]. However, as microparticle imaging depends on the instrument properties, such as numerical aperture, motorized rotation stage precision, and detector, it needs to be systematically conducted on different setups. Similarly, the analysis of the number of projections could be used to find an adaptive criterion for the automatic determination of this parameter, given a sample. Ultimately, in discussing these aspects, we aim to help standardize the OPT technology and make it more accessible to life scientists.

Disclosures

The authors declare that there are no conflicts of interest related to this article.

Funding

The authors gratefully acknowledge the funding from the EU Framework Programme for Research and Innovation (grant agreement 686271).

Acknowledgments

The authors would like to thank Dr. Virginie Uhlmann for the helpful discussions and comprehensive review of the manuscript.

4.2 Author contributions

Author contributions are written based on the CRediT taxonomy [115].

David Nguyen proposed the idea of a practical OPT paper with technical details of the specimen acquisition protocol (**Conceptualization**). He participated in the organ extraction and performed the sample preparation (**Methodology**, **Investigation**). David rendered the figures of the paper (**Visualization**), wrote the original draft (**Writing – Original Draft Preparation**), and is responsible for **Data Curation**.

Octave Martin participated in the organ extraction, sample preparation, and performed the OPT acquisitions of the different specimens, including the microparticles which he prepared himself (**Methodology**, **Investigation**). He modified the OPT software for the acquisition and processing of a large number of projections (**Software**). Octave also reviewed the manuscript (**Writing – review & editing**).

Adrien Charles Descloux proposed and discussed the correlation method to compare reconstructions from different total number of projections (**Conceptualization**). Adrien was involved in discussions about the microparticles imaging and the OPT PSF shape (**Investigation**). He also reviewed the manuscript (**Writing – review & editing**).

Dimitri Van De Ville provided **Supervision**, was involved in **Funding acquisition**, and reviewed the manuscript (**Writing – review & editing**).

Theo Lasser supervised the project (**Supervision**), provided funding (**Funding acquisition**), and reviewed the manuscript (**Writing – review & editing**).

Aleksandra Radenovic provided **Supervision**, was involved in **Funding acquisition**, and reviewed the manuscript (**Writing – review & editing**).

5 OPT applied to Alzheimer's disease

In the last two chapters (Chapter 3 and 4), we have demonstrated the performance of OPT in the context of mouse whole-organ imaging, with an emphasis on the brain. An essential part of neurodegenerative diseases research is done on mouse brains, and its role in elucidating the etiology of diseases such as Alzheimer's disease (AD) is critical. In the OPT images of amyloid plaques in whole mouse brains, we have seen a mixed contrast between the tissue autofluorescence and the plaque-specific signal. This mixed contrast makes it difficult to separate the plaques from their surroundings. A means of isolating amyloid plaques for quantification would be extremely valuable to observe the disease progression and assess treatments efficacy. In this chapter, we demonstrate for the first time segmentation and quantification of amyloid plaques in whole mouse brains of AD mice with a supervised learning algorithm based on random forests [126]. The performance of the method was evaluated in a preliminary cross-sectional study, and the results are presented in a research article submitted to Biomedical Optics Express in December 2018. This section is composed of the preprint version of the article, followed by a detailed list of author contributions.

5.1 Supervised learning to quantify amyloidosis in whole brains of an Alzheimer's disease mouse model acquired with optical projection tomography

David Nguyen[1,2,3*], Virginie Uhlmann[4,5], Arielle L. Planchette[1,3], Paul J. Marchand[3], Dimitri Van De Ville[2,6], Theo Lasser[3], Aleksandra Radenovic[1]

[1] *Laboratory of Nanoscale Biology, School of Engineering, École Polytechnique Fédérale de Lausanne, CH-*1015 *Lausanne, Switzerland*
[2] *Biomedical Imaging Group, School of Engineering, École Polytechnique Fédérale de Lausanne, CH-*1015 *Lausanne, Switzerland*
[3] *Medical Image Processing Lab, School of Engineering, École Polytechnique Fédérale de Lausanne, CH-*1202 *Genève, Switzerland*
[4] *Laboratoire d'Optique Biomédicale, School of Engineering, École Polytechnique Fédérale de Lausanne, CH-*1015 *Lausanne, Switzerland*
[5] *European Bioinformatics Institute, EMBL-EBI, Cambridge, United Kingdom*
[6] *Department of Radiology and Medical Informatics, University of Geneva, CH-*1202 *Genève, Switzerland*
[*] *david.nguyen@epfl.ch*

Abstract

Alzheimer's disease (AD) is characterized by amyloidosis of brain tissues. This phenomenon is studied with genetically-modified mouse models. We propose a method to quantify amyloidosis in whole 5xFAD mouse brains, a model of AD. We use optical projection tomography (OPT) and a random forest voxel classifier to segment and measure amyloid plaques. We validate our method in a preliminary cross-sectional study, where we measure 6136 ± 1637, 8477 ± 3438, and 17267 ± 4241 plaques (AVG ± SD) at 11, 17, and 31 weeks. Overall, this method can be used in the evaluation of new treatments against AD.

Introduction

Amyloidosis in brain tissues is associated with several neurodegenerative diseases, including Parkinson's and Alzheimer's disease (AD). In AD, toxic extracellular aggregates of a truncated and thus misfolded amyloid precursor protein form deposits known as amyloid plaques [127, 128]. These plaques have a spherical shape, and their size varies between approximately ten and one hundred micrometers. The neuropathological nature of the plaques is hypothesized to play a central role in the etiology of AD and is at the core of Alzheimer's disease research [66]. The mechanisms of plaque formation and their consequences remain elusive and are commonly studied in genetically modified rodent models, such as the 5xFAD mouse model [105]. Such models are designed to reproduce the age-dependent amyloid deposition observed in humans [129].

The standard technique used to visualize and quantify amyloid plaques is histopathology wherein sections of brain tissue are sliced, mounted on glass cover slides, stained, and imaged with either a widefield or a fluorescence microscope. Histopathology is an invaluable diagnostic tool but has some limitations. Strict sample preparation protocols and a well-practiced and meticulous expertise are required. In addition, reproducibility across samples is challenging to obtain, and artefacts related to sample preparation are nearly unavoidable. Furthermore, three-dimensional renderings of whole brains remain prohibitively time-consuming. As a consequence, this technique only allows observing the development of amyloid plaques in local, arbitrarily chosen areas of the brain, making an objective comparison between specimen difficult. Other less invasive techniques exist to image amyloid plaque growth *in vivo*, such as two-photon microscopy [130], optical coherence microscopy [68], and photoacoustic microscopy [131]. All three techniques can resolve individual plaques consistently while preserving brain integrity through the use of cranial windows. They can cover several square millimeters of tissue over hundreds of micrometers in depth, but fail at imaging over the whole brain. Differential phase contrast tomography [132] and contrast-enhanced magnetic resonance microscopy [133] can produce images of amyloidosis in whole intact rodent brains with a resolution of a few tens of micrometers. However, they require expensive instruments with specific sample preparation protocols and are therefore not routinely used. Ultramicroscopy [134] is another technique for visualizing amyloidosis in whole-excised mouse brains [43, 135]. It is a mesoscopic adaptation of light sheet microscopy, where a sheet of light illuminates the sample orthogonal to the detection path, thus producing optically sectioned fluorescence images of the organ with minimal photobleaching. Similarly, optical projection tomography (OPT) [9] can perform whole mouse brain neuroanatomical phenotyping [50] and amyloidosis imaging [55] by acquiring fluorescence projections of the organ at different angles over a complete turn. Although ultramicroscopy and OPT are complementary techniques, ultramicroscopy often offers a better resolution, while OPT is generally easier to implement and more robust to misalignment.

To quantify amyloidosis progression from image data, the standard protocol is to process specimen with an amyloid plaques-specific staining such that the plaques stand out from other tissue elements. A segmentation mask is then obtained by identifying which image elements correspond to amyloid plaques. From there, the number of plaques and volume they occupy can be estimated. When imaging the whole brain at once, a significant challenge is the staining of the intact organ. For amyloid plaques, Methoxy-X04 [136] is one of the only probes that can be used due to its ability to penetrate the blood-brain barrier. However, the excitation of Methoxy-X04 (in the near-UV/blue) also generates a strong signal from tissue autofluorescence. Therefore, quantitative image-based analysis of amyloidosis relying on voxel intensity thresholding, as typically used in histopathology data, cannot be performed. Amyloid plaques are indeed indistinguishable from tissue autofluorescence based on intensity, henceforth requiring a more complex image analysis approach. In the work of Jährling *et al.* [43], plaques could be isolated in ultramicroscopy images by applying intensity thresholding since small sub-volumes called cubes were considered instead of the whole brain volume. Quantitative analysis was then run through six of these cubes per sample. Statistical analyses are performed on the sub-volumes but they do not reflect the brain-wide plaque distribution.

In this paper, we propose a supervised learning pipeline relying on random forest voxel classifiers to segment and quantify amyloid plaques in whole 5xFAD mouse brains of different ages acquired with OPT.

Learning-based automated classification for AD has gained a strong interest in recent years. The disease is indeed currently diagnosed based on clinical examination, and classification of AD samples, preferably at an early stage of the pathology, holds a strong potential for adding validity to the diagnosis. Signal-based classification already allowed identifying markers to aid in Alzheimer's disease diagnostic from diffusion tensor imaging scans [137], EEG signals [138], intracellular recordings [139], or multiple sources including various 3D imaging modalities [140].

Regarding tissue imaging data, BioVision [141] was proposed as a supervised training approach for image-based identification of histopathological objects. This approach, relying on a pixel-based Bayesian classifier, has been used for the quantification of amyloid plaques in histology images [142]. A similar approach was followed by Vandenberghe *et al.* [143] on the same type of data, showing that random forest classifiers exhibited better performance. The work of Li *et al.* [144] also illustrates the good performance of pixel-based decision tree algorithms, this time for the pixel-based classification of MRI image data. An essential aspect of these previous works is that the classification algorithm operates on pixels in 2D slices. Another way to approach the problem of identifying brain components from images is atlas-based segmentation [145, 143]. In this setting, a labeled model (the atlas) of the 3D organ is deformed to fit the 3D image volume at once. From the resulting boundaries of each labeled regions, statistics can be derived at the local level.

As no atlas labels are available for mouse brain in OPT data, the approach we propose considers 3D voxels in image volumes without an underlying atlas. It is, to the best of our knowledge, the first attempt to introduce a learning-based method for amyloid plaques detection in OPT image data and, more generally, to quantify amyloid plaques relying on a pipeline incorporating information from all three dimensions in an atlas-free setting.

Our manuscript is structured as follows. Firstly, we briefly describe the sample preparation and imaging setup, which we introduced in our previous work [55]. Secondly, we present the supervised learning pipeline for segmentation and quantification of amyloidosis. Supervised learning provides an efficient way to learn, from a set of manually annotated examples, how image features such as *e.g.*, grayscale intensity and textures [146], should be combined to segment objects of interest in images [147]. In particular, pixel- and voxel-based random forest classifiers have proved their efficiency for bioimage segmentation tasks [148, 149]. We choose to rely on that specific type of algorithms for two main reasons: first, random forests are well-suited for classification tasks with few training data; and second, they can be used through the ilastik [150] interface. ilastik is an open-source image analysis software, which provides a user-friendly GUI for training and reusing trained classification workflows for prediction. In that way, we aim at making our image analysis pipeline easily reusable with or without additional training. Thirdly, we showcase the results of the segmentation and quantification in 5xFAD mouse brains of different ages. Finally, we discuss the impact and limitations of our study and give some recommendations based on our preliminary results.

Materials and methods

Sample preparation

Experiment animals, 5xFAD mice [105] on a B6SJL F1 background, were generated by crossing 5xFAD transgenic females on a C57BL/6J background (34848-JAX, MMRRC) with wild type SJL/J males (000686, The Jackson Laboratory) in the local animal facility (housing conditions are described below). The disease phenotype is observed to be more robust on this hybrid background [151]. The 5xFAD mouse model is commercially-available and widely-used in AD research. The mice develop a severe amyloid pathology starting around 1.5 months with high levels of accumulation in the subiculum [105]. Animal procedures were carried out according to Swiss regulations [152] (animal protection ordinance 455.1) under the approval of the veterinary authority of the canton of Vaud (license: VD3058), and all efforts were made to minimize suffering, following the principle of the 3Rs [121]. Experiment animals were housed in ventilated cages (maximum 5 animals per cage) under a 12h light/dark cycle (lights on at 7 a.m.) and controlled atmosphere (23 °C and 50% relative humidity) with *ad libitum* access to food and water. Two 5xFAD transgenic females on a C57BL/6J background were housed with one wild type SJL/J male in the breeding cages under the same conditions as experiment animals, but the extreme aggression of SJL/J males [153] hampered the breeding capacity. Indeed, 5 out of 12 females in the 6 breeding cages (that we shared with other experimentalists) were found dead with lethal lesions from fights with the males. To refine our breeding protocol, we decided to move the males in individual cages when the females were pregnant. However, this measure was not sufficient to prevent casualties in the breeding cages, and it reduced the number of experiment animals that could be generated, more details can be found in the discussion section.

Brains were processed as described previously [55]. In summary, the mice were injected with Methoxy-X04 (Tocris) [136], a fluorescent marker that targets amyloid plaques. Then, they were deeply anesthetized using an overdose of pentobarbital and perfused with a 10% formalin solution. The brains were extracted and post-fixed in formalin overnight. Each organ was mounted in a 1.5% agarose gel and cleared using BABB before imaging. An illustration of these steps is shown in Fig. 5.1A.

Ten experiment animals could be retrieved from the breedings and were divided into three age-groups after amyloidosis onset (Tg/0): a young one at 11 weeks old ($n = 3$), a middle-aged one at 17 weeks old ($n = 4$), and an old one at 31 weeks old ($n = 3$). A fourth control group

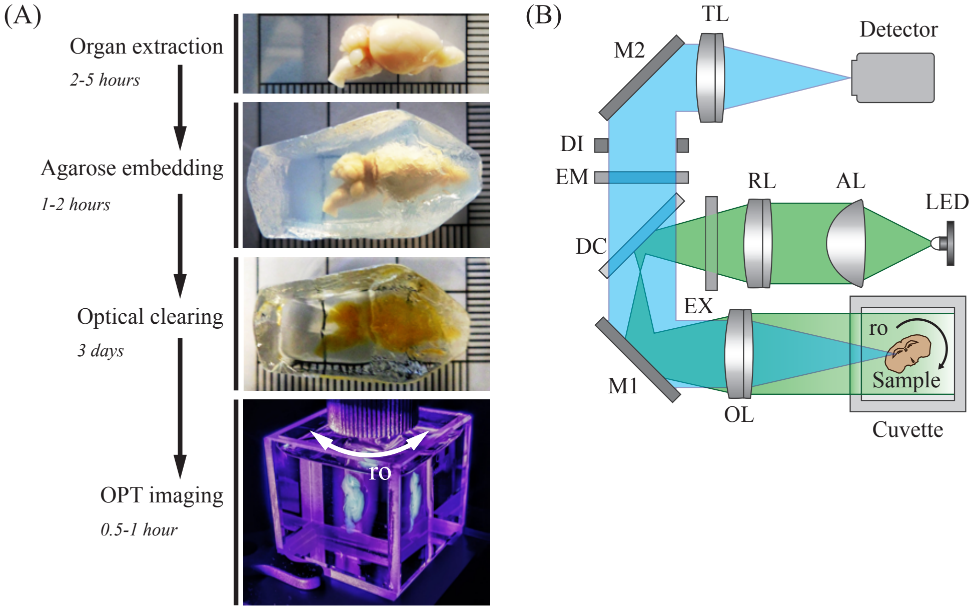

Figure 5.1 – **Sample preparation and experimental setup.** (A) Photographs of a mouse brain through the different steps of the preparation protocol. (B) Scheme of the optical projection tomography setup. AL, aspheric lens; RL, relay lens; EX, excitation filter; DC, dichroic mirror; M1/2, mirrors; OL, objective lens; EM, emission filter; DI, diaphragm; TL, tube lens; ro, rotation.

($n = 2$) was formed with B6SJL F1 mice (+/+) that did not have the transgenes. The control group followed the same sample preparation as the experiment groups, including Methoxy-X04 injection. All samples and their corresponding group are recapitulated in Table 5.1. As indicated in the third column, some samples are composed of only one hemisphere of the brain, as some specimen had to be shared with other experimentalists.

Optical projection tomography

Whole brain imaging was performed with a custom OPT setup [55] shown in Fig. 5.1B. The instrument is similar to an epifluorescence microscope. It uses a 420-nm LED light source and a 300-mm achromat objective lens (OL) to produce fluorescence projections of the sample with a 0.5X magnification. The fluorescent light is filtered using a custom filter set from Chroma composed of a dichroic (DC) mirror (AT455dc), an excitation (EX) filter (AT420/40x), and an emission (EM) filter (AT465lp). A diaphragm (DI) in the rear focal plane of the OL enlarges the depth of field to guarantee a sharp focus through the front half of the sample. Projections are acquired over 360 degrees by steps of 0.3 or 0.9 degrees in approximately five minutes. The three-dimensional reconstruction of the sample is achieved by applying a filtered back-projection [73] to these projections. To do so, we perform the same procedure as described previously in [55], and refer the reader to the latter work for more details. In

Table 5.1 – **List of samples processed.** The * indicates samples, which were partially annotated for the training of the random forest classifiers. The † indicates samples, which were used to generate Fig. 5.4. Tg/0, transgenic animals; +/+, wild type animals.

Id	Age [weeks]	Structure	Genotype	Image size [px^3]	Group
0[†]	11	Whole	Tg/0	407*x*344*x*514	Young
1[*]	11	Hemisphere	Tg/0	283*x*288*x*517	
2	11	Hemisphere	Tg/0	268*x*321*x*569	
3	17	Whole	Tg/0	300*x*274*x*590	Middle-aged
4	17	Whole	Tg/0	317*x*243*x*650	
5[†]	17	Hemisphere	Tg/0	446*x*307*x*602	
6	17	Hemisphere	Tg/0	442*x*320*x*577	
7[*,†]	31	Whole	Tg/0	420*x*357*x*603	Old
8	31	Whole	Tg/0	411*x*389*x*597	
9	31	Whole	Tg/0	427*x*384*x*615	
10	7	Whole	+/+	352*x*340*x*512	Control
11[†]	31	Whole	+/+	432*x*334*x*576	

this configuration, the OPT setup has an isotropic resolution of approximately 50 µm over the whole organ. The current resolution does not allow to measure small plaques (10-50 µm). However, the intense brightness of the plaques still makes them detectable for counting.

Image segmentation and quantification

The overall image-based segmentation and quantification process from reconstructed projections is depicted in Figure 5.2. Once 3D image volumes are reconstructed with a filtered back-projection algorithm, images are normalized using Fiji [107] and its contrast enhancement tool before segmentation to accommodate for differences in dynamic range stemming from variations in, *e.g.*, image acquisition time. During normalization, 0.1% of the total amount of voxels (stack histogram) is allowed to be saturated in the image to account for outliers. This normalization step is crucial for the quality of the subsequent segmentation of amyloid plaques. As voxel intensity is part of the feature set considered by our proposed supervised learning approach, all image volumes must be brought to a comparable dynamic range, both in the training and prediction phases.

We segment plaques from background and brain image elements using a supervised learning approach. To do so, we designed a 3D voxel classification workflow in the open-source image analysis software ilastik [150]. The image analysis pipeline consists of two steps. First, training is performed from manual annotations of a few voxels in a small selection of image data. Then, the trained supervised learning algorithm predicts the type of the remaining unannotated voxels in these image data, as well as the type of each voxel for the ones left aside during training. In our case, random forests [126] are used as learning algorithm. The working

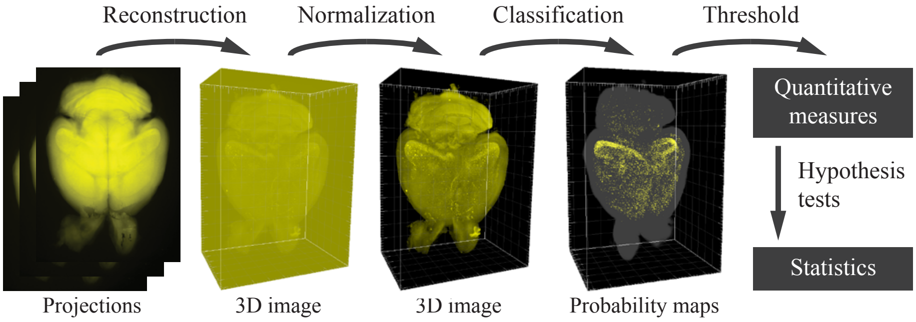

Figure 5.2 – **Processing pipeline.** From OPT acquisition, the projections are used to reconstruct a 3D image with a filtered back-projection algorithm. After a normalization step, a random forest classifier identifies voxels corresponding to plaques in the image volume. Quantitative measurements can be extracted from the segmentation mask, and statistical analyses can be conducted.

principle of this approach is as follows. A set of numerical measurements, called features, is computed for each object to be classified (in our case, the voxels). These measurements aim at describing the object in terms of, *e.g.*, color, shape, neighborhood and serve to distinguish objects belonging to different classes (in our case, plaques versus everything else). The specific nature of the features we rely on is described hereafter.

In the training phase, given (a) a collection of objects, (b) their feature values, and (c) their known class labels, several decision trees are built by randomly picking features and searching for proper decision boundaries to separate between classes. Starting from the root, each intermediate node in a decision tree corresponds to a specific feature, while leaves correspond to class labels. In the prediction phase, given an object and its collection of computed features, each tree is explored to predict the class as follows: the value of the feature corresponding to the root node is examined, and dictates which branch to follow. This process is repeated at each intermediate node until a leaf is reached, which predicts the class of the object. The final class probability estimates are obtained as the percentage of trees predicting the object to belong to each considered class. The overall classification procedure with random forests is illustrated in Fig. 5.3.

The choice of a specific supervised learning algorithm among the vast variety of those available is generally dictated by the constraints that are inherent to the considered problem. In our case, following the principles of the 3Rs, we want our approach to be able to train based on a small number of samples. Moreover, we aim at maximizing the reusability of our pipeline, which implies limiting handcrafted steps and relying on well-established processing environments. These considerations guided our choice for random forests to segment plaques. Random forests indeed provide an excellent trade-off between generalization capability and ability to learn from few training examples [154]. This last point specifically makes them preferred over the currently popular convolutional neural networks, which require training datasets of significantly larger size than the ones considered in this work. In addition, random forests are available through the ilastik GUI, which maximizes user-friendliness during the training phase and ease of use when predicting on new data.

In the training phase, manual annotations were provided for each of the three classes, here corresponding to background, brain, and plaques. Our underlying assumption motivating this setting is that, although plaque signal cannot easily be separated from the autofluorescence signal from brain tissues using a simple intensity-based threshold, it does stand out when considering a combination of texture, intensity and shape measurements. The random forest classifier, therefore, acts as an adaptive way to learn a complex threshold combining these different features to isolate plaques from the rest of the image volume content. The specific voxel features we rely on were computed through the 3D volumes. They can be grouped in three categories: color-based (*i.e.*, voxel intensity values), edge-based (*i.e.*, various edge detectors such as gradient filter, difference of Gaussians, and Laplacian of Gaussians), and texture-based (*e.g.*, eigenvalues of structure tensor, Hessian matrix). All features were computed at various image scales; that is, on the original image volume as well as on the image volume processed by various levels of Gaussian smoothing.

When relying on learning-based approaches, the selection of training elements, which are used as ground truth, is of major importance as it influences the generalization capability and overall performance or the algorithm. We selected samples 1 and 7 (see Table 5.1) for training. These two image volumes, one corresponding to a young and one to an old specimen, were chosen to avoid age-induced batch effects [155]. A few manually labeled voxels were distributed through the whole volume along the X, Y and Z planes to minimize training bias and reduce the risk of overfitting. Once trained, the pipeline was used to predict plaques in all remaining dataset. To assess the false positive rate of the random forest classifier trained in this way, we also ran the pipeline on brain image volumes of negative control specimen to report the amount of erroneously predicted plaques. Results are provided in Table 5.2 and testify the specificity of the method.

We then reused the same background and brain voxel labels but removed the plaque class to train a 2-class random forest voxel classifier and retrieve a whole brain segmentation mask. This second step allows us to compute an estimate of total brain volume, which is used to extract the ratio of plaque volume to the whole brain.

Due to data size (see Table 5.1 for details), all considered image volumes were first converted from .tif stacks to .h5, processed with ilastik, and converted back from .h5 to .tif for visualization purpose.

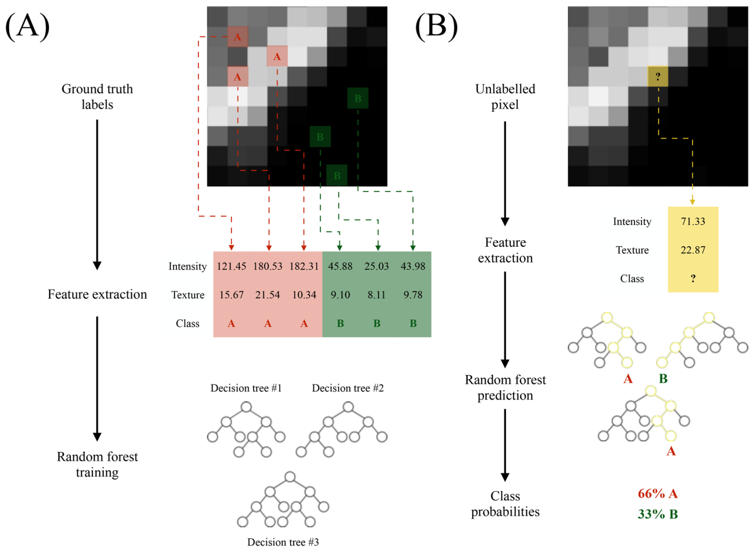

Figure 5.3 – **Classification procedure with random forests.** For the sake of simplicity, 2D pixels and a 2-class problem are depicted. (A) Training phase. A few voxels from each classes (here **A**, the object, and **B**, the background) are manually labeled as ground truth. A collection of measurements, referred to as features, are extracted to characterize these voxels. Here, only two (intensity and texture-based features) are shown. A forest of decision trees is then constructed. Each stage of a decision tree is built by randomly picking a feature and choosing a boundary value that best separates each class according to this measurement. Here, three trees are shown. (B) Classification, or prediction, phase. For each unlabeled voxel, the same set of features as in training phase are extracted. These measurements are then fed to the random forest trees, which provide class prediction. The final probability is retrieved as the percentage of trees predicting each class.

Results

Imaging of amyloid pathology progression

Selected three-dimensional brain images from the three groups of mice are shown in Fig. 5.4A-C. As reported previously [55], the emission signal of Methoxy-X04 is deeply mixed with tissue autofluorescence. Therefore, both the amyloid plaques and brain anatomy can be visualized in a single OPT acquisition. Amyloid plaques can be identified from the strong fluorescent signal they emit as well as from their characteristic small spherical shape. As expected, strong age-dependent amyloidosis is observed in the subiculum, indicated by the white arrows. These images already give us a qualitative feeling for the progression of the amyloid pathology, which worsens with age. However, as previously mentioned, thresholding based solely on voxel intensity as often performed on histopathology data is inefficient for quantitative analysis. The cerebellum, indicated by the blue arrows, indeed exhibits similar voxel intensity levels as plaques, possibly caused by different autofluorescence contrast mechanisms. Likewise, the cortical barrel fields (white arrowheads), which are dense anatomical features of the mouse brain, reach high levels of autofluorescence intensity. Ultimately, perfusion artefacts, such as blood-containing vessels (blue arrowheads), also corrupt the outcome of intensity threshold-based segmentation due to the strong autofluoresence of hemoglobin. Therefore, correct isolation of amyloid plaques from the whole brain requires to rely on a combination of several visual aspects such as their texture, shape, and intensity. A brain image from the control group is shown in Fig. 5.4D. While there is a strong signal from nervous tissues, there is an absence of amyloid plaques.

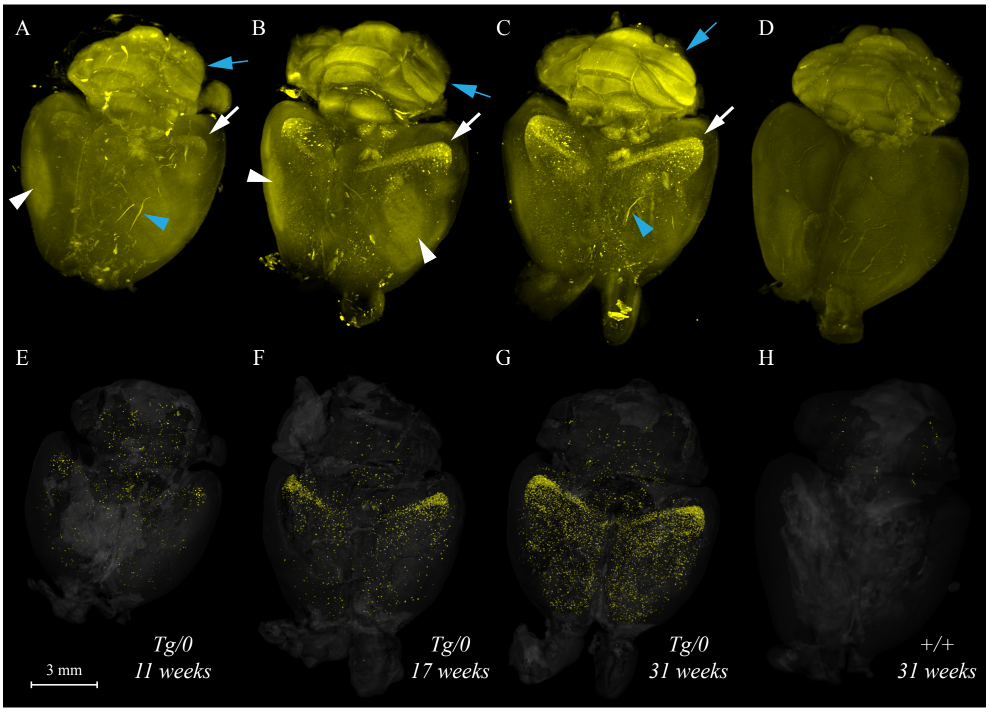

Figure 5.4 – **Imaging of amyloid pathology progression.** (A-C) Renderings of OPT images from the three age-groups: young, middle-aged, and old, respectively. Blue arrows, cerebellum; White arrows, amyloid plaques in the subiculum; Blue arrowheads, blood vessels; White arrowheads, cortical barrel fields. (D) Rendering from the control group. (E-H) Corresponding renderings after random forest classification and thresholding. The amyloid plaques, in yellow (thresholded at 0.5), are overlaid with the brain anatomy, in grey (thresholded at 0.7), whose transparency is reduced for visualization purposes.

Quantification of the amyloid plaques

The outcome of the voxel classification workflow described above provides an efficient way to segment amyloid plaques based on a mixture of their visual features. For each voxel in an OPT image volume of a diseased brain, the 3-class random forest classifier returns a probability value (0-1), yielding a 3D probability map image. The value of each voxel in the probability map image corresponds to the likelihood that the corresponding voxel in the original image belongs to an amyloid plaque. A segmentation mask isolating amyloid plaques is thus obtained by thresholding the 3D probability map at 0.5. This threshold can be directly interpreted as retaining only voxels with a higher-than-50-percent chance of belonging to a plaque. We found it to be sufficiently sensitive for plaque detection against the strong background while maintaining a certain level of specificity, which is discussed at the end of this section. The same procedure can be carried out to segment brain anatomy relying on the probability map output of the 2-class random forest classifier and a threshold of 0.7. The sensitivity to brain tissues is indeed observed to be higher due to a consistency in the autofluorescence signal, allowing us to increase the threshold value to gain more specificity. Segmentation results of the selected brain images from the three age-groups are shown in Fig. 5.4E-H. The transparency of the brain anatomy channel was reduced to enhance the visibility of amyloid plaques. As expected, we observe an increase in the number of plaques with age.

Moreover, the classifier seems to have captured the different features that make amyloid plaques apparent in OPT images. For example, the cerebellum is properly excluded as it does not appear to show amyloid deposition, which is in agreement with known results [105]. Despite its strong fluorescence intensity, it does not meet the other visual criteria to be associated with the amyloid plaque class. The same observations hold for the cortical barrel fields and perfusion artefacts.

After segmentation, we perform a quantitative analysis of the amyloid plaques in the brain by computing the ratio of plaque volume to the total organ volume. This measure is referred to as plaque load and is expressed in percentage. Additionally, the total plaque count provides another quantitative measure of amyloidosis. Regions of dense deposition, such as the subiculum, exhibits the formation of clusters of amyloid plaques in OPT images due to the resolution of the instrument and the normalization step. To refine our estimate of plaque count, we measured the average size of a single plaque and divided the total area of all larger plaque clusters by this value in each sample. Since small plaques have a size comparable to the instrument resolution, we might overestimate the plaque load.

Additionally, as mentioned previously and reported in Table 5.1, some samples of our study are single brain hemispheres. To allow for a fair comparison of the total number of plaques with full brain samples, we reported twice their measured plaque count. This choice is motivated by current observations of brain amyloidosis, which suggests a symmetry of the pathology between brain hemispheres [156]. To further validate this procedure, the 3D image of a whole 31-week-old brain (sample 7 in Table 5.1) was digitally split and the number of plaques was counted in each hemisphere. A total amount of 8418 and 7467 plaques in the left and right hemisphere were obtained respectively, which corresponds to a ratio of 0.53 and 0.47 when divided by the total number of plaques. We thus believe that assuming that the plaque count in a single hemisphere roughly corresponds to half of the total plaque count in the whole brain is a reasonable hypothesis. The results of the quantitative analysis of all samples are summarized in Table 5.2.

Providing results from alternative methods for a reasonable comparison to our approach appears to be challenging. Existing solutions for the automated image-based assessment of amyloid plaques are indeed designed for imaging modalities of entirely different nature (*e.g.*, histopathology, MRI) and, most importantly, trained at a pixel (and not voxel) level. Considering the choice of the algorithm, random forests through ilastik pragmatically appears to be the most efficient solution to maximize user-friendliness in re-training and prediction mode, while ensuring good performance based on a small training set. We are not aware of a convolutional neural network or support vector machine implementation that provides these two features at once.

Unfortunately, no gold standards are available for the labeling of amyloid plaques in 3D OPT image volumes. Although this prevents a rigorous evaluation of the performance, we relied on expert opinion to assess the validity of the segmentation results from a qualitative point of view. They were considered to be accurate from a purely visual perspective.

Since our method has been designed to be easily reusable, all results provided in this paper can be directly reproduced by importing the image analysis pipeline in ilastik, which holds all the necessary information regarding algorithmic parameters, and running it on the raw data (the image analysis pipeline and raw data are available at the Open Science Framework). Annotations provided for training can as well be visualized and the algorithm re-trained from user-provided brush strokes on images through ilastik's GUI.

Table 5.2 – **Quantitative measurements of amyloid plaque quantity in all samples.** The * indicates samples which were partially annotated for the training of the random forest classifiers. The † indicates samples, which were used to generate Fig. 5.4. The mean and standard deviation (SD) is included for each measure and group, which are compared in this study. The control group serves as quality control.

Id	Plaque load [%]		Total number of plaques		Group
$0^\dagger$	0.05	Mean: 0.11 SD: 0.07	4595	Mean: 6136 SD: 1637	Young
1^*	0.09		5958		
2	0.19		7854		
3	0.42	Mean: 0.25 SD: 0.14	12642	Mean: 8477 SD: 3438	Middle-aged
4	0.28		9784		
$5^\dagger$	0.12		4898		
6	0.16		6582		
$7^{*,\dagger}$	0.27	Mean: 0.42 SD: 0.15	13602	Mean: 17267 SD: 4241	Old
8	0.56		21913		
9	0.43		16287		
10	0.001	Mean: 0.002 SD: 0.001	114	Mean: 143 SD: 41	Control
$11^\dagger$	0.003		172		

Ultimately, we performed a statistical analysis of our results, illustrated with boxplots in Fig. 5.5. For the plaque load, there is no statistically significant difference between groups as determined by one-way ANOVA ($F(2,7) = 4.733, p = .05$). However, we still performed a post-

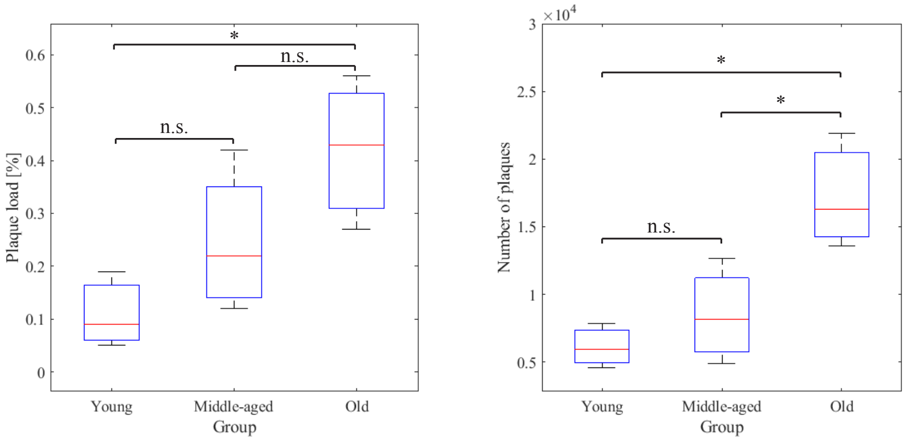

Figure 5.5 – **Representation of the amyloidosis statistical analysis** Boxplots of the quantitative measures of amyloid progression for each group of mice. *, $p < .05$ (Tuckey's test); n.s., not statistically significant.

hoc Tuckey comparison since $p = \alpha = .05$, and we found a statistically significant difference between the young and old group ($p < .05$) (with a 5% chance of it being a false positive). Moreover, a statistically significant difference in total plaque number is observed by one-way ANOVA ($F(2,7) = 9.609, p = .01$). Tuckey's test showed that the old group differs significantly ($p < .05$) from the middle-aged and the young group.

As a quality control, we performed the quantitative analysis on negative controls (Table 5.1). Both the plaque load and plaque count show a reasonably low amount of false positives (Table 5.2), demonstrating the specificity of our analysis.

Discussion

The segmentation of amyloid plaques from whole images of 5xFAD mice brains acquired with OPT shows promising results, as seen in Fig. 5.4E-H. However, limited statistically significant differences are drawn from the group analysis. We believe that this restricted statistical significance, observed in spite of the visually encouraging segmentation outcome obtained with our method, can be attributed to three different factors: the plaque load, number of plaques and number of samples. We now describe in more details how these three aspects affected results in our experimental setting, and propose solutions to minimize their adverse effect in further experimental designs.

Firstly, plaque load is a standard measure of amyloidosis in sections with high plaque density from histopathology data. In our experimental design, sample calculation is based on the findings of Bolmont *et al.* [68], who observed a difference of approximately 1.6 percent in the plaque load between 2 and 4 months of age, using a different mouse model. However, when calculated for the whole brain of 5xFAD mice, plaque load hardly reached 0.5 percent, with differences of 0.1 – 0.2 percent between groups. Therefore, our design is not appropriate to observe such small differences: there is not enough plaque load difference between the age groups we consider when observing the whole brain at once, as opposed to studying a small, specific local section of it. Moreover, comparison of sections in OPT images is hard to achieve due to the difficulty of reliably finding matching sections in the image volumes. Larger groups should thus be considered to observe a statistically significant difference in amyloid plaque load.

Secondly, only limited information about the total number of plaques can be found in the literature. Jährling *et al.* [43] observe a difference of several thousands of plaques between young (10 weeks old) and old (28-34 weeks old) animals. Although these measurements come from a different mouse model of amyloidosis and the total plaque count does not represent a whole brain, they were the most sensible known results for our work and thus served as a basis for our experimental design. Our results suggest that their plaque number estimate was a reasonable starting hypothesis, but that the variability in total plaque count was underestimated. The inter-specimen plaque number variance observed in small cubes is indeed drastically lower than in the entire brain volume. The young (11 weeks old) and middle-aged (17 weeks old) groups seem to be too close in terms of age to be able to observe a statistically significant difference. Our quantification method might not be sensitive enough to capture changes in amyloidosis under 6 weeks of age difference, as there is not enough disease progression in this period to detect a statistically significant difference in levels of amyloidosis. For that reason, we recommend having at least 8 weeks (2 months) of age difference between groups.

Thirdly, when using 5xFAD mice on a B6SJL F1 background, the extreme aggressivity of the SJL/J males in the breeding cages must be considered in the experimental design as casualties are more likely to happen, thus reducing the number of generated specimens. Having witnessed this, we suggest using the congenic 5xFAD strain, on a C57BL/6J background instead. Animals should then be generated by back-crossing females 5xFAD (34848-JAX, MMRRC) with C57BL/6J males (000664, The Jackson Laboratory). We nevertheless believe that the results of our quantitative analysis can be used as a preliminary study. Based on our findings, in order to observe a statistically significant difference of 0.15 percent with a standard deviation of 0.15 percent in the plaque load relying on a one-tailed t-test, 16 animals are required in each age-group ($\alpha = .05$ and power = .85). Concerning the experiment duration, in our experience, 8-12 animals can be sacrificed per day, and the remaining sample preparation takes 4 days (count 1 day to embed the samples in agarose and 10 – 20 minutes per following day to change clearing solutions) plus 1 day of imaging.

In summary, it is noteworthy to take into consideration that quantifying the plaque load in whole mouse brains is inherently subject to more variability compared to other techniques, which focus on smaller regions of interest. Therefore, a more substantial amount of samples is necessary and care must be taken in the experimental design to take into account the variability factors mentioned above. However, our technique, which considers the organ in its entirety, offers a wealth of information for AD research. When looking at individual images, our approach allows to isolate amyloid plaques from the rest of the brain adequately. The plaque patterns are also observed to be similar to what has been previously observed [105]. Plaque load might be overestimated due to the instrument resolution, causing smaller bright plaques to appear with a size of approximately 50 µm. To our knowledge, it is the first time that the plaque load and the total number of plaques are measured in the whole brain of 5xFAD mice.

Our approach, being atlas-free, does not provide information about the locality of the plaques. As a trade-off, it results in a computationally lighter segmentation approach. Incorporating labels to perform atlas-based segmentation is a natural future avenue to pursue. Such additional structure knowledge could, in fact, be combined with our method by including atlas-based information as features to be considered by the random forests.

Conclusion

In this paper, we propose an image-based analysis pipeline for the quantification of amyloidosis. The pipeline is applied to whole brain images of 5xFAD mice, a mouse model of Alzheimer's disease. Image volumes are acquired with an optical projection tomography instrument, and amyloid plaques are segmented relying on a random forest voxel classifier. The plaque load and the total number of plaques are then consistently measured in the whole organ. The pipeline has been tested on 3D OPT images of brains of mice at different ages to illustrate the age-dependent disease progression. This preliminary study shows a statistically significant increase in the number of plaques in old animals (31 weeks old) compared to young and middle-aged ones (11 weeks old and 17 weeks old, respectively). Although the other group differences are not statistically significant, we believe the study should be repeated with more animals to draw more complete conclusions with regards to the disease progression. While there isn't a strict statistically significant difference in the plaque load ($p = \alpha$), a Tuckey post-hoc analysis revealed that the old group differs significantly from the young one. Isolation of plaques from the strong background autofluorescence signal is observed to be successful, and tests on negative controls show a negligible false positive rate. We provide the image volumes and manual annotations used for training, as well as the pre-trained ilastik workflows for download and further use by the community at the Open Science Framework.

In the future, we would like to take advantage of the tissue autofluorescence to segment regions of interest in the brain, such as the subiculum, which is the region where most of the deposition occurs in 5xFAD mice and estimate a local plaque load. Additionally, the pipeline could be reused for data acquired with other mesoscopic imaging modalities, such as ultramicroscopy, and in different rodent models of amyloidosis. Ultimately, we would like to use light sheet microscopy to establish a gold standard for amyloid plaques in the whole brain and compare it with the performance of our OPT classification method.

Data availability

OPT reconstructed data sets and ilastik pipelines are available at the Open Science Framework with a README document on how to use them.

Funding

D.N., AL.P., PJ.M., D.VDV., T.L., and A.R. were supported by the EU Framework Programme for Research and Innovation (Grant agreement 686271). V.U. was supported partly by the Swiss National Science Foundation (Grant 200020-162343), and partly by EMBL-EBI core fundings.

Acknowledgments

The authors would like to thank Dr. Arno Bouwens for the helpful discussions and suggestions for amyloid plaques segmentation.

Disclosures

The authors declare that there are no conflicts of interest related to this article.

5.2 Author contributions

Author contributions are written based on the CRediT taxonomy [115].

David Nguyen generated and maintained the 5xFAD mouse colony with the help of the EPFL animal facility (**Methodology**, **Project Administration**), and carried out the experiment design (**Conceptualization**). He participated in the brain extractions and performed the rest of the sample preparation (**Methodology**). He also acquired the OPT images, annotated the training sets (**Investigation**), performed the segmentation and quantification (**Software**), and rendered (**Visualization**) the 3D volumes and bar plots. David Nguyen co-wrote the original draft (**Writing – Original Draft Preparation**), and is responsible for **Data Curation**.

Virginie Uhlmann proposed the random forest classification approach to segment amyloid plaques (**Conceptualization**, **Ressources**), provided her expertise to annotate, interpret, and evaluate the pertinence of the data sets (**Validation**, **Supervision**). She also co-wrote the original draft (**Writing – Original Draft Preparation**), reviewed the manuscript (**Writing – review & editing**), and participated in **Data Curation**.

Arielle Louise Planchette participated in the brain extractions (**Methodology**, **Investigation**), was involved in the interpretation and evaluation of the results from the plaque classification (**Validation**), and reviewed the manuscript (**Writing – review & editing**).

Paul James Marchand participated in the brain extractions (**Methodology**, **Investigation**), discussed the experiment design (**Conceptualization**), and reviewed the manuscript (**Writing – review & editing**).

Dimitri Van De Ville discussed the experiment design (**Conceptualization**), provided **Supervision**, was involved in **Funding acquisition**, and reviewed the manuscript (**Writing – review & editing**).

Theo Lasser supervised the project (**Supervision**), provided funding (**Funding acquisition**), and reviewed the manuscript (**Writing – review & editing**).

Aleksandra Radenovic discussed the experiment design (**Conceptualization**), provided **Supervision**, was involved in **Funding acquisition**, and reviewed the manuscript (**Writing – review & editing**).

6 OPT towards cell imaging

In optical microscopy, there is a fundamental limitation given by the detector size and its pixel number. Common scientific CMOS cameras have a square 1.3 × 1.3 cm^2 detector with 2048 × 2048 px^2 (the physical pixel size is 6.5 × 6.5 μm^2). Imaging of a whole mouse organ can require up to 2 × 2 cm^2 in the case of the liver [157]. Therefore, a field of view (FOV) of 2.6 × 2.6 cm^2 can be realized with such detectors using a 0.5X magnification, as featured in the OPT instrument considered in this thesis. However, the image pixel size becomes 13 × 13 μm^2, and the maximum attainable resolution in a single image is given by twice this size (following Shannon sampling theorem [124]), *i.e.*, 26 × 26 μm^2. There are then two approaches to improve the resolution down to micrometer level. Both allow cell imaging but require the acquisition of more images.

The first approach consists of acquiring a mosaic of smaller images with higher magnification and stitch them together in a post-processing step. It is often the chosen solution in light sheet microscopy [158]. However, in standard OPT, this approach provides a limited improvement on projection resolution due to the depth of field (DOF) requirements, stated as follows. Whatever the size of the image on the camera, the DOF is at least half the specimen thickness in standard OPT (Section 2.2). Therefore, images at high magnification will have the same resolution as lower magnification ones. There has been an attempt to perform OPT in a region of interest (ROI) of the specimen with remote focal scanning OPT [52] but the acquisition protocol only works in ring-like areas centered on the axis of rotation.

The other approach combines imaging modalities. For example, Arranz *et al.* [51] proposed an OPT design incorporating a light sheet illumination arm. The idea is to acquire the whole volumetric information with OPT, and then target ROIs with an enhanced resolution using light sheet illumination. In the same manner, we investigated the combination of OPT with structured illumination microscopy (SIM).

In this last Chapter, I will provide an outlook of how we aim to combine SIM and OPT. First, I will give a brief description of SIM and its implementation within an OPT instrument (Section 6.1). Then I will review the remaining challenges, which have yet to be overcome and our strategy to solve them (Section 6.2). Finally, I will conclude this thesis with a few words on the impact of our achievements in the duration of this work (Section 6.3).

6.1 Structured illumination microscopy with OPT

Theory and algorithm

SIM is often referenced as a super-resolution (SR) imaging technique [159, 160], but in the combination with OPT we are interested in its optical sectioning (OS-) capacity [161, 162]. In OS-SIM, the intensity in the sample plane is modulated with sinusoidal patterns, sequentially and equally phase-shifted by $\phi_1 = 0°$, $\phi_2 = 120°$, and $\phi_3 = 240°$. These patterns P_i can be expressed mathematically as

$$P_i = P_0\left[1 + \sin(2\pi k_0 x + \phi_i)\right] \quad \text{with} \quad i \in \{1,2,3\}, \tag{6.1}$$

where P_0 is the illumination intensity without modulation, k_0 the modulation frequency, and ϕ_i the corresponding phase-shift. The images I_i recorded by the detector can therefore be written as

$$I_i(x,y) = \left(P_i(x,y) \cdot O(x,y)\right) * h(x,y) \quad \text{with} \quad i \in \{1,2,3\}, \tag{6.2}$$

where O is the object in the sample plane, h the instrument point spread function (PSF), and (x, y) the spatial coordinates. The optically-sectioned image I_{OS} is then computed as

$$I_{OS} = \frac{\sqrt{2}}{3}\sqrt{(I_1 - I_2)^2 + (I_2 - I_3)^2 + (I_3 - I_1)^2}. \tag{6.3}$$

To simplify image processing, we used the SIMToolbox [163] developed partially by a colleague in the group to process OS-SIM images. This toolbox is based on maximum a posteriori probability image estimation [164]. It is an iterative approach which solves the inverse problem of computing the OS-SIM image based on the acquired images I_i. It has the advantage of not requiring prior knowledge of the PSF and pattern positions.

Instrument design

The critical component of a SIM instrument is the spatial light modulator (SLM). In recent designs, it is often a pixelated device that creates the illumination patterns by varying the light beam intensity. There are two primary types of pixelated SLM: liquid crystals on silicon (LCOS) [165] and digital micromirror devices (DMD) [166]. LCOS devices are a matrix of liquid crystals on a mirror surface. They allow grayscale values of intensity modulation and have smaller pixels. However, they are polarization-dependent. DMDs are composed of thousands of micromirrors that can be tilted to separate the light beam into an “on” or “off” state. They have a broader spectral response than LCOS and can be used without polarization control. We chose to implement our OS-SIM instrument with a DMD and reuse the OPT LEDs as the light source (see Figure 6.1). The pattern contrast is assumed to be better with a DMD when using LEDs, due to their spectral bandwith [167].

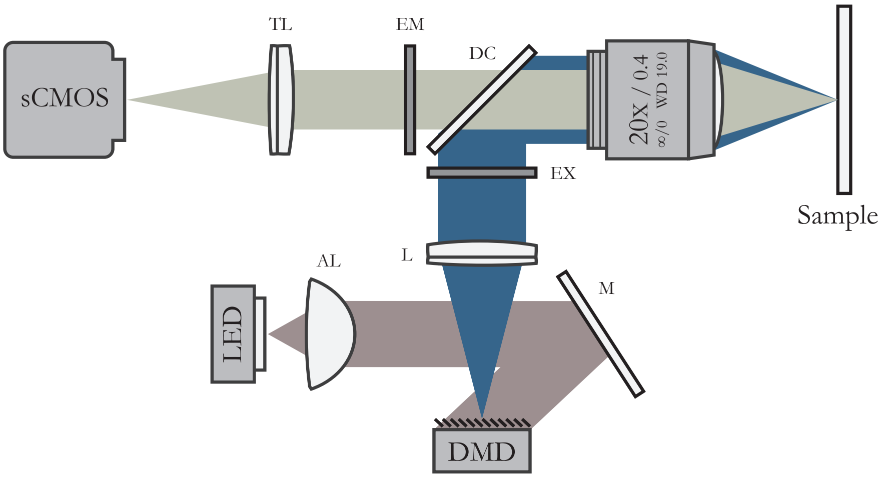

Figure 6.1 – SIM instrument design. It uses LEDs and a DMD to generate a patterned illumination on the sample. The resulting fluorescence signal is collected on an sCMOS detector through a filter set. The filter set is composed of an excitation filter EX, an emission filter EM, and a dichroic mirror DC. A 20X long-working-distance (19 mm) objective with a numerical aperture (NA) of 0.4 is used in view of imaging whole mouse organs. AL, aspheric lens; L, achromatic lens (f=150 mm); M, mirror; TL, tube lens.

The OS-SIM specifications in air with a $20X$ Nikon objective lens (TU Plan EPI ELWD, $20X$, NA=0.4, working distance=19 mm) are a FOV of 0.67 × 0.67 mm^2 and a resolution of approximately 0.7 µm. The instrument was first implemented in a stand-alone version to evaluate its performance without disturbing the experiments running with the OPT instrument. Ultimately, the OS-SIM was meant to be combined with the OPT in a single apparatus (see Figure 6.2). The two modalities cover different scales: a whole volumetric scan with OPT provides an overview of the sample while a series of SIM images provides high-resolution information in selected ROIs.

Next, we qualitatively validated the OS-SIM performance with a Zeiss fluorescence test slide

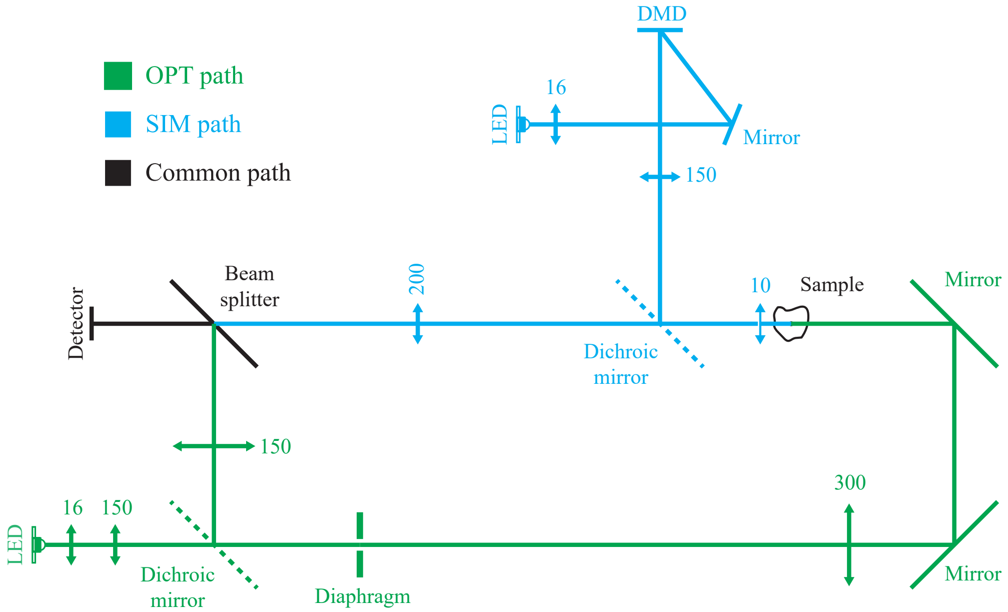

Figure 6.2 – Combination of the SIM and OPT modalities in a single instrument. The number above each lens indicates its focal length. Fluorescence filters are omitted for clarity. After a whole volumetric scan of the sample with OPT, regions of interest can be imaged at a higher resolution with SIM.

(see Figure 6.3) and a 460-nm high-power LED (PT-121-B, Luminus). This sample comes from a highly autofluorescent flower *Convallaria majalis*. The average of the sample images acquired with the different illumination patterns, which corresponds to a widefield fluorescence microscopy version of the sample, remains slightly blurred, although the focus was adjusted precisely (Figure 6.3(a)). The blur is mostly caused by out-of-focus light coming from the sample part that is not contained within the imaging plane. When processed with the SIMToolbox (Figure 6.3(b)), the patterned images give a sharper result with increased contrast (striking examples are pointed out by the white arrowheads). A complete characterization of the OS-SIM setup would be desirable. However, we were more concerned about the challenges of imaging thick specimens, such as mouse organs.

Whole mouse organs prepared for OPT require submersion in a glass cuvette filled with refractive-index-matching liquid before imaging. In the OPT instrument, this change in refractive index along the detection axis produces negligible aberrations on the projections because of the low (0.01) NA used. However, in the OS-SIM instrument, the NA is 0.4 with an objective lens designed to operate in air and aberrations have to be considered.

6.2 Aberration correction

Imaging of whole mouse organs requires the use of objectives with a long working-distance in the order of the tissue thickness (approximately 10 mm). However, commercially-available

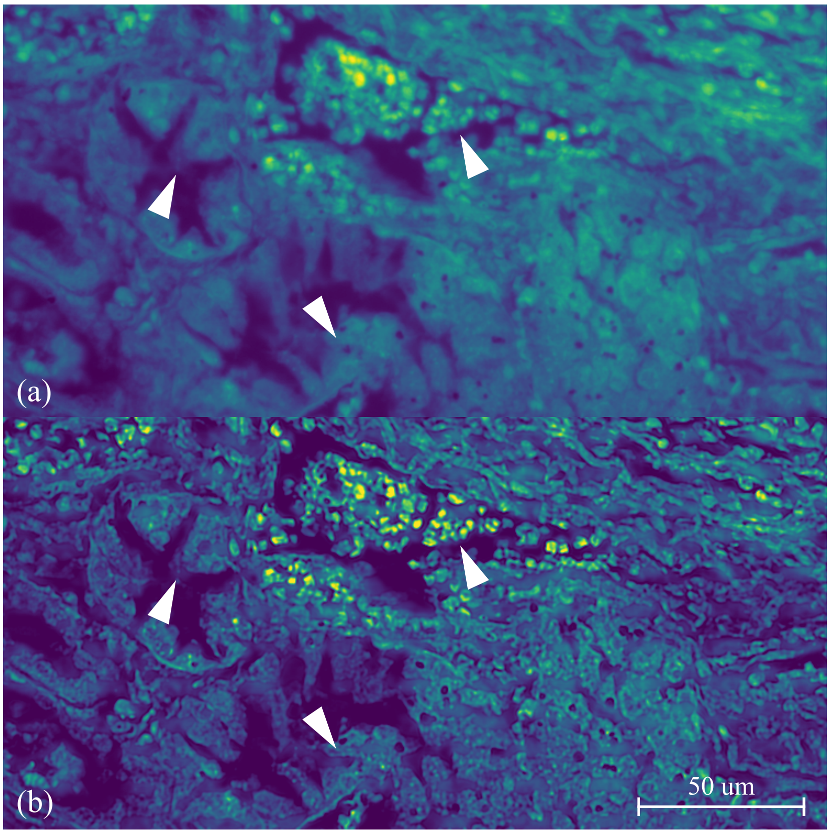

Figure 6.3 – Validation of the OS-SIM instrument with the Zeiss fluorescence test slide. (a) Average of the images recorded on the detector. (b) MAP-SIM result computed with the SIMToolbox from the same images. Arrowheads point towards regions in the image where optical sectioning improved the contrast.

solutions are usually designed for operation in air. When these objectives are used to image in a surrounding medium that has a different refractive index, the image quality significantly degrades as reported by Dodt *et al.* [168] in ultramicroscopy. Briefly, the refraction of light occurring at the interface of a refractive-index mismatch causes strong spherical aberrations, and the light beam fails to focus on a single point. This results in a distorted image on the detector. To address the aberration problem, we used the OS-SIM in widefield mode, *i.e.*, setting all the micromirrors to the “on” state and having a homogeneous illumination on the sample.

The advances of mesoscopic imaging techniques over the past 20 years have recently fostered the development of aberration-correction strategies to use commercial long-working-distance objective lenses [10, 169]. However, these complex strategies are application- and objective-lens-dependant. Before trying them, we decided to perform optical design simulations of the OS-SIM instrument detection (see Figure 6.4) with OpticStudio 15 (Zemax LLC, America). First, we modeled the objective lens with a lens tandem composed of two paraxial lenses (f=9.5 mm, and f=−10 mm) separated by 9 mm (Figure 6.4(a)). This lens tandem has the same working distance (19 mm), and focal length (f=10 mm) as the Nikon objective lens. The tube lens was a paraxial lens (f=200 mm). Then we added the BABB (10 mm) and the glass cuvette wall (2.5 mm) starting from the sample plane (on the left in Figure 6.4(a)).

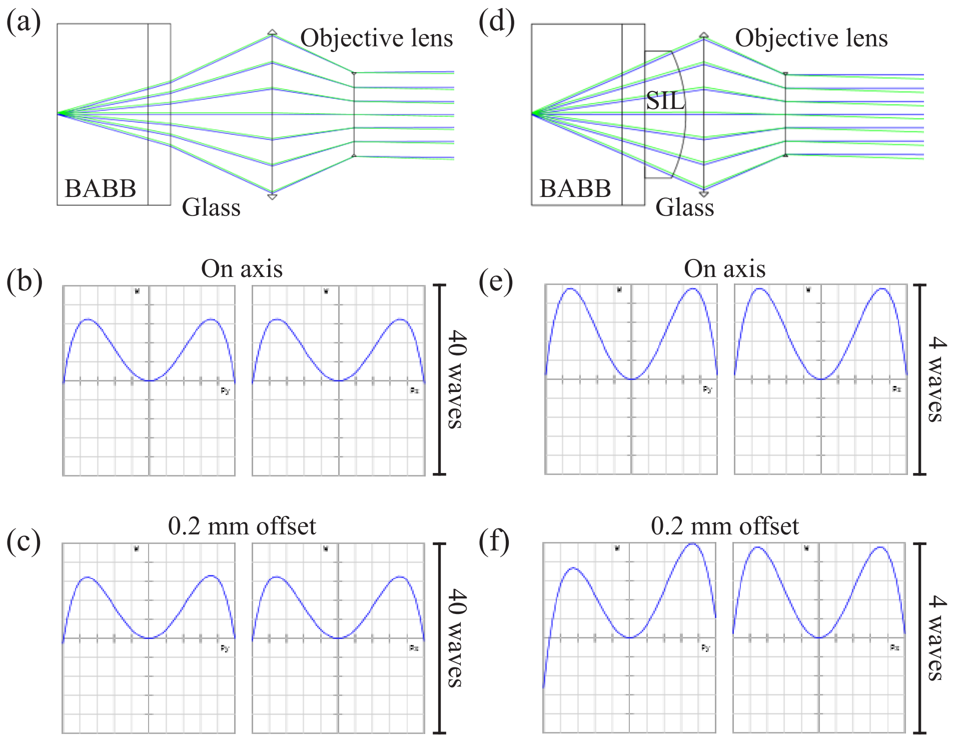

Figure 6.4 – Spherical aberration correction concept. (a) Simulation of the detection rays on the objective-lens side, a 10 mm layer of BABB and 2.5 mm of glass create an interface for light refraction and aberrations. Blue rays come from the optical axis and green rays from 0.2 mm away in the same imaging plane. (b)-(c) Optical path difference of corresponding rays measured in the detector plane. (d) Correction with a SIL that makes an orthogonal surface to the rays and reduces the refraction effect. (e)-(f) Optical path differences after correction with a SIL.

Finally, we measured the optical path difference (OPD) in the detector plane (Figure 6.4(b)-(c)). The OPD is a quantity that expresses the deviation in the wavefront compared to an aberration-free system. It is measured in waves, and if below 1, the imaging optics is said to be diffraction-limited. The OPD measured with BABB and the glass cuvette wall is approximately 13 waves, which suggest that a strong degradation of the image quality will result. Images of fluorescent microparticles with the OS-SIM instrument in air and through approximately 10 mm of BABB and 2.5 mm of glass concur the simulation result and highlight the degradation in image quality experimentally (Figure 6.5(a), (d) and (b), (e)). The microparticle size in these experiments was limited to minimum 5 μm because smaller ones vanished completely due to aberrations.

Our approach to correct aberrations in the OS-SIM instrument is based on the solid immer-

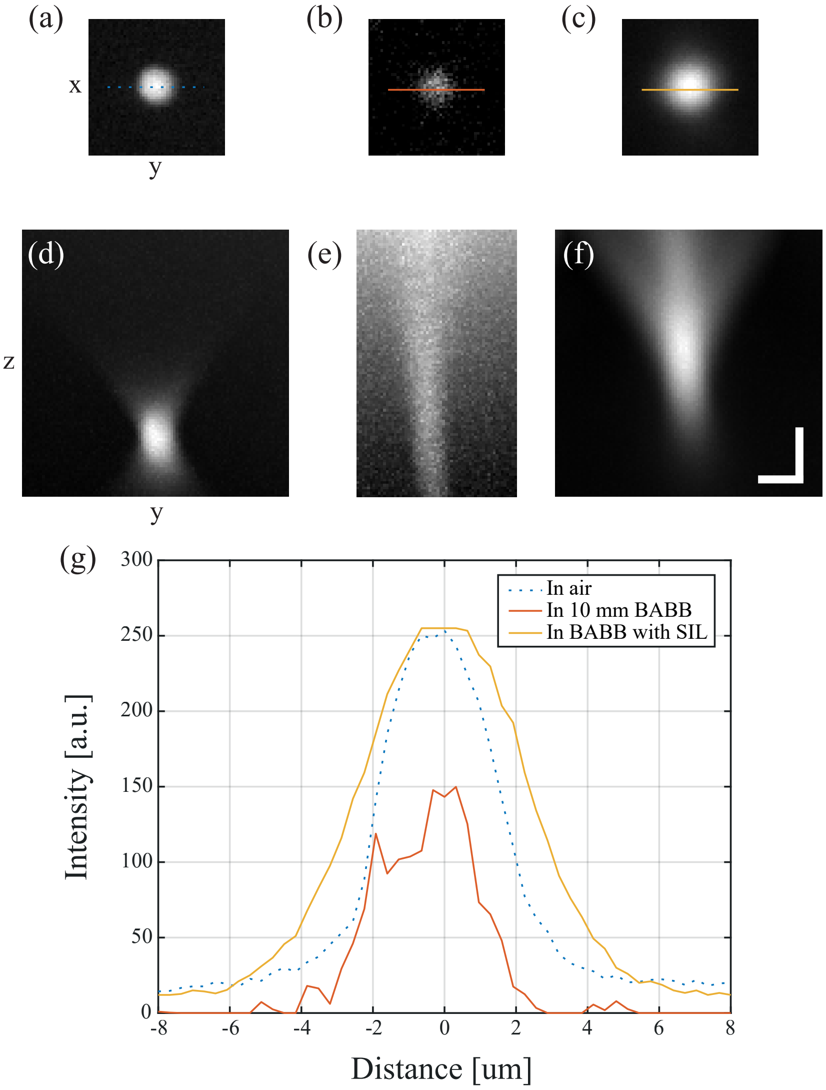

Figure 6.5 – Evaluation of the aberration correction with a SIL. (a) Five-micrometer fluorescent microparticle imaged in air with the OS-SIM in brightfield mode. (b) Microparticle imaged through approximately 10 mm of BABB and 2.5 mm of glass. (c) Microparticle imaged through BABB and glass and a SIL. (d-f) Corresponding cross sections along the optical axis. (g) Line plots through the microparticles in (a)-(c) showing their profile. The air curve is dotted because it was acquired with different exposure time, 0.02 s instead of 0.5 s for the other two. Scale bars: 5 µm.

sion principle [170]. We modeled a solid immersion lens (SIL) that is mounted on the glass cuvette wall (Figure 6.4(d)) and calculated a surface curvature that minimizes the refraction at the interface of refractive-index-mismatch. This condition is satisfied when the surface is orthogonal to the focused rays. After optimization, we measured an OPD of approximately 2 waves (Figure 6.4(e)-(f)), which is still considered to be limited by aberrations but is closer to the diffraction limit. Finally, we imaged microparticles with the OS-SIM instrument, and a SIL (LA1255-A, Thorlabs) glued to the cuvette wall (Figure 6.5(c) and (f)). With the aberration correction, the microparticle has an improved contrast when compared to the case with BABB and glass only (exposure time of 0.5 s in both images). However, the microparticle intensity is still lower than the one obtained when it is imaged in air (exposure time of 0.02 s).

The current aberration-correction is insufficient to image whole mouse organs prepared for OPT. The opportunity to try more advanced aberration-correction techniques such as adaptive optics [171, 172] however remains open.

6.3 Final words

In my thesis, we fostered the development of optical projection tomography. We started by designing a custom instrument for whole mouse organ imaging, which was fully described in a first journal publication (2017) [55]. This instrument was duplicated in the group of Professor Holmberg (Lund University, Sweden) where it is available and regularly utilized as a platform for 3D imaging of large specimens. Then, we shared our practical experience with the instrument in a second research article (submitted to Optics Express, December 2018). We also highlighted the use of OPT in Alzheimer's research by imaging whole mouse brains with amyloidosis at different ages, as described in our last article (submitted to Biomedical Optics Express, December 2018). Our efforts were oriented towards the dissemination of the technology and making it more accessible to inexperienced users. We went on to try bridging the scales in combining structured illumination microscopy and OPT, following the needs of life scientists to have an overview of their samples and high-resolution images in regions of interest. In this context, we demonstrated the use of solid immersion lenses for the correction of spherical aberrations arising when imaging through a cuvette and index-matching liquid. The complete correction of these aberrations will require more advanced techniques, such as adaptive optics, but we are confident that this problem can be overcome.

A Image portfolio

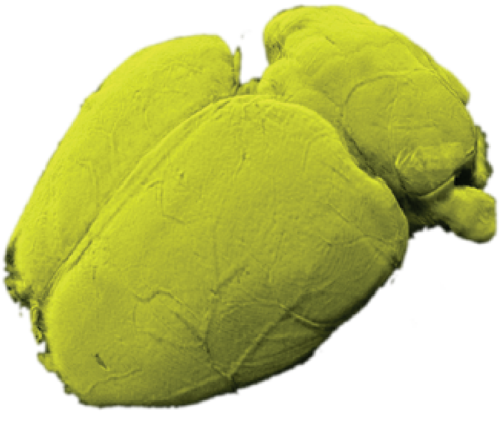

Seeing is believing

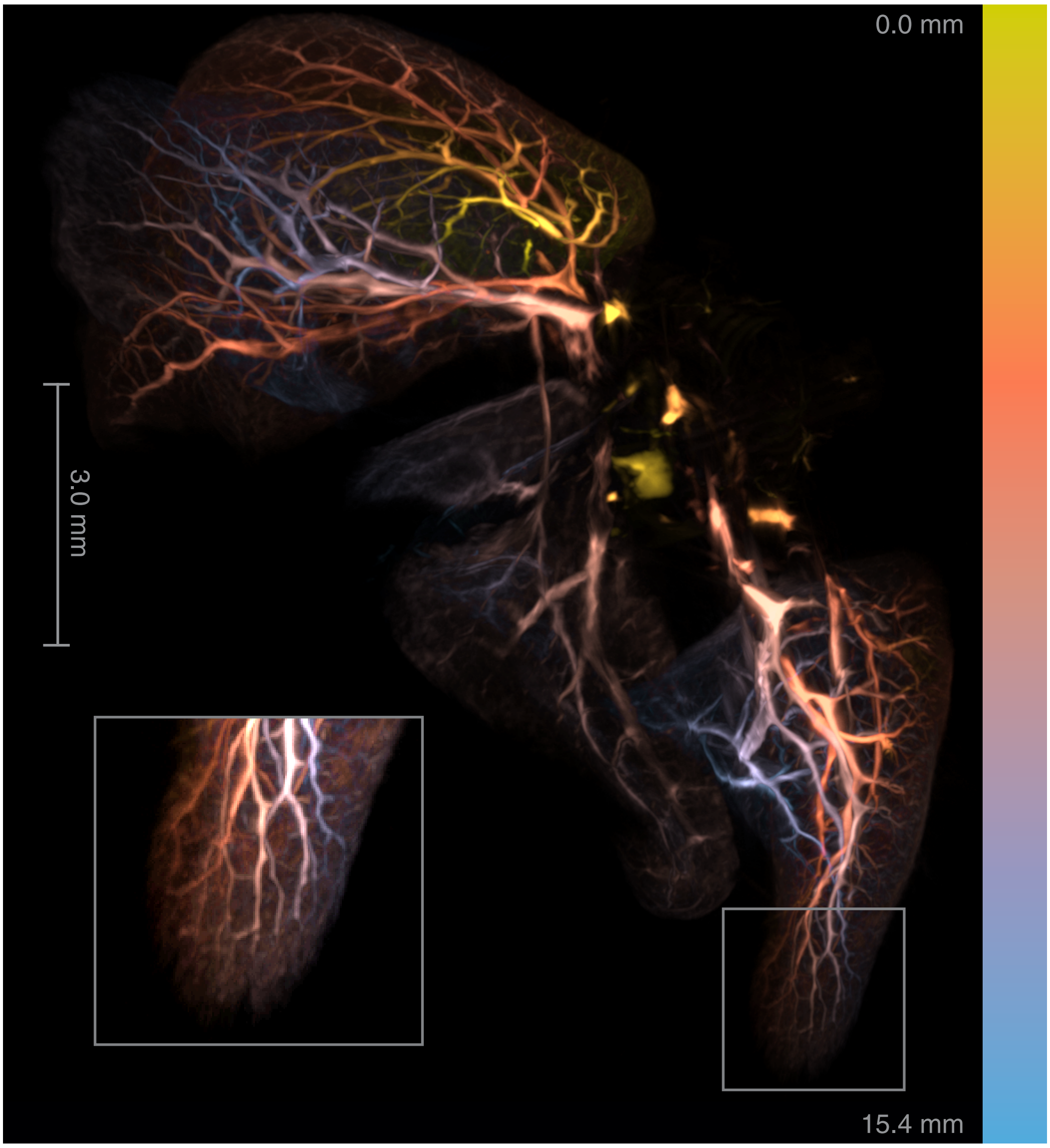

Figure A.1 – Depth-color-coded maximum intensity projection of the vasculature in a whole mouse lung acquired with optical projection tomography.

Figure A.2 – Maximum intensity projection of the barbs in a cockatiel feather acquired with optical-sectioning structured illumination microscopy. This image ranked among the top 10 winners of the “When Aesthetics meets Innovation” photo contest (EPFL, Switzerland).

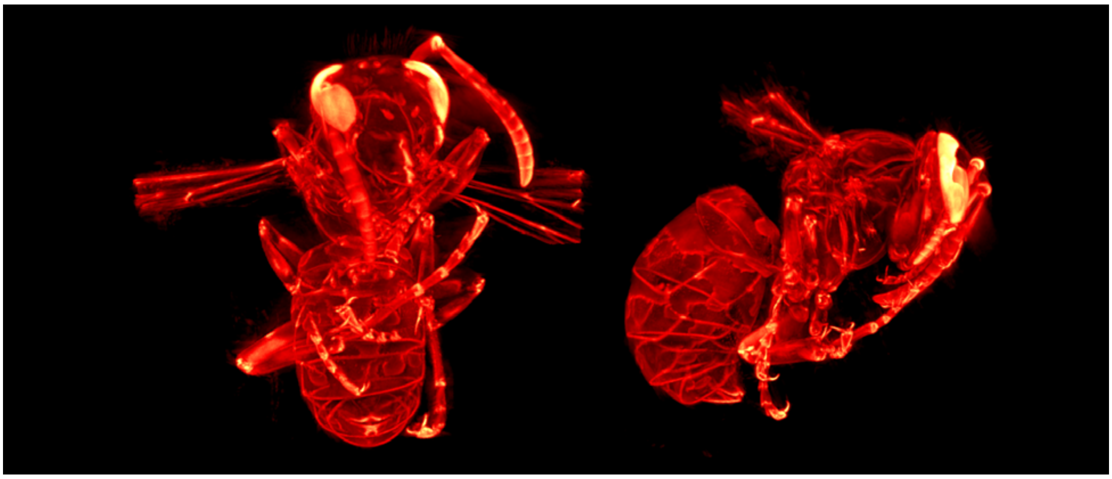

Figure A.3 – Maximum intensity projections of a wasp acquired with optical projection tomography.

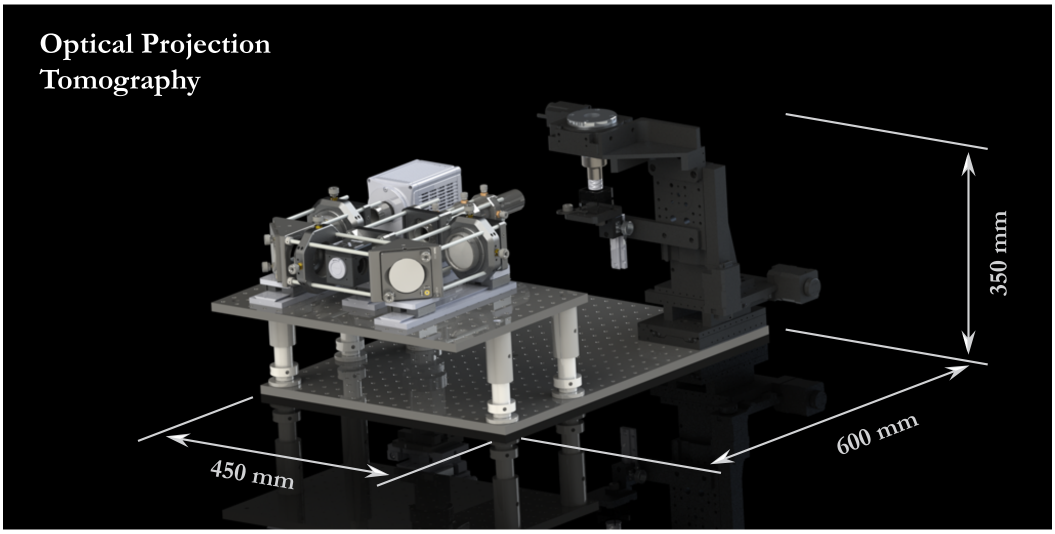

Figure A.4 – CAD rendering of the OPT instrument.

Bibliography

[1] Z. Sun, K. Ng, and N. Ramli, "Biomedical imaging research: a fast-emerging area for interdisciplinary collaboration," *Biomedical imaging and intervention journal*, vol. 7, no. 3, 2011.

[2] M. Rudin, N. Beckmann, and M. Rausch, "Magnetic resonance imaging in biomedical research: Imaging of drugs and drug effects," in *Methods in enzymology*, vol. 385, pp. 240–256, Elsevier, 2004.

[3] P. Raghavendra and T. Pullaiah, *Advances in Cell and Molecular Diagnostics.* Academic Press, 2018.

[4] M. M. Khalil, J. L. Tremoleda, T. B. Bayomy, and W. Gsell, "Molecular spect imaging: an overview," *International journal of molecular imaging*, vol. 2011, 2011.

[5] D. Stucht, K. A. Danishad, P. Schulze, F. Godenschweger, M. Zaitsev, and O. Speck, "Highest resolution in vivo human brain mri using prospective motion correction," *PloS one*, vol. 10, no. 7, p. e0133921, 2015.

[6] A. du Plessis, S. G. le Roux, and A. Guelpa, "Comparison of medical and industrial x-ray computed tomography for non-destructive testing," *Case Studies in Nondestructive Testing and Evaluation*, vol. 6, pp. 17–25, 2016.

[7] C. Baltes, N. Radzwill, S. Bosshard, D. Marek, and M. Rudin, "Micro mri of the mouse brain using a novel 400 mhz cryogenic quadrature rf probe," *NMR in Biomedicine: An International Journal Devoted to the Development and Application of Magnetic Resonance In vivo*, vol. 22, no. 8, pp. 834–842, 2009.

[8] V. Ntziachristos and D. Razansky, "Molecular imaging by means of multispectral optoacoustic tomography (msot)," *Chemical reviews*, vol. 110, no. 5, pp. 2783–2794, 2010.

[9] J. Sharpe, U. Ahlgren, P. Perry, B. Hill, A. Ross, J. Hecksher-Sørensen, R. Baldock, and D. Davidson, "Optical projection tomography as a tool for 3d microscopy and gene expression studies," *Science*, vol. 296, no. 5567, pp. 541–545, 2002.

[10] M. Pende, K. Becker, M. Wanis, S. Saghafi, R. Kaur, C. Hahn, N. Pende, M. Foroughipour, T. Hummel, and H.-U. Dodt, "High-resolution ultramicroscopy of the developing and

adult nervous system in optically cleared drosophila melanogaster," *Nature Communications*, vol. 9, no. 1, p. 4731, 2018.

[11] A. F. Fercher, W. Drexler, C. K. Hitzenberger, and T. Lasser, "Optical coherence tomography-principles and applications," *Reports on progress in physics*, vol. 66, no. 2, p. 239, 2003.

[12] V. Ntziachristos, "Going deeper than microscopy: the optical imaging frontier in biology," *Nature methods*, vol. 7, no. 8, p. 603, 2010.

[13] A. Rehemtulla, L. D. Stegman, S. J. Cardozo, S. Gupta, D. E. Hall, C. H. Contag, and B. D. Ross, "Rapid and quantitative assessment of cancer treatment response using in vivo bioluminescence imaging," *Neoplasia*, vol. 2, no. 6, pp. 491–495, 2000.

[14] T. Deffieux, C. Demene, M. Pernot, and M. Tanter, "Functional ultrasound neuroimaging: a review of the preclinical and clinical state of the art," *Current opinion in neurobiology*, vol. 50, pp. 128–135, 2018.

[15] A. M. Cormack, "Representation of a function by its line integrals, with some radiological applications," *Journal of applied physics*, vol. 34, no. 9, pp. 2722–2727, 1963.

[16] G. N. Hounsfield, "Computerized transverse axial scanning (tomography): Part 1. description of system," *The British journal of radiology*, vol. 46, no. 552, pp. 1016–1022, 1973.

[17] A. Shukla and U. Kumar, "Positron emission tomography: An overview," *Journal of medical physics/Association of Medical Physicists of India*, vol. 31, no. 1, p. 13, 2006.

[18] P. C. Lauterbur *et al.*, "Image formation by induced local interactions: examples employing nuclear magnetic resonance," 1973.

[19] R. H. Webb, "Confocal optical microscopy," *Reports on Progress in Physics*, vol. 59, no. 3, p. 427, 1996.

[20] W. R. Zipfel, R. M. Williams, and W. W. Webb, "Nonlinear magic: multiphoton microscopy in the biosciences," *Nature biotechnology*, vol. 21, no. 11, p. 1369, 2003.

[21] J. G. Fujimoto and D. Farkas, *Biomedical optical imaging.* Oxford University Press, 2009.

[22] A. Descloux, K. Grußmayer, E. Bostan, T. Lukes, A. Bouwens, A. Sharipov, S. Geissbuehler, A.-L. Mahul-Mellier, H. Lashuel, M. Leutenegger, *et al.*, "Combined multi-plane phase retrieval and super-resolution optical fluctuation imaging for 4d cell microscopy," *Nature Photonics*, vol. 12, no. 3, p. 165, 2018.

[23] J. S. Lewis, S. Achilefu, J. Garbow, R. Laforest, and M. Welch, "Small animal imaging: current technology and perspectives for oncological imaging," *European journal of cancer*, vol. 38, no. 16, pp. 2173–2188, 2002.

[24] D. W. Holdsworth and M. M. Thornton, "Micro-ct in small animal and specimen imaging," *Trends in Biotechnology*, vol. 20, no. 8, pp. S34–S39, 2002.

[25] M. J. Paulus, S. S. Gleason, S. J. Kennel, P. R. Hunsicker, and D. K. Johnson, "High resolution x-ray computed tomography: an emerging tool for small animal cancer research," *Neoplasia*, vol. 2, no. 1-2, pp. 62–70, 2000.

[26] H. Benveniste and S. Blackband, "Mr microscopy and high resolution small animal mri: applications in neuroscience research," *Progress in neurobiology*, vol. 67, no. 5, pp. 393–420, 2002.

[27] V. Herold, P. Mörchel, C. Faber, E. Rommel, A. Haase, and P. M. Jakob, "In vivo quantitative three-dimensional motion mapping of the murine myocardium with pc-mri at 17.6 t," *Magnetic Resonance in Medicine: An Official Journal of the International Society for Magnetic Resonance in Medicine*, vol. 55, no. 5, pp. 1058–1064, 2006.

[28] C. R. Jack Jr, M. Garwood, T. M. Wengenack, B. Borowski, G. L. Curran, J. Lin, G. Adriany, O. H. Gröhn, R. Grimm, and J. F. Poduslo, "In vivo visualization of alzheimer's amyloid plaques by magnetic resonance imaging in transgenic mice without a contrast agent," *Magnetic Resonance in Medicine: An Official Journal of the International Society for Magnetic Resonance in Medicine*, vol. 52, no. 6, pp. 1263–1271, 2004.

[29] H.-P. F. Brecht, R. Su, M. P. Fronheiser, S. A. Ermilov, A. Conjusteau, and A. A. Oraevsky, "Whole-body three-dimensional optoacoustic tomography system for small animals," *Journal of biomedical optics*, vol. 14, no. 6, p. 064007, 2009.

[30] D. Razansky, C. Vinegoni, and V. Ntziachristos, "Imaging of mesoscopic-scale organisms using selective-plane optoacoustic tomography," *Physics in Medicine & Biology*, vol. 54, no. 9, p. 2769, 2009.

[31] W. Lu, Q. Huang, G. Ku, X. Wen, M. Zhou, D. Guzatov, P. Brecht, R. Su, A. Oraevsky, L. V. Wang, *et al.*, "Photoacoustic imaging of living mouse brain vasculature using hollow gold nanospheres," *Biomaterials*, vol. 31, no. 9, pp. 2617–2626, 2010.

[32] C. H. Contag and B. D. Ross, "It's not just about anatomy: in vivo bioluminescence imaging as an eyepiece into biology," *Journal of Magnetic Resonance Imaging: An Official Journal of the International Society for Magnetic Resonance in Medicine*, vol. 16, no. 4, pp. 378–387, 2002.

[33] H.-U. Dodt, U. Leischner, A. Schierloh, N. Jährling, C. P. Mauch, K. Deininger, J. M. Deussing, M. Eder, W. Zieglgänsberger, and K. Becker, "Ultramicroscopy: three-dimensional visualization of neuronal networks in the whole mouse brain," *Nature methods*, vol. 4, no. 4, p. 331, 2007.

[34] M. Weber, M. Mickoleit, and J. Huisken, "Light sheet microscopy," in *Methods in cell biology*, vol. 123, pp. 193–215, Elsevier, 2014.

[35] B.-C. Chen, W. R. Legant, K. Wang, L. Shao, D. E. Milkie, M. W. Davidson, C. Janetopoulos, X. S. Wu, J. A. Hammer, Z. Liu, *et al.*, "Lattice light-sheet microscopy: imaging molecules to embryos at high spatiotemporal resolution," *Science*, vol. 346, no. 6208, p. 1257998, 2014.

[36] R. Menzel, "Ultramicroscopy–imaging a whole animal or a whole brain with micron resolution," *Frontiers in neuroscience*, vol. 5, p. 11, 2011.

[37] P. J. Keller and H.-U. Dodt, "Light sheet microscopy of living or cleared specimens," *Current opinion in neurobiology*, vol. 22, no. 1, pp. 138–143, 2012.

[38] M. B. Ahrens, M. B. Orger, D. N. Robson, J. M. Li, and P. J. Keller, "Whole-brain functional imaging at cellular resolution using light-sheet microscopy," *Nature methods*, vol. 10, no. 5, p. 413, 2013.

[39] P. J. Keller and M. B. Ahrens, "Visualizing whole-brain activity and development at the single-cell level using light-sheet microscopy," *Neuron*, vol. 85, no. 3, pp. 462–483, 2015.

[40] A. Kaufmann, M. Mickoleit, M. Weber, and J. Huisken, "Multilayer mounting enables long-term imaging of zebrafish development in a light sheet microscope," *Development*, vol. 139, no. 17, pp. 3242–3247, 2012.

[41] P. J. Keller, A. D. Schmidt, A. Santella, K. Khairy, Z. Bao, J. Wittbrodt, and E. H. Stelzer, "Fast, high-contrast imaging of animal development with scanned light sheet–based structured-illumination microscopy," *Nature methods*, vol. 7, no. 8, p. 637, 2010.

[42] L. Silvestri, A. Bria, L. Sacconi, G. Iannello, and F. Pavone, "Confocal light sheet microscopy: micron-scale neuroanatomy of the entire mouse brain," *Optics express*, vol. 20, no. 18, pp. 20582–20598, 2012.

[43] N. Jährling, K. Becker, B. M. Wegenast-Braun, S. A. Grathwohl, M. Jucker, and H.-U. Dodt, "Cerebral β-amyloidosis in mice investigated by ultramicroscopy," *PloS one*, vol. 10, no. 5, p. e0125418, 2015.

[44] J. Sharpe, "Optical projection tomography as a new tool for studying embryo anatomy," *Journal of anatomy*, vol. 202, no. 2, pp. 175–181, 2003.

[45] M. D. Wong, J. Dazai, J. R. Walls, N. W. Gale, and R. M. Henkelman, "Design and implementation of a custom built optical projection tomography system," *PloS one*, vol. 8, no. 9, p. e73491, 2013.

[46] A. Bassi, L. Fieramonti, C. D'Andrea, G. Valentini, and M. Mione, "In vivo label-free three-dimensional imaging of zebrafish vasculature with optical projection tomography," *Journal of biomedical optics*, vol. 16, no. 10, p. 100502, 2011.

[47] T. Alanentalo, A. Asayesh, H. Morrison, C. E. Lorén, D. Holmberg, J. Sharpe, and U. Ahlgren, "Tomographic molecular imaging and 3d quantification within adult mouse organs," *Nature methods*, vol. 4, no. 1, p. 31, 2007.

[48] T. Alanentalo, C. E. Loren, A. Larefalk, J. Sharpe, D. Holmberg, and U. Ahlgren, "High-resolution three-dimensional imaging of islet-infiltrate interactions based on optical projection tomography assessments of the intact adult mouse pancreas," *Journal of biomedical optics*, vol. 13, no. 5, p. 054070, 2008.

[49] T. Alanentalo, A. Hörnblad, S. Mayans, A. K. Nilsson, J. Sharpe, Å. Larefalk, U. Ahlgren, and D. Holmberg, "Quantification and 3-d imaging of the insulitis-induced destruction of β-cells in murine type 1 diabetes," *Diabetes*, 2010.

[50] J. A. Gleave, M. D. Wong, J. Dazai, M. Altaf, R. Mark Henkelman, J. P. Lerch, and B. J. Nieman, "Neuroanatomical phenotyping of the mouse brain with three-dimensional autofluorescence imaging," *Physiological genomics*, vol. 44, no. 15, pp. 778–785, 2012.

[51] A. Arranz, D. Dong, S. Zhu, M. Rudin, C. Tsatsanis, J. Tian, and J. Ripoll, "Helical optical projection tomography," *Optics express*, vol. 21, no. 22, pp. 25912–25925, 2013.

[52] T. Watson, N. Andrews, S. Davis, L. Bugeon, M. D. Dallman, and J. McGinty, "Optim: Optical projection tomography integrated microscope using open-source hardware and software," *PloS one*, vol. 12, no. 7, p. e0180309, 2017.

[53] A. K. Trull, J. van der Horst, W. J. Palenstijn, L. J. van Vliet, T. van Leeuwen, and J. Kalkman, "Point spread function based image reconstruction in optical projection tomography," *Physics in Medicine & Biology*, vol. 62, no. 19, p. 7784, 2017.

[54] A. K. Trull, J. van der Horst, L. J. van Vliet, and J. Kalkman, "Comparison of image reconstruction techniques for optical projection tomography," *Applied optics*, vol. 57, no. 8, pp. 1874–1882, 2018.

[55] D. Nguyen, P. J. Marchand, A. L. Planchette, J. Nilsson, M. Sison, J. Extermann, A. Lopez, M. Sylwestrzak, J. Sordet-Dessimoz, A. Schmidt-Christensen, *et al.*, "Optical projection tomography for rapid whole mouse brain imaging," *Biomedical optics express*, vol. 8, no. 12, pp. 5637–5650, 2017.

[56] Alzheimer's Association and others, "2018 alzheimer's disease facts and figures," *Alzheimer's & Dementia*, vol. 14, no. 3, pp. 367–429, 2018.

[57] M. Prince, R. Bryce, E. Albanese, A. Wimo, W. Ribeiro, and C. P. Ferri, "The global prevalence of dementia: a systematic review and metaanalysis," *Alzheimer's & dementia*, vol. 9, no. 1, pp. 63–75, 2013.

[58] C. P. Ferri, M. Prince, C. Brayne, H. Brodaty, L. Fratiglioni, M. Ganguli, K. Hall, K. Hasegawa, H. Hendrie, Y. Huang, *et al.*, "Global prevalence of dementia: a delphi consensus study," *The lancet*, vol. 366, no. 9503, pp. 2112–2117, 2005.

[59] R. Brookmeyer, E. Johnson, K. Ziegler-Graham, and H. M. Arrighi, "Forecasting the global burden of alzheimer's disease," *Alzheimer's & dementia*, vol. 3, no. 3, pp. 186–191, 2007.

[60] M. Wortmann, "Dementia: a global health priority-highlights from an adi and world health organization report," *Alzheimer's research & therapy*, vol. 4, no. 5, p. 40, 2012.

[61] G. McKhann, D. Drachman, M. Folstein, R. Katzman, D. Price, and E. M. Stadlan, "Clinical diagnosis of alzheimer's disease report of the nincds-adrda work group* under the auspices of department of health and human services task force on alzheimer's disease," *Neurology*, vol. 34, no. 7, pp. 939–939, 1984.

[62] G. M. McKhann, D. S. Knopman, H. Chertkow, B. T. Hyman, C. R. Jack Jr, C. H. Kawas, W. E. Klunk, W. J. Koroshetz, J. J. Manly, R. Mayeux, *et al.*, "The diagnosis of dementia due to alzheimer's disease: Recommendations from the national institute on aging-alzheimer's association workgroups on diagnostic guidelines for alzheimer's disease," *Alzheimer's & dementia*, vol. 7, no. 3, pp. 263–269, 2011.

[63] B. Dubois, H. H. Feldman, C. Jacova, J. L. Cummings, S. T. DeKosky, P. Barberger-Gateau, A. Delacourte, G. Frisoni, N. C. Fox, D. Galasko, *et al.*, "Revising the definition of alzheimer's disease: a new lexicon," *The Lancet Neurology*, vol. 9, no. 11, pp. 1118–1127, 2010.

[64] L. M. Ittner and J. Götz, "Amyloid-β and tau—a toxic pas de deux in alzheimer's disease," *Nature Reviews Neuroscience*, vol. 12, no. 2, p. 67, 2011.

[65] J. A. Hardy and G. A. Higgins, "Alzheimer's disease: the amyloid cascade hypothesis," *Science*, vol. 256, no. 5054, p. 184, 1992.

[66] J. Hardy and D. J. Selkoe, "The amyloid hypothesis of alzheimer's disease: progress and problems on the road to therapeutics," *science*, vol. 297, no. 5580, pp. 353–356, 2002.

[67] W. E. Klunk, H. Engler, A. Nordberg, Y. Wang, G. Blomqvist, D. P. Holt, M. Bergström, I. Savitcheva, G.-F. Huang, S. Estrada, *et al.*, "Imaging brain amyloid in alzheimer's disease with pittsburgh compound-b," *Annals of Neurology: Official Journal of the American Neurological Association and the Child Neurology Society*, vol. 55, no. 3, pp. 306–319, 2004.

[68] T. Bolmont, A. Bouwens, C. Pache, M. Dimitrov, C. Berclaz, M. Villiger, B. M. Wegenast-Braun, T. Lasser, and P. C. Fraering, "Label-free imaging of cerebral β-amyloidosis with extended-focus optical coherence microscopy," *Journal of Neuroscience*, vol. 32, no. 42, pp. 14548–14556, 2012.

[69] B. Dubois, H. H. Feldman, C. Jacova, H. Hampel, J. L. Molinuevo, K. Blennow, S. T. DeKosky, S. Gauthier, D. Selkoe, R. Bateman, *et al.*, "Advancing research diagnostic criteria for alzheimer's disease: the iwg-2 criteria," *The Lancet Neurology*, vol. 13, no. 6, pp. 614–629, 2014.

[70] G. Yamin and D. B. Teplow, "Pittsburgh compound-b (pib) binds amyloid β-protein protofibrils," *Journal of neurochemistry*, vol. 140, no. 2, pp. 210–215, 2017.

[71] G. A. Elder, M. A. Gama Sosa, and R. De Gasperi, "Transgenic mouse models of alzheimer's disease," *Mount Sinai Journal of Medicine: A Journal of Translational and Personalized Medicine: A Journal of Translational and Personalized Medicine*, vol. 77, no. 1, pp. 69–81, 2010.

[72] T. Wengenack, S. Whelan, G. Curran, K. Duff, and J. Poduslo, "Quantitative histological analysis of amyloid deposition in alzheimer's double transgenic mouse brain," *Neuroscience*, vol. 101, no. 4, pp. 939–944, 2000.

[73] A. C. Kak and M. Slaney, *Principles of computerized tomographic imaging.* IEEE press New York, 1988.

[74] J. H. Lambert, *Photometria sive de mensura et gradibus luminis, colorum et umbrae.* Klett, 1760.

[75] J. Radon, "On the determination of functions from their integral values along certain manifolds," *IEEE transactions on medical imaging*, vol. 5, no. 4, pp. 170–176, 1986.

[76] H. Stark, J. Woods, I. Paul, and R. Hingorani, "Direct fourier reconstruction in computer tomography," *IEEE Transactions on Acoustics, Speech, and Signal Processing*, vol. 29, no. 2, pp. 237–245, 1981.

[77] A. Azaripour, T. Lagerweij, C. Scharfbillig, A. E. Jadczak, B. Willershausen, and C. J. Van Noorden, "A survey of clearing techniques for 3d imaging of tissues with special reference to connective tissue," *Progress in histochemistry and cytochemistry*, vol. 51, no. 2, pp. 9–23, 2016.

[78] S. Inoué and K. Spring, *Video microscopy: The fundamentals.* Springer, 1997.

[79] J. R. Walls, J. G. Sled, J. Sharpe, and R. M. Henkelman, "Correction of artefacts in optical projection tomography," *Physics in Medicine & Biology*, vol. 50, no. 19, p. 4645, 2005.

[80] M. Rieckher, U. J. Birk, H. Meyer, J. Ripoll, and N. Tavernarakis, "Microscopic optical projection tomography in vivo," *PLOS one*, vol. 6, no. 4, p. e18963, 2011.

[81] R. W. Cole and J. N. Turner, "Light-emitting diodes are better illumination sources for biological microscopy than conventional sources," *Microscopy and Microanalysis*, vol. 14, no. 3, pp. 243–250, 2008.

[82] D. Dong, S. Zhu, C. Qin, V. Kumar, J. V. Stein, S. Oehler, C. Savakis, J. Tian, J. Ripoll, *et al.*, "Automated recovery of the center of rotation in optical projection tomography in the presence of scattering.," *IEEE J. Biomedical and Health Informatics*, vol. 17, no. 1, pp. 198–204, 2013.

[83] G. J. Gage, D. R. Kipke, and W. Shain, "Whole animal perfusion fixation for rodents," *Journal of visualized experiments: JoVE*, no. 65, 2012.

[84] C. Antal, M. Teletin, O. Wendling, M. Dgheem, J. Auwerx, and M. Mark, “Tissue collection for systematic phenotyping in the mouse,” *Current protocols in molecular biology*, vol. 80, no. 1, pp. 29A–4, 2007.

[85] L. Quintana and J. Sharpe, “Preparation of mouse embryos for optical projection tomography imaging,” *Cold Spring Harbor Protocols*, vol. 2011, no. 6, pp. pdb–prot5639, 2011.

[86] B. W. Lindsey, A. M. Douek, F. Loosli, and J. Kaslin, “A whole brain staining, embedding, and clearing pipeline for adult zebrafish to visualize cell proliferation and morphology in 3-dimensions,” *Frontiers in neuroscience*, vol. 11, p. 750, 2018.

[87] Lund University - Faculty of Medicine, “OPT imaging platform.” https://www.med.lu.se/english/research/infrastructure/opt_imaging_platform. Accessed: 2018-12-24.

[88] A. Li, H. Gong, B. Zhang, Q. Wang, C. Yan, J. Wu, Q. Liu, S. Zeng, and Q. Luo, “Micro-optical sectioning tomography to obtain a high-resolution atlas of the mouse brain,” *Science*, vol. 330, no. 6009, pp. 1404–1408, 2010.

[89] H. Gong, S. Zeng, C. Yan, X. Lv, Z. Yang, T. Xu, Z. Feng, W. Ding, X. Qi, A. Li, *et al.*, “Continuously tracing brain-wide long-distance axonal projections in mice at a one-micron voxel resolution,” *Neuroimage*, vol. 74, pp. 87–98, 2013.

[90] J. Huisken and D. Y. Stainier, “Selective plane illumination microscopy techniques in developmental biology,” *Development*, vol. 136, no. 12, pp. 1963–1975, 2009.

[91] L. Silvestri, A. L. A. Mascaro, I. Costantini, L. Sacconi, and F. S. Pavone, “Correlative two-photon and light sheet microscopy,” *Methods*, vol. 66, no. 2, pp. 268–272, 2014.

[92] E. Lugo-Hernandez, A. Squire, N. Hagemann, A. Brenzel, M. Sardari, J. Schlechter, E. H. Sanchez-Mendoza, M. Gunzer, A. Faissner, and D. M. Hermann, “3d visualization and quantification of microvessels in the whole ischemic mouse brain using solvent-based clearing and light sheet microscopy,” *Journal of Cerebral Blood Flow & Metabolism*, vol. 37, no. 10, pp. 3355–3367, 2017.

[93] E. G. Reynaud, J. Peychl, J. Huisken, and P. Tomancak, “Guide to light-sheet microscopy for adventurous biologists,” *Nature methods*, vol. 12, no. 1, p. 30, 2014.

[94] J. R. Walls, J. G. Sled, J. Sharpe, and R. M. Henkelman, “Resolution improvement in emission optical projection tomography,” *Physics in Medicine & Biology*, vol. 52, no. 10, p. 2775, 2007.

[95] C. Vinegoni, D. Razansky, J.-L. Figueiredo, M. Nahrendorf, V. Ntziachristos, and R. Weissleder, “Normalized born ratio for fluorescence optical projection tomography,” *Optics letters*, vol. 34, no. 3, pp. 319–321, 2009.

[96] T. Correia, N. Lockwood, S. Kumar, J. Yin, M.-C. Ramel, N. Andrews, M. Katan, L. Bugeon, M. J. Dallman, J. McGinty, *et al.*, "Accelerated optical projection tomography applied to in vivo imaging of zebrafish," *PLOS one*, vol. 10, no. 8, p. e0136213, 2015.

[97] C. Vinegoni, L. Fexon, P. F. Feruglio, M. Pivovarov, J.-L. Figueiredo, M. Nahrendorf, A. Pozzo, A. Sbarbati, and R. Weissleder, "High throughput transmission optical projection tomography using low cost graphics processing unit," *Optics express*, vol. 17, no. 25, pp. 22320–22332, 2009.

[98] A. Arranz, D. Dong, S. Zhu, C. Savakis, J. Tian, and J. Ripoll, "In-vivo optical tomography of small scattering specimens: time-lapse 3d imaging of the head eversion process in drosophila melanogaster," *Scientific reports*, vol. 4, p. 7325, 2014.

[99] C. Vinegoni, C. Pitsouli, D. Razansky, N. Perrimon, and V. Ntziachristos, "In vivo imaging of drosophila melanogaster pupae with mesoscopic fluorescence tomography," *Nature methods*, vol. 5, no. 1, p. 45, 2008.

[100] J. McGinty, H. B. Taylor, L. Chen, L. Bugeon, J. R. Lamb, M. J. Dallman, and P. M. French, "In vivo fluorescence lifetime optical projection tomography," *Biomedical optics express*, vol. 2, no. 5, pp. 1340–1350, 2011.

[101] K. Lee, J. Avondo, H. Morrison, L. Blot, M. Stark, J. Sharpe, A. Bangham, and E. Coen, "Visualizing plant development and gene expression in three dimensions using optical projection tomography," *The Plant Cell*, vol. 18, no. 9, pp. 2145–2156, 2006.

[102] K. J. Lee, G. M. Calder, C. R. Hindle, J. L. Newman, S. N. Robinson, J. J. Avondo, and E. S. Coen, "Macro optical projection tomography for large scale 3d imaging of plant structures and gene activity," *Journal of experimental botany*, vol. 68, no. 3, pp. 527–538, 2016.

[103] S. Gupta, R. Utoft, H. Hasseldam, A. Schmidt-Christensen, T. D. Hannibal, L. Hansen, N. Fransén-Pettersson, N. Agarwal-Gupta, B. Rozell, Å. Andersson, *et al.*, "Global and 3d spatial assessment of neuroinflammation in rodent models of multiple sclerosis," *PloS one*, vol. 8, no. 10, p. e76330, 2013.

[104] J. A. Gleave, J. P. Lerch, R. M. Henkelman, and B. J. Nieman, "A method for 3d immunostaining and optical imaging of the mouse brain demonstrated in neural progenitor cells," *Plos one*, vol. 8, no. 8, p. e72039, 2013.

[105] H. Oakley, S. L. Cole, S. Logan, E. Maus, P. Shao, J. Craft, A. Guillozet-Bongaarts, M. Ohno, J. Disterhoft, L. Van Eldik, *et al.*, "Intraneuronal β-amyloid aggregates, neurodegeneration, and neuron loss in transgenic mice with five familial alzheimer's disease mutations: potential factors in amyloid plaque formation," *Journal of Neuroscience*, vol. 26, no. 40, pp. 10129–10140, 2006.

[106] K. Spring and S. Inoué, "Video microscopy: the fundamentals," 1997.

[107] J. Schindelin, I. Arganda-Carreras, E. Frise, V. Kaynig, M. Longair, T. Pietzsch, S. Preibisch, C. Rueden, S. Saalfeld, B. Schmid, *et al.*, “Fiji: an open-source platform for biological-image analysis,” *Nature methods*, vol. 9, no. 7, p. 676, 2012.

[108] P. Thévenaz and M. Unser, “User-friendly semiautomated assembly of accurate image mosaics in microscopy,” *Microscopy research and technique*, vol. 70, no. 2, pp. 135–146, 2007.

[109] M.-T. Ke, S. Fujimoto, and T. Imai, “Seedb: a simple and morphology-preserving optical clearing agent for neuronal circuit reconstruction,” *Nature neuroscience*, vol. 16, no. 8, p. 1154, 2013.

[110] J. R. Walls, L. Coultas, J. Rossant, and R. M. Henkelman, “Three-dimensional analysis of vascular development in the mouse embryo,” *PloS one*, vol. 3, no. 8, p. e2853, 2008.

[111] E. S. Lein, M. J. Hawrylycz, N. Ao, M. Ayres, A. Bensinger, A. Bernard, A. F. Boe, M. S. Boguski, K. S. Brockway, E. J. Byrnes, *et al.*, “Genome-wide atlas of gene expression in the adult mouse brain,” *Nature*, vol. 445, no. 7124, p. 168, 2007.

[112] K. Chung and K. Deisseroth, “Clarity for mapping the nervous system,” *Nature methods*, vol. 10, no. 6, p. 508, 2013.

[113] H. Hama, H. Kurokawa, H. Kawano, R. Ando, T. Shimogori, H. Noda, K. Fukami, A. Sakaue-Sawano, and A. Miyawaki, “Scale: a chemical approach for fluorescence imaging and reconstruction of transparent mouse brain,” *Nature neuroscience*, vol. 14, no. 11, p. 1481, 2011.

[114] A. Ertürk, K. Becker, N. Jährling, C. P. Mauch, C. D. Hojer, J. G. Egen, F. Hellal, F. Bradke, M. Sheng, and H.-U. Dodt, “Three-dimensional imaging of solvent-cleared organs using 3disco,” *Nature protocols*, vol. 7, no. 11, p. 1983, 2012.

[115] “CRediT.” https://casrai.org/credit/. Accessed: 2018-10-24.

[116] D. Soliman, G. J. Tserevelakis, M. Omar, and V. Ntziachristos, “Combining microscopy with mesoscopy using optical and optoacoustic label-free modes,” *Scientific reports*, vol. 5, p. 12902, 2015.

[117] H. F. Zhang, K. Maslov, G. Stoica, and L. V. Wang, “Functional photoacoustic microscopy for high-resolution and noninvasive in vivo imaging,” *Nature biotechnology*, vol. 24, no. 7, p. 848, 2006.

[118] R. Ma, M. Distel, X. L. Deán-Ben, V. Ntziachristos, and D. Razansky, “Non-invasive whole-body imaging of adult zebrafish with optoacoustic tomography,” *Physics in Medicine & Biology*, vol. 57, no. 22, p. 7227, 2012.

[119] R. J. Bryson-Richardson and P. D. Currie, “Optical projection tomography for spatio-temporal analysis in the zebrafish,” in *Methods in cell biology*, vol. 76, pp. 37–50, Elsevier, 2004.

[120] Z. Hu, J. Gao, N. Zhang, Y. Yang, X. Liu, H. Zheng, and D. Liang, "An improved statistical iterative algorithm for sparse-view and limited-angle ct image reconstruction," *Scientific reports*, vol. 7, no. 1, p. 10747, 2017.

[121] W. M. S. Russell, R. L. Burch, and C. W. Hume, *The principles of humane experimental technique*, vol. 238. Methuen London, 1959.

[122] R. W. Cole, T. Jinadasa, and C. M. Brown, "Measuring and interpreting point spread functions to determine confocal microscope resolution and ensure quality control," *Nature protocols*, vol. 6, no. 12, p. 1929, 2011.

[123] P. C. Goodwin, "Evaluating optical aberrations using fluorescent microspheres: Methods, analysis, and corrective actions," in *Methods in cell biology*, vol. 114, pp. 369–385, Elsevier, 2013.

[124] C. E. Shannon, "Communication in the presence of noise," *Proceedings of the IRE*, vol. 37, no. 1, pp. 10–21, 1949.

[125] J. van der Horst and J. Kalkman, "Image resolution and deconvolution in optical tomography," *Optics express*, vol. 24, no. 21, pp. 24460–24472, 2016.

[126] L. Breiman, "Random forests," *Machine learning*, vol. 45, no. 1, pp. 5–32, 2001.

[127] S. Han, M. Kollmer, D. Markx, S. Claus, P. Walther, and M. Fändrich, "Amyloid plaque structure and cell surface interactions of β-amyloid fibrils revealed by electron tomography," *Scientific reports*, vol. 7, p. 43577, 2017.

[128] R. H. Takahashi, T. Nagao, and G. K. Gouras, "Plaque formation and the intraneuronal accumulation of β-amyloid in alzheimer's disease," *Pathology international*, vol. 67, no. 4, pp. 185–193, 2017.

[129] J. Götz, J. Streffer, D. David, A. Schild, F. Hoerndli, L. Pennanen, P. Kurosinski, and F. Chen, "Transgenic animal models of alzheimer's disease and related disorders: histopathology, behavior and therapy," *Molecular psychiatry*, vol. 9, no. 7, p. 664, 2004.

[130] P. Yan, A. W. Bero, J. R. Cirrito, Q. Xiao, X. Hu, Y. Wang, E. Gonzales, D. M. Holtzman, and J.-M. Lee, "Characterizing the appearance and growth of amyloid plaques in app/ps1 mice," *Journal of Neuroscience*, vol. 29, no. 34, pp. 10706–10714, 2009.

[131] S. Hu, P. Yan, K. Maslov, J.-M. Lee, and L. V. Wang, "Intravital imaging of amyloid plaques in a transgenic mouse model using optical-resolution photoacoustic microscopy," *Optics letters*, vol. 34, no. 24, pp. 3899–3901, 2009.

[132] B. Pinzer, M. Cacquevel, P. Modregger, S. McDonald, J. Bensadoun, T. Thuering, P. Aebischer, and M. Stampanoni, "Imaging brain amyloid deposition using grating-based differential phase contrast tomography," *Neuroimage*, vol. 61, no. 4, pp. 1336–1346, 2012.

[133] C. Dudeffant, M. Vandesquille, K. Herbert, C. M. Garin, S. Alves, V. Blanchard, E. E. Comoy, F. Petit, and M. Dhenain, “Contrast-enhanced mr microscopy of amyloid plaques in five mouse models of amyloidosis and in human alzheimer’s disease brains,” *Scientific reports*, vol. 7, no. 1, p. 4955, 2017.

[134] K. Becker, N. Jährling, S. Saghafi, and H.-U. Dodt, “Ultramicroscopy: light-sheet-based microscopy for imaging centimeter-sized objects with micrometer resolution,” *Cold Spring Harbor protocols*, vol. 2013, no. 8, pp. pdb–top076539, 2013.

[135] T. Liebmann, N. Renier, K. Bettayeb, P. Greengard, M. Tessier-Lavigne, and M. Flajolet, “Three-dimensional study of alzheimer’s disease hallmarks using the idisco clearing method,” *Cell reports*, vol. 16, no. 4, pp. 1138–1152, 2016.

[136] W. E. Klunk, B. J. Bacskai, C. A. Mathis, S. T. Kajdasz, M. E. McLellan, M. P. Frosch, M. L. Debnath, D. P. Holt, Y. Wang, and B. T. Hyman, “Imaging aβ plaques in living transgenic mice with multiphoton microscopy and methoxy-x04, a systemically administered congo red derivative,” *Journal of Neuropathology & Experimental Neurology*, vol. 61, no. 9, pp. 797–805, 2002.

[137] A. Ebadi, J. L. Dalboni da Rocha, D. B. Nagaraju, F. Tovar-Moll, I. Bramati, G. Coutinho, R. Sitaram, and P. Rashidi, “Ensemble classification of alzheimer’s disease and mild cognitive impairment based on complex graph measures from diffusion tensor images,” *Frontiers in neuroscience*, vol. 11, p. 56, 2017.

[138] E. Gallego-Jutglà, M. Elgendi, F. Vialatte, J. Solé-Casals, A. Cichocki, C. Latchoumane, J. Jeong, and J. Dauwels, “Diagnosis of alzheimer’s disease from eeg by means of synchrony measures in optimized frequency bands,” in *Engineering in Medicine and Biology Society (EMBC), 2012 Annual International Conference of the IEEE*, pp. 4266–4270, IEEE, 2012.

[139] S. Beker, V. Kellner, G. Chechik, and E. A. Stern, “Learning to classify neural activity from a mouse model of alzheimer’s disease amyloidosis versus controls,” *Alzheimer’s & Dementia: Diagnosis, Assessment & Disease Monitoring*, vol. 2, pp. 39–48, 2016.

[140] K. R. Gray, P. Aljabar, R. A. Heckemann, A. Hammers, D. Rueckert, A. D. N. Initiative, *et al.*, “Random forest-based similarity measures for multi-modal classification of alzheimer’s disease,” *NeuroImage*, vol. 65, pp. 167–175, 2013.

[141] C. Chubb, Y. Inagaki, P. Sheu, B. Cummings, A. Wasserman, E. Head, and C. Cotman, “Biovision: an application for the automated image analysis of histological sections,” *Neurobiology of aging*, vol. 27, no. 10, pp. 1462–1476, 2006.

[142] F. Letronne, G. Laumet, A.-M. Ayral, J. Chapuis, F. Demiautte, M. Laga, M. E. Vandenberghe, N. Malmanche, F. Leroux, F. Eysert, *et al.*, “Adam30 downregulates app-linked defects through cathepsin d activation in alzheimer’s disease,” *EBioMedicine*, vol. 9, pp. 278–292, 2016.

[143] M. E. Vandenberghe, A.-S. Hérard, N. Souedet, E. Sadouni, M. D. Santin, D. Briet, D. Carré, J. Schulz, P. Hantraye, P.-E. Chabrier, *et al.*, "High-throughput 3d whole-brain quantitative histopathology in rodents," *Scientific reports*, vol. 6, p. 20958, 2016.

[144] Y. Li, X. Zhu, P. Wang, J. Wang, S. Liu, F. Li, and M. Qiu, "Detection of aβ plaque deposition in mr images based on pixel feature selection and class information in image level," *Biomedical engineering online*, vol. 15, no. 1, p. 108, 2016.

[145] M. Grand'Maison, S. P. Zehntner, M.-K. Ho, F. Hébert, A. Wood, F. Carbonell, A. P. Zijdenbos, E. Hamel, and B. J. Bedell, "Early cortical thickness changes predict β-amyloid deposition in a mouse model of alzheimer's disease," *Neurobiology of disease*, vol. 54, pp. 59–67, 2013.

[146] A. Depeursinge, A. Foncubierta-Rodriguez, D. Van De Ville, and H. Müller, "Three-dimensional solid texture analysis in biomedical imaging: review and opportunities," *Medical image analysis*, vol. 18, no. 1, pp. 176–196, 2014.

[147] C. Sommer and D. W. Gerlich, "Machine learning in cell biology–teaching computers to recognize phenotypes," *J Cell Sci*, pp. jcs–123604, 2013.

[148] A. Kreshuk, C. N. Straehle, C. Sommer, U. Koethe, M. Cantoni, G. Knott, and F. A. Hamprecht, "Automated detection and segmentation of synaptic contacts in nearly isotropic serial electron microscopy images," *PloS one*, vol. 6, no. 10, p. e24899, 2011.

[149] P. Strnad, S. Gunther, J. Reichmann, U. Krzic, B. Balazs, G. De Medeiros, N. Norlin, T. Hiiragi, L. Hufnagel, and J. Ellenberg, "Inverted light-sheet microscope for imaging mouse pre-implantation development," *Nature methods*, vol. 13, no. 2, p. 139, 2016.

[150] C. Sommer, C. N. Straehle, U. Koethe, F. A. Hamprecht, *et al.*, "Ilastik: Interactive learning and segmentation toolkit.," in *ISBI*, vol. 2, p. 8, 2011.

[151] The Jackson Laboratory, "B6SJL-Tg(APPSwFlLon,PSEN1*M146L*L286V)6799Vas/Mmjax mouse strain datasheet." https://www.jax.org/strain/006554. Accessed: 2018-10-02.

[152] Swiss Confederation - Federal Food Safety and Veterinary Office, "Animal experimentation." https://www.blv.admin.ch/blv/en/home/tiere/tierversuche.html. Accessed: 2018-10-02.

[153] The Jackson Laboratory, "000686 - SJL/J." https://www.jax.org/strain/000686. Accessed: 2018-10-02.

[154] M. Fernández-Delgado, E. Cernadas, S. Barro, and D. Amorim, "Do we need hundreds of classifiers to solve real world classification problems?," *The Journal of Machine Learning Research*, vol. 15, no. 1, pp. 3133–3181, 2014.

[155] L. Shamir, "Assessing the efficacy of low-level image content descriptors for computer-based fluorescence microscopy image analysis," *Journal of microscopy*, vol. 243, no. 3, pp. 284–292, 2011.

[156] C. A. Raji, J. T. Becker, N. D. Tsopelas, J. C. Price, C. A. Mathis, J. A. Saxton, B. J. Lopresti, J. A. Hoge, S. K. Ziolko, S. T. DeKosky, *et al.*, “Characterizing regional correlation, laterality and symmetry of amyloid deposition in mild cognitive impairment and alzheimer’s disease with pittsburgh compound b,” *Journal of neuroscience methods*, vol. 172, no. 2, pp. 277–282, 2008.

[157] S. Yokota, Y. Ono, T. Nakao, P. Zhang, G. K. Michalopoulos, and Z. Khan, “Partial bile duct ligation in the mouse: A controlled model of localized obstructive cholestasis.,” *Journal of visualized experiments: JoVE*, no. 133, 2018.

[158] M. Stefaniuk, E. J. Gualda, M. Pawlowska, D. Legutko, P. Matryba, P. Koza, W. Konopka, D. Owczarek, M. Wawrzyniak, P. Loza-Alvarez, *et al.*, “Light-sheet microscopy imaging of a whole cleared rat brain with thy1-gfp transgene,” *Scientific reports*, vol. 6, p. srep28209, 2016.

[159] M. G. Gustafsson, “Surpassing the lateral resolution limit by a factor of two using structured illumination microscopy,” *Journal of microscopy*, vol. 198, no. 2, pp. 82–87, 2000.

[160] R. Heintzmann and T. Huser, “Super-resolution structured illumination microscopy,” *Chemical reviews*, vol. 117, no. 23, pp. 13890–13908, 2017.

[161] J. Mertz, “Optical sectioning microscopy with planar or structured illumination,” *Nature methods*, vol. 8, no. 10, p. 811, 2011.

[162] B. Thomas, M. Momany, and P. Kner, “Optical sectioning structured illumination microscopy with enhanced sensitivity,” *Journal of Optics*, vol. 15, no. 9, p. 094004, 2013.

[163] P. Křížek, T. Lukeš, M. Ovesnỳ, K. Fliegel, and G. M. Hagen, “Simtoolbox: a matlab toolbox for structured illumination fluorescence microscopy,” *Bioinformatics*, vol. 32, no. 2, pp. 318–320, 2015.

[164] T. Lukeš, P. Křížek, Z. Švindrych, J. Benda, M. Ovesnỳ, K. Fliegel, M. Klíma, and G. M. Hagen, “Three-dimensional super-resolution structured illumination microscopy with maximum a posteriori probability image estimation,” *Optics express*, vol. 22, no. 24, pp. 29805–29817, 2014.

[165] D. Vettese, “Microdisplays: Liquid crystal on silicon,” *Nature Photonics*, vol. 4, no. 11, p. 752, 2010.

[166] D. Dudley, W. M. Duncan, and J. Slaughter, “Emerging digital micromirror device (dmd) applications,” in *MOEMS display and imaging systems*, vol. 4985, pp. 14–26, International Society for Optics and Photonics, 2003.

[167] D. Dan, M. Lei, B. Yao, W. Wang, M. Winterhalder, A. Zumbusch, Y. Qi, L. Xia, S. Yan, Y. Yang, *et al.*, “Dmd-based led-illumination super-resolution and optical sectioning microscopy,” *Scientific reports*, vol. 3, p. 1116, 2013.

[168] H.-U. Dodt, S. Saghafi, K. Becker, N. Jährling, A. Niendorf, C. Hahn, M. Pende, and M. Wanis, “Ultramicroscopy: development and outlook,” *Neurophotonics*, vol. 2, no. 4, p. 041407, 2015.

[169] C. Choi, K.-D. Song, S. Kang, J.-S. Park, and W. Choi, “Optical imaging featuring both long working distance and high spatial resolution by correcting the aberration of a large aperture lens,” *Scientific reports*, vol. 8, no. 1, p. 9165, 2018.

[170] S. M. Mansfield and G. Kino, “Solid immersion microscope,” *Applied physics letters*, vol. 57, no. 24, pp. 2615–2616, 1990.

[171] V. Marx, “Microscopy: hello, adaptive optics,” 2017.

[172] N. Ji, “Adaptive optical fluorescence microscopy,” *Nature methods*, vol. 14, no. 4, p. 374, 2017.

DAVID NGUYEN

Engineer in Microtechnologies

📱 +41 (0)79 241 4031

✉ david.nguyen.ch@gmail.com

iD 0000-0002-3067-2241

Technical Skills

Overview

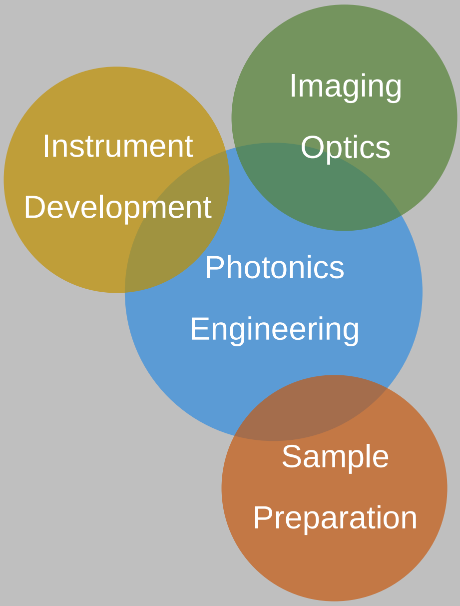

Languages

French (mother tongue) • English (C1) • German (A1)

Software

Solidworks • OpticStudio • Imaris • ImageJ • Office • LaTeX • Illustrator

Programming

Matlab • Java • C/C++ • PHP • MySQL

Interests

Rock climbing

Running

Personal development

Publications (selected out of 7)

Nguyen D, Uhlmann V, et al. Supervised learning to quantify amyloidosis in whole brains of an Alzheimer's disease mouse model acquired with optical projection tomography. PLOS ONE [submitted]. 2018.

Nguyen D, Marchand PJ, et al. Optical projection tomography for rapid whole mouse brain imaging. Biomed Opt Express. 2017. doi:10.1364/BOE.8.005637.

Berclaz C, Szlag D, **Nguyen D**, et al. Label-free fast 3D coherent imaging reveals pancreatic islet micro-vascularization and dynamic blood flow. Biomed Opt Express. 2016. doi:10.1364/BOE.7.004569.

Sommet N, **Nguyen D**, et al. When and why performance goals predict exploitation behaviors: An achievement goal complex analysis of the selection function of assessment. Motiv Emot. 2018.

Teaching

2014-Present	**Project supervision** • Whole-brain imaging in Alzheimer's mouse models, Amélie Ducrey, 2016 • Segmentation of amyloid plaques in OPT mouse brain images, 2016 **Teaching assistant** Biomicroscopy I (1 semester) Imaging Optics (2 semesters)
2016-Present	**Volunteer school tutor in a domestic violence shelter**

Research

2014-Present	**Ph.D, Bioengineering** Thesis: Mesoscopy of the mouse brain for the study of Alzheimer's disease • Design, construction and exploitation of an Optical Projection Tomography instrument • Optical clearing and whole rodent organ preparation for imaging (trained in animal experimentation: RESAL 1) LABORATOIRE D'OPTIQUE BIOMÉDICALE Ecole Polytechnique Fédérale de Lausanne (EPFL), Switzerland

Education

2012-2014	**MSc., Microengineering** (avg 5.63/max 6) Specialization: Applied Optics Ecole Polytechnique Fédérale de Lausanne (EPFL), Switzerland
2009-2012	**BSc., Microengineering** (avg 4.79/max 6) Ecole Polytechnique Fédérale de Lausanne (EPFL), Switzerland
2008-2009	**Cours de Mathématiques Spéciales** Ecole Polytechnique Fédérale de Lausanne (EPFL), Switzerland
2005-2008	**Federal Diploma of Vocational Education and Training (CFC) in Computer Science** CIFOM-ET, Switzerland

Ce document a été imprimé au Centre d’impression EPFL,
imprimerie climatiquement neutre, certifiée myClimate.